Quantitative Evaluation of Oil Pipeline Cracks Using an Electromagnetic Acoustic Transducer and Numerical Simulation

IVAN FERNANDO LAZCANO-GUZMAN

Quantitative Evaluation of Oil Pipeline Cracks Using an Electromagnetic Acoustic Transducer and Numerical Simulation

Ivan Fernando Lazcano Guzman

A Thesis presented for the degree of
Master of Science

Department of Engineering
Durham University
United Kingdom

September 2020

Dedication

To my mom and dad, who always gave everything in the world for their children. For all their hard work during all these years and never giving up. I aspire to do an incredible job with my children as you did with yours. For all your support and love, thank you.

Quantitative Evaluation of Oil Pipeline Cracks Using Electromagnetic Acoustic Transducers and Numerical Simulation

Abstract

Defect detection is of great importance in the oil and gas industry. Early defect detection prevents structure failures leading to safe operations and to non-negative economic impact. Quantifying the depth of a defect is achievable using ultrasonic guided waves and Electromagnetic Acoustic Transducers (EMAT). Producing Lamb waves and using their dispersive properties, the velocity variations of these waves travelling within the pipe boundaries can be converted into thickness using a fixed frequency. The Simultaneous Iterative Reconstruction Technique (SIRT) algorithm is employed to achieve this quantification and obtain a thickness map of the pipeline. This project aims to successfully detect hole type and corrosion type defects through experimentation and numerical simulation using the proposed algorithm in both cases. The corrosion defect to identify is 1mm depth at its deepest point, 10.5mm long and 20mm wide. The hole defect type are three 2mm diameter holes aligned with the pipeline axis. Processing the signals obtained from the guided waves we obtain the arrival times to convert it into velocity and further conversion into thickness using the dispersive relationship of the Lamb waves. Doing this for the base cases, a pipeline with no defect and the pipeline in the presence of a defect, it is possible to obtain a thickness map of the area where the waves travelled and collected information for the denominated area of interest. Comparing the signals obtained when the algorithm is implemented, we are able to identify a thickness variation and determine whether a defect exists or if the pipeline is clean.

Declaration

The work in this thesis is based on research carried out at the Sustainable Infrastructure Research Challenge, the Department of Engineering, United Kingdom. No part of this thesis has been submitted elsewhere for any other degree or qualification and it is all my own work unless referenced to the contrary in the text.

Acknowledgements

First, I would like to express my special thanks and all my gratitude to Dr. Qing Wang for her excellent guidance and unconditional support during the entire duration of this project. You are a magnificent supervisor. I would like to extend my gratitude to Dalia who morally supported and accompanied me during this time. Finally, to Josue and David for all the support given in this project.

Contents

List of Figures

List of Tables

List of Acronyms

ART Algebraic Reconstruction Technique.

DR-SIRT Dimensional Reduction Simultaneous Iterative Reconstruction Technique.

EMAT Electromagnetic Acoustic Transducer.

ERT Electrical Resistance Tomography.

ET Electromagnetic Testing.

FMM Fast Marching Method.

GWT Guided Wave Testing.

HARBUT Hybrid Algorithm for Robust Breast Ultrasound Tomography.

NDE Non-Destructive Evaluation.

NDT Non-Destructive Testing.

PLA Polylactic Acid.

SHM Structural Health Monitoring.

SIRT Simultaneous Iterative Reconstruction Technique.

SNR Signal-to-Noise Ratio.

TOF Time Of Flight.

UGW Ultrasonic Guided Waves.

UT Ultrasonic Testing.

VT Visual and Optical Testing.

Nomenclature

δ	Skin depth
γ	Conductivity of specimen
μ	Magnetic permeability
μ_m	Relative permeability of the specimen
ρ	Electrical resistivity
B_d	Dynamic magnetic flux density
B_s	Static magnetic field flux density
E_E	Eddy currents electric field intensity
f	Frequency
F_L	Lorenz Force resultant
f_L	Lorenz force bulk density
H_d	Dynamic magnetic field
J_0	Excitation current density
J_e	Eddy currents density
$L[i,j]$	Total length of the ray[i,j]
$l[i,j]$	Length of a ray[i,j]
$t[i,j,m,n]$	Time of the wave crossing a pixel[m,n] of the ray[i,j]

$T[i, j]$ Total time of flight of the ray[i,j]

$v[m, n]$ Velocity of the wave in the pixel[m,n]

Chapter 1

Introduction

1.1 Background of the research

Many pipeline failures around the world have been reported. In Canada, the earliest report of a pipeline failure dates from 1962, where an explosion in a gas pipeline occurred, causing the loss of human life [1]. Moreover, in 1999, a pipeline failed due to corrosion, causing the spillage of 3,213 m^3 of crude oil, highly contaminating the soil [2]. More recently, in the United States a pipeline spilled approximately 1,450 m^3 of oil in North Dakota. In 2011, 53 m^3 were spilled and in 2017 it leaked around 1,540 m^3 from the same pipeline [3]. Environmental circumstances promote the development of corrosion in the pipe wall when the coating is disbonded and the section under the disbonded area is more susceptible to develop corrosion due to the environmental conditions. When the pipeline wall loses material reducing its thickness, the operational pressure at which these pipes are designed is exceeded, causing an explosion if the pressure is high enough, or producing small cracks from where the liquid leaks. Therefore, damage detection in pipelines is of great significance in economic and safety terms in the oil and gas industry. The integrity monitoring of pipelines and other structures in these industries is a regular practice and of great importance. The health of these structures leads to good operation and performance of its activities. However, when the integrity of these structures is compromised by environmental and operational factors due to a lack of monitoring, and it is not attended to correctly, the consequences may be fatal.

Non-Destructive Testing/Non-Destructive Evaluation (NDT/NDE) techniques are used to evaluate the integrity of the structure without doing any damage to the structure itself. The most common and basic NDT/NDE technique is Visual and Optical Testing (VT), which refers to a simple visual inspection from the user to examine the surface and locate anomalies. Moreover, Electromagnetic Testing (ET), commonly called Eddy currents, are generated due to a changing magnetic field in a conductive material. The defect is detected when it obstructs the flow of the eddy currents induced. Another technique is Ultrasonic Testing (UT), in this high frequency sound waves travel through the material to identify changes in the material. In UT, bulk waves are used, which travel in a direction perpendicular to the surface of the object where the sensor is placed. [4]. Although the techniques mentioned before are commonly used and accurate results are obtained, they share a similar limitation. Some NDT/NDE techniques are listed in Table 1.1 with their action principles.

NDT/NDE Technique	Principle
Visual Testing (VT)	Physical examination by user
Eddy Currents	Electric
Ultrasonic Testing (UT)	Acoustic
Ultrasonic Guided Waves	Acoustic
Radiography (RT)	Radiaton
Magnetic Flux Leakage	Magnetic

Table 1.1: NDT/NDE techniques and their principle of operation

Pipelines are regularly buried or underwater, inaccessible for normally use NDT techniques. For such problems, Guided Wave Testing (GWT) has been used to locate imperfections in cases where other methods are unable to. Usually GWT consists of analyzing the Time Of Flight (TOF) of the waves and comparing them with a base measurement carried out when the material is in a perfect state. Comparing the base and the new TOF measurements with the amplitude of the wave it is possible to see if a disturbance appears in the signal, pointing out an imperfection, as was performed in [5–7]. With a known velocity of the wave and the position of the sensors, it is possible to locate the defect. However, using such techniques we are unable to estimate how dangerous the defect is and the time of action to repair the

defect before the spillage begins. In other words, the quantification of the defect is still an uncertainty.

1.2 Scope, aim and objectives of the research

For such problems, the use of Ultrasonic Guided Waves (UGW) proved to be an effective technique when combined with an algorithm to process data and estimate the wall thickness of the pipeline. Ultrasonic waves are mechanical disturbances that reproduce in an elastic medium and travel through it at ultrasonic frequencies. The ultrasonic range is above 20 kHz and is not detectable to human hearing (Fig. 1.1). Moreover, guided waves are elastic waves that propagate within the medium limits and such boundaries or limits are given by waveguides or in other words the object (plates, rods, hollow cylinder, multilayer structures, etc.). Thus, UGW are a combination of both waves previously mentioned. Because UGW are guided, they are capable of travelling more than a hundred meters with relatively low energy loss [8]. Moreover, low ranges in the ultrasonic range (30-200 kHz) are used to generate ultrasonic guided waves for long distance inspection. Using devices such as piezoelectrics, it is possible to generate ultrasonic guided waves to implement reconstruction techniques or tomography algorithms. Although the piezoelectrics are very effective, they strictly require to be coupled to the object over a clean and regular surface using a special couplant.

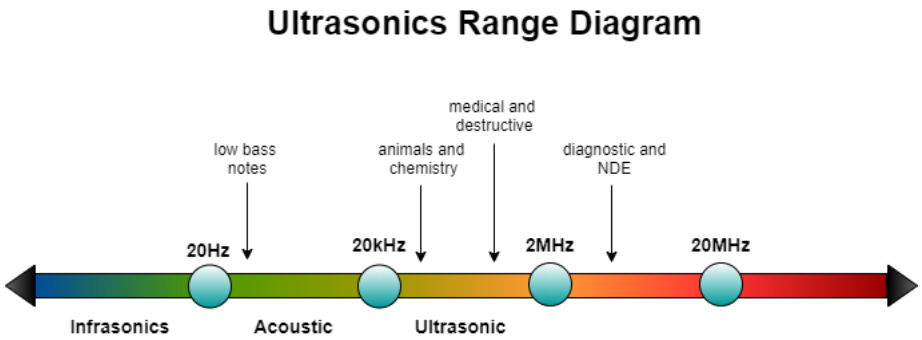

Figure 1.1: Ultrasonic Range Diagram. The ultrasonic range is illustrated in the figure as well as examples of noise and procedures at certain frequencies.

The Electromagnetic Acoustic Transducer (EMAT) is a relatively new and cost-effective technology in (NDT) and Structural Health Monitoring (SHM). The EMAT is mainly composed of a coil and a magnet (Fig. 1.2). An alternating current is induced in the coil, inducing eddy currents at a skin depth surface of the material. The eddy currents in the presence of a magnetic field generated by the magnet generate the Lorentz force, which creates vibrations, that reproduce the elastic wave [5–7, 9]. For its structure and operation mode, it has a contactless nature, allowing it, to produce UGW with no need for a coupling system and translation of the transducer. Moreover, the couplant used in the piezoelectric restricts the operation to a range of temperatures where the couplant does not melt. Furthermore, the couplant causes a scattering in the wave, contaminating the signal and making it harder to process [10]. Therefore, the EMAT overcomes these difficulties of the piezoelectric and it is used in this research as the transduction device. For such purposes, we use the property of dependence between velocity and frequency-thickness of the lamb waves [10–12]. This project aims to successfully quantify the depth of two different defect types in a pipe, a crack type defect with a radius of 2.5mm and an oval-shaped corrosion type defect with of 20mm in its longer axis and 10.2mm in its shorter axis. Using the proposed Simultaneous Iterative Reconstruction Technique (SIRT) - Fast Marching Method (FMM) algorithm enables the helical path and bent-rays consideration to achieve more accurate results.

The content of this project is presented in six chapters, the following points provide a brief resume of the main objective of the chapters of this thesis.

- Chapter 1. Background of the problematic and objectives of the research are presented.
- Chapter 2. The selection of wave mode, including advantages and properties of the selected mode is discussed. Additionally, the selection of the transducer design specifications for a proper excitation of the A0 Lamb wave mode are given.

- Chapter 3. A theoretical background of implemented algorithms using guided waves as well as the proposed algorithm of this thesis are presented, explained and discussed.

- Chapter 4. Software, simulation setup and results are provided. The algorithm is extensively explained and results are shown. The algorithm implemented in this research is presented and examined.

- Chapter 5. An explanation of the experimentation and its components as well as previous tests at different parameters are illustrated.

- Chapter 6. Conclusions are given and possible further work in the area is proposed.

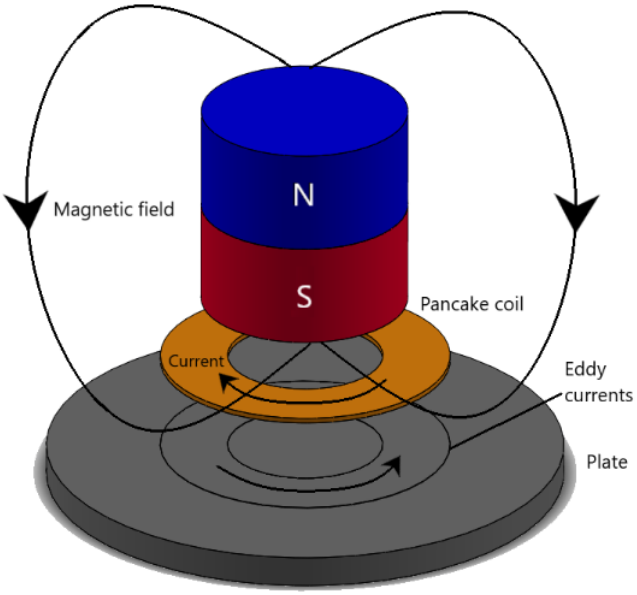

Figure 1.2: Omni-directional Electromagnetic Acoustic Transducer structure concept. The figure illustrates the acting magnetic field generated by the magnet, pancake coil and the generated eddy currents at a skin depth of the plate. Adapted image from [11].

Chapter 2

Tomography System Development

In this chapter, the selection of the components needed for the guided wave tomography is presented. First, explanations of the guided waves and ultrasonic guided waves are given followed by a discussion and review of previous work where the ultrasonic guided waves are used to identify defects. Second, definitions and properties of Lamb wave modes as well as previous work and reasons for the selection mode are presented. Third, physics related to the operation of the transducer are explained. Finally, the specifications of the transducer to produce the desired wave mode are given as well as reasons for its selection.

2.1 Ultrasonic Guided Waves

Ultrasonic Guided Waves are used for the detection of strange objects. These are widely used in the non-destructive testing field, for the detection of deterioration in a structure due to operational and environmental factors. In addition, UGW are used in quality inspections, where anomalies are searched for inside the material when a special or important structure is built. The popularity of ultrasonic guided wave techniques in recent years has been increasing due to the new and high computational power available. Using computational power, we are able to develop new and more complex algorithms and improve and test theories in this complex field, as well as more realistic simulations and better processing of the data. An important property of the UGW is that they can travel through the entire volume of the object to

inspect it from a single sensor location, where waves reflect back and forth inside the waveguide (pipeline, plate, rod). Using this technique allows the inspection of inaccessible pipelines. It is also possible to cover longer distances with greater sensitivity. Moreover, the wavelength of a wave would commonly be greater than the thickness of the object to inspect if guided waves are being generated. Additionally, an important peculiarity of ultrasonic testing at long distance is the ability to sense defects that are as small as 1-3 percent of the pipe cross section compared to the ultrasonic wavelength, and where the wavelength is greater than the thickness of the pipe, even in some cases greater than the diameter of the pipe [13, 14].

2.1.1 Ultrasonic Guided Waves in Defect Detection

As mentioned before, the EMAT is used in the NDT/NDE. The main purpose of the NDT/NDE area is the detection of default impurities, anomalies that occur in the material from its fabrication, as well as the development of defects such as corrosion and cracks in the objects through its operational life. Ultrasonic Guided Waves have been widely used for defect detection in structures such as pipes, tanks, and plates in the petrochemical industry. Recent work in this specific area has been carried out. In [6], a simulated model with defects and different depths was used, producing UGW by an EMAT in an aluminium plate. In [13], torsional guided waves were excited from an EMAT for permanent pipeline inspection, detecting defects by comparing signals from a defect-free base model. The transducer arrangement works in a pulse-echo mode, where the receivers wait for the normal reflection of the waves from an end or a union. The receivers detect a strange signal where there should be only noise, pointing out that something unusual produced the early reflection of the waves. Moreover, in [14] torsional and longitudinal guided wave modes were used for defect detection, measuring the arrival time. By combining information of the data acquired from both signals in the presence of different size defects, better information of the integrity of the object is obtained. The test has also been carried out with a pipeline filled with liquid and the data shows that information is better than when only exciting one wave mode. Furthermore, in [15] a numerical simulation exciting torsional T(0,2) wave mode was carried out. The same process for defect detection

was applied by comparing the signals from two models, one defect-free and a second one with a defect added. The comparison of the results showed a difference in the signals accounting for the damage added in the pipeline. The detection process in these cases compared the amplitude of the signals taken defect-free with those in the presence of a defect. Results showed that the strength of the signal decreased or the reflection was stronger as the size or the depth of the defect increased. It is proven that it is possible to detect defects using UGW. However, remaining data about defects is still unknown, and the severity of the damage in the object remains an uncertainty.

2.1.2 Lamb A0 and S0 wave modes

Lamb waves are elastic waves that propagate parallel to the plane of the boundaries of the plate and perpendicular to the thickness direction (Fig. 2.1). The wave behaves as a standing wave, in that its peaks do not vary in space only in time. In other words, the standing wave oscillates in the same position. This movement determines its properties (symmetric/ anti-symmetric). Their velocity is dependent on the product of frequency of excitation and the thickness of the medium, also known as the dispersion relationship (Fig. 2.2) [11, 12]. One of the differences of these modes is how the wave moves, the wave modes are named for their movement: A0 (Anti-symmetric) and S0(Symmetric) (Fig. 2.1). Moreover, the number 0 is the order of this type of wave. As the frequency is increased, new order modes are produced, with different velocities depending on the frequency used. This can be seen in Fig. 2.2, where A1 and S1 appear in the graph with different velocities and are produced at different frequency ranges. The use of higher frequencies produces more waves that will be mixed in the signal, which is very difficult to decode to know what wave produced what specific signal. Alternatively, using lower frequencies only produce A0 and S0 lamb waves, producing cleaner signals that are easier to process. The main difference between A0 and S0 is the velocity. As can be seen in Fig. 2.2, S0 has a higher velocity than A0, arriving faster at the sensor. Consequently, this difference is visually appreciable, in signals the arriving time of the S0 is less compared with the A0.

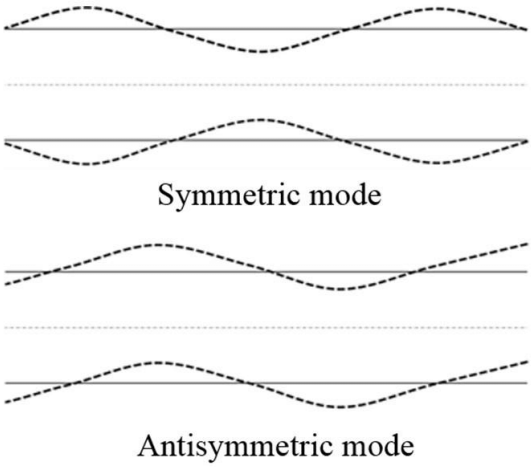

Figure 2.1: Illustration of Lamb wave S0 (Symmetric) and A0(Anti-symmetric) mode movement.

In [16], differences between Lamb A0 and S0 wave modes have been evaluated in past research. The sensitivity of the Lamb A0 and S0 wave modes to imperfections in plates were tested, proving high sensitivity to thickness variations in low frequency ranges from 50, 100 and 150 kHz for the A0 wave mode, due to its steep slope at the beginning of the dispersion curve. In contrast, the S0 Lamb wave mode demonstrates less sensitivity to the thickness variations. However, the S0 Lamb wave mode behaves differently in the presence of liquid, having much less attenuation compared with the A0 mode. Moreover, in [17], the S0 Lamb wave mode was used to detect corrosion in a pipeline, testing its sensitivity through experimentation of defects with different dimensions and shapes. The depth of the artificial hole type defect ranged from 1-2 mm. Similarly, in [18, 19] Lamb wave modes are used for defect detection. The Lamb waves were excited at a frequency of 0.5MHz and 1.35MHz in [18] and from 900-990 kHz in [19]. A tomography of the pipeline detecting a defect is achieved. For the purposes of this research, we have selected the A0 Lamb wave mode for defect detection due to its high sensitivity in relative low frequencies. Additionally, the fixed frequency used is 50kHz due to at such frequency the sensitivity of velocity variations is higher as shown in Fig. 2.2

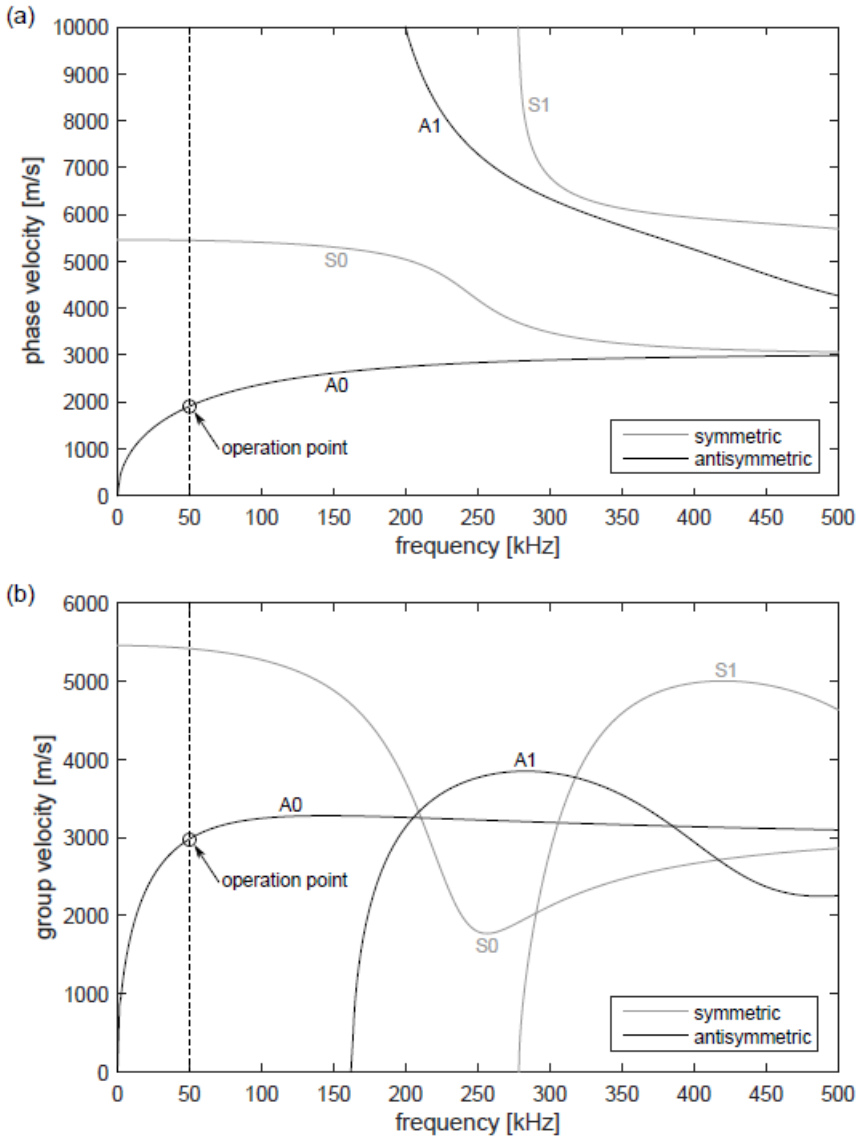

Figure 2.2: Dispersion curves of the Lamb wave mode in a steel plate of 10 mm thickness. Image from [11].

2.2 Electromagnetic Acoustic Transducer

The Electromagnetic Acoustic Transducer is a non-destructive testing technology principally composed of a coil and a magnet or electromagnet above the coil (Fig. 1.2). The EMAT generates acoustic waves electromagnetically, which are mostly used for defect detection due to corrosion and cracks in different structures of interest. The EMAT can work in pulse-echo or through-transmission modes. The pulse-echo refers to a single EMAT exciting the ultrasonic wave and receiving it,

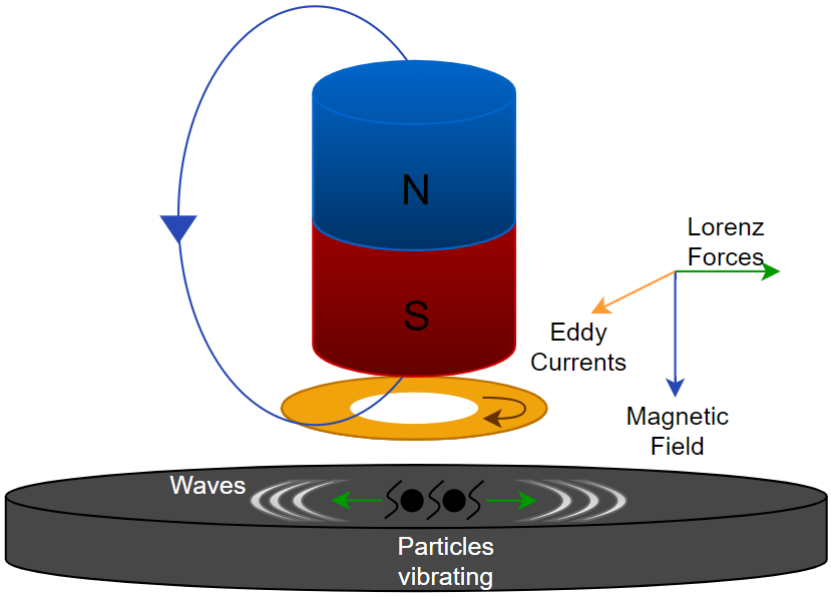

Figure 2.3: Electromagnetic Acoustic Transducer acting forces representation.

and with through-transmission, there are two EMATs, one exciting the waves and the second one receiving them [20]. This technology works with two methods to generate the ultrasonic waves: Lorentz force and Magnetostriction [5,6,9,11,21,22]. An alternating current is induced in the coil, generating eddy currents at a thin layer right under the surface of the object, commonly called skin depth [6,9]. The skin depth (δ) at which the eddy currents are induced is dependent on the excitation frequency (f), the resistivity (ρ) and the permeability (μ) of the conductor. It is calculated as Eq. (1) [13].

$$\delta = \sqrt{\frac{\rho}{\pi f \mu}} \tag{1}$$

Moreover, the eddy currents in the presence of the magnetic field, generates the Lorenz force. The Lorentz Force is a force that makes the particles of the material vibrate and thus generate the elastic waves. Thus, the Lorentz Force is the result of the interaction of these forces, the superposition of the magnetic fields and the eddy current. The Lorentz force principle of EMAT is governed by the equations Eq. (2) to Eq. (8) [5,6,9,11,21,22].

$$\nabla \times H_d = J_0 + \frac{\partial D}{\partial t} \tag{2}$$

$$B_d = \mu_m H_d \tag{3}$$

$$\nabla \times E_E = -\frac{\partial B_d}{\partial t} \tag{4}$$

$$J_e = \gamma E_E \tag{5}$$

$$f_L = J_e \times (B_d + B_s) \tag{6}$$

$$F_L = \iiint_V f_L dV \tag{7}$$

Where $\nabla = \frac{\partial}{\partial x} + \frac{\partial}{\partial y} + \frac{\partial}{\partial z}$ is the gradient vector, H_d is the dynamic magnetic field intensity induced by the coil, J_0 is the excitation current density, B_d is the dynamic magnetic flux density, μ_m is the relative permeability of the specimen, E_E is the electric field intensity of the eddy current, γ is the conductivity of the specimen, J_e is the eddy current density, B_s is the static magnetic flux density from the magnet, f_L is the bulk density of Lorentz force, and F_L is the resultant Lorentz Force. According to Eq. (6), the magnetic field and the eddy current field determine the Lorentz force. Generally, the dynamic magnetic field is much weaker than the static one when the excitation current is not high. Therefore, Eq. (6) can be rewritten as Eq. (8).

$$f_L = J_e \times B_d \tag{8}$$

2.2.1 Electromagnetic Acoustic Transducer in Defect Detection and Efficiency Enhancement

Past work has been carried out in order to improve the efficiency of the EMAT. Most work in the field of improving the efficiency of converting electromagnetic forces into acoustic forces has been carried out using aluminium objects due to their higher electrical conductivity and lower density, increasing the efficiency of the transducer and so transforming electromagnetic energy into acoustical energy. However, the efficiency of the EMAT working under low frequencies and high currents experiences a beneficial increment, as was proven in [23]. Likewise, in [24] a phased EMAT has been developed to be able to produce a sufficient Signal-to-Noise Ratio (SNR), designed specifically for the inspection of thick samples, in which the signals present

high attenuation. Results presented in this work have shown an increase of 35% in the amplitude of the signal and significant improvement in the SNR compared with other designs. However, the current used to obtain such results is around 1.5kA, which is quite high for such small signals obtained ($70mV$). The efficiency of the transducer remains as an area to tackle for researchers and industry. Moreover, in [21] the optimal number of transducers to produce stronger signals in a circular array in a steel pipeline is investigated. The optimal number of transducers is achieved for the proposed EMAT structure for the excitation of the torsional wave mode. Simulations work was split into two models, electromagnetic and acoustic models. The electromagnetic model obtains the induced Lorentz forces due to the eddy currents in the presence of the magnetic field provided by the magnet. Moreover, the Lorentz forces were used as an impulse force in the acoustic model to produce the wave propagation. This research proves that, contrary to what might be deduced, to obtain a stronger signal, more or bigger transducers are needed. To choose the right size of the magnet, the total area of magnetization needs to be taken into consideration. A bigger magnet will provide a stronger magnetic field, however less area will be magnetized, therefore, a balance between strength and size is necessary for excitation efficiency. The most important parameters for the purpose of this research to increase the Lorenz Force were to increase the eddy currents and the magnetic field strength using a different distribution of elements in the array as well as various coil dimensions. A different use of the EMAT was introduced in [25], a special setup of the transducer was used in order to detect defects in an outer pipe wall. The setup of one transmitter and one receiver enabled the ability to move them along the pipeline direction while the excited waves travel in a circumferential direction. Results were obtained by comparing readings for a defect-free model with readings in the presence of a defect acquired from the experimentation. Results showed that the signals obtained from the waves were different in the presence of a defect compared to the readings acquired from the baseline model. However, the comparison and the decision whether a defect exists has to be made by the operator, leading to human error. Furthermore, in [26], a similar setup was made with EMATs in order for detection in the inner pipewall. The EMATs travel inside

the pipeline, controlled by a special device, and the same comparison of the signals is made. Additionally, in [27] a different EMAT design is used for the excitation of torsional waves. The goal in this research is to detect a notch defect through long range guided wave inspection in a pulse-echo mode in pipelines. The structure of the EMAT consist of periodic permanent magnet and a racetrack coil printed in a flexible printed circuit board wrapped in the pipeline, fully covering the diameter of the pipeline. The magnet are placed above the straight lines of the racetrack coil. This setup achieves the excitation of torsional T(0,1) wave mode.

2.2.2 Electromagnetic Acoustic Transducer for Lamb wave Mode Generation

The use of the EMAT has been extended. Many researchers selected Lamb wave modes due to their advantages in quantifying defects after processing the information given by the signals. In [28] different configurations of EMAT were developed and tested in order to excite a pure mode of Lamb wave A0 mode and suppress S0 mode at a noise level. A clean and more pure A0 mode was achieved for easier signal processing. Moreover, the lift off effect was tested in order to examine its relation with the strength of the wave; however, lift off effect experiments resulted in minimum influence on the excitation of the signal in a purity and strength. Moreover, different coil configurations were used to test the sensitivity of the transducer to Lamb wave modes and the relation between coil geometry and sensitivity of the transducer was investigated in [29]. Similarly, in [30], different approaches were used in order to optimize the ratio A0/S0 Lamb wave mode. Furthermore, in [31] different structures were tested in order to enhance a pure mode of helical Lamb wave mode using different configurations of magnets and coils. The magnetic field strength is examined along the length of the transducer and the coil is designed without the results of the different magnet configuration to enhance the eddy currents. The frequencies selected are 200 and 300kHz to produce the Lamb wave modes. Results proved that, when combining a cylindrical magnet and a circular hole magnet with a separation and a coil specially designed for the magnet, it is possible to produce a pure lamb wave mode.

For the purposes of this project a similar structure of the transducer developed in [28] will be used. The selection of the magnet is based on [11, 28] where the magnet selected was able to produce sufficient magnetic strength to excite a pure Lamb A0 wave mode successfully, suppressing the S0 wave mode. To produce a pure helical A0 Lamb wave mode we use a circular coil with an inner and outer diameter of 10 and 28 mm respectively, with 42 turns in a double layer configuration based on the coil VII in [29]. Moreover, a holder for the components was printed in 3D by a MakerBot + Desktop 3D printer with a printing time of one hour and thirty minutes. The blueprints are presented in Fig. 2.4 and Fig. 2.5. The specifications of the transducer components are displayed in Table 2.1. For the requirements of this project the EMAT structure selected is sufficiently strong and easier to fabricate to produce the desired wave mode. Therefore, considering the increasing efficiency of the EMAT working at a low frequency with steel objects and the benefits of using low frequencies producing cleaner signals for easier processing in section 2.1.1, we will excite a Lamb A0 wave mode at 50 kHz due to its high sensitivity.

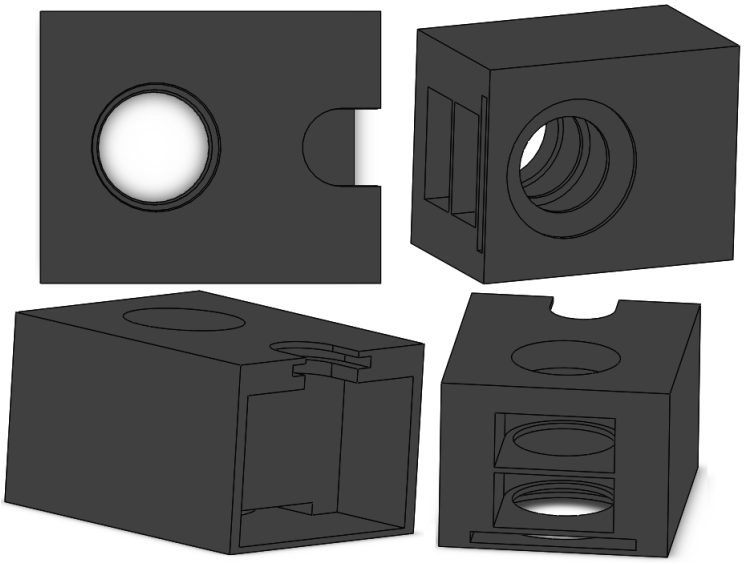

Figure 2.4: Electromagnetic Acoustic Transducer holder 3D model printed by MakerBot + Desktop printer using PLA.

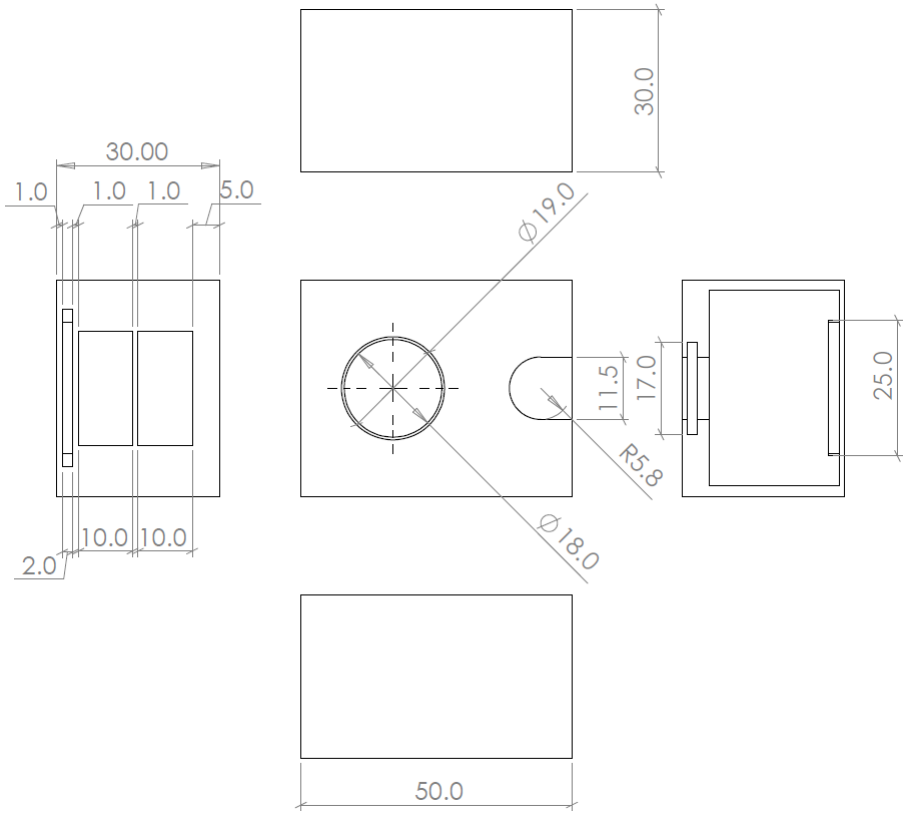

Figure 2.5: 3D holder dimensions. Dimensions in views are presented in millimeters.

Magnet	
Material	Neodymium-Iron-Boron (NdFeB)
Shape	Circular
Diameter	20 mm
Height	10 mm
Strength	0.51 T
Coil	
Outer Diameter	28 mm
Inner Diameter	10 mm
Turns	42 turns
Measured Resistance	25.52 Ω
Measured Inductance	8.67 μH

Table 2.1: Magnet and Coil specifications

2.3 Summary

The UGW have been used in many investigations. Some of these with a different goals. The objective mainly is to identify an strange behaviour of the wave through signals. Nevertheless, valuable information about the seriousness of the imperfection of the material is not given. Similarly, Lamb wave mode proven to be a powerful tool to overcome the lack of information previously mentioned. Using the dispersion relationship provides data that other UGW not. Furthermore, the new technology and advantageous of EMAT shown to be capable of produce many types of UGW. Using the correct configuration of components, clean lamb wave modes can be excited and read.

Chapter 3

Ultrasonic Guided Wave Tomography Theory

In this chapter, the principles of the Ultrasonic Guided Wave Tomography, will be presented. First, theoretical background regarding on developed algorithms for tomography using UGW are explained, highlighting strengths and weaknesses. Second, previous work where such algorithms were implemented are given, as well as gaps in the research. Third, the proposed algorithm is presented, explained and illustrated.

3.1 Theoretical Background

As mentioned previously, the estimation of thickness using guided waves is of high interest. The capacity to know the remnant thickness of a section of interest gives a high knowledge of the integrity of the pipeline. Moreover, in the case of a defect present in the pipe wall, the suspension of operation or the quick maintenance action due to high risk of an accident may be crucial to avoid costly economic losses and high repair costs. More importantly, high environmental damage could also be prevented. Techniques for detection and estimation of the defect severity have been developed in recent years.

3.1.1 Algebraic Reconstruction Technique and Simultaneous Iterative Reconstruction Technique

The Algebraic Reconstruction Technique (ART) is a technique used for defect detection. The ART is an iterative method, which generates reconstruction via an iterative process, beginning with an initial estimate of the object to be reconstructed. It improves on this initial estimate via a sequence of estimates that presumably converge to an optimum reconstruction after a number of iterations [32]. The ART was first introduced in [33], where the technique was developed to reconstruct three-dimensional objects from electron micro graphs at different positions and X-ray photography. Later, a generalized ART algorithm was introduced in [32]. The generalized ART algorithm was used to solve the so-called inverse problem or also named reconstruction of an object based on its projection or data obtained. In this work the ART was generalized to diffraction tomography and compared with the filtered backprojection algorithm. Results demonstrate that the generalized ART algorithm achieved better results when the number of views was small.

The method consists of a series of N projections from the i transmitters to the j receivers. The transmitters and receivers were positioned in a setup covering the area of interest. This setup creates pairs of transmitter-receiver $[i, j]$. In the area of interest a mesh of certain size is created to represent the pixels $p[m, n]$ of the image to be created. In order to apply this technique, the rays are assumed to be straight lines from transmitters to receiver, creating a ray path. The ray path $ray[i, j]$ of the wave excited by the transmitters i travels along the mesh, crossing x number of pixels $p[m, n]$ until reaching the receiver j (Fig. 3.1) [12].

The time the wave spends crossing each pixel is $t[i, j, m, n] = l[i, j, m, n]/v[m, n]$, where $l[i, j, m, n]$ is the length of the $ray[i, j]$ that is in the pixel $p[m, n]$ and $v[m, n]$ being the constant velocity in the $p[m, n]$. The velocity is assumed constant to be able to detect variation. The total TOF $T[i, j]$ is the sum of all the times $t[i, j, m, n]$.

$$T[i,j] = \sum_{m,n \epsilon ray[i,j]} t[i,j,m,n] = \sum_{m,n \epsilon ray[i,j]} \frac{l[i,j,m,n]}{v[m,n]} \tag{9}$$

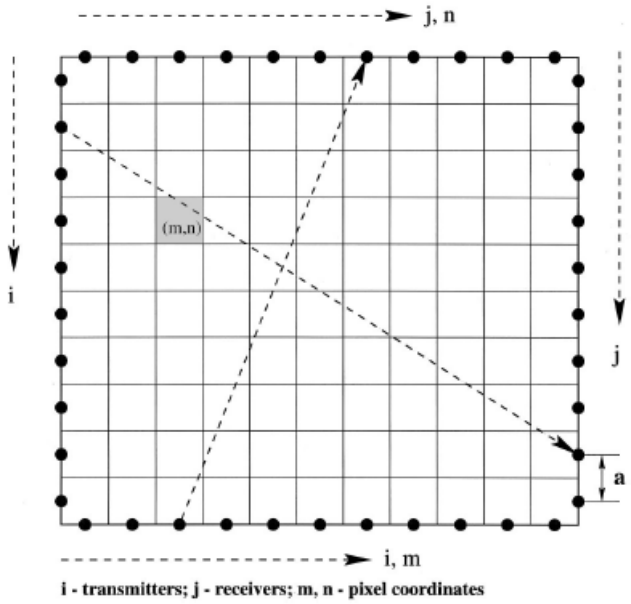

Figure 3.1: Simultaneous Iterative Reconstruction Technique representation. Image from [12].

Eq. (9) is the theoretically measured TOF from the algorithm. Knowing the arrival time in every pixel $p[m,n]$ it is possible to convert it into velocity and into thickness with the lamb wave dispersion property. Once the segments of each $ray[i,j]$ in each pixel $p[m,n]$ are calculated the iteration process begins with an initial guess of the constant velocity $v^0[m,n]$ to calculate the initial arrival time for each ray

$$T^0[i,j] = \sum_{m,n \epsilon ray[i,j]} \frac{l[i,j,m,n]}{v^0[m,n]} \tag{10}$$

Secondly, for each ray the updated velocities in the pixels containing that ray are calculated:

$$\Delta \frac{1}{v_{m,n \epsilon ray[i,j]}[m,n]} = \frac{T[i,j] - T^0[i,j]}{L[i,j]} \tag{11}$$

Where, $L[i,j]$ is the total length of the $ray[i,j]$ and $T[i,j]$ is the arrival time of the wave experimentally measured. Third, the difference in the velocity calculated in the second step is added to calculate a new velocity called v^1, which will be used for the next iteration.

$$\frac{1}{v^1[m,n]} = \Delta\frac{1}{v[m,n]} + \frac{1}{v^0[m,n]} \tag{12}$$

The TOF is measured in two cases, without and with a defect. The data from the first case is compared with the algorithm to measure accuracy. The TOF measurements from the case with defect added is then taken into account in the second step of the iteration to obtain a difference in the arrival time.

The SIRT is very similar to the ART. However, there is a small difference. The ART updates pixel velocities ray by ray while the SIRT only updates velocities at the end of every iteration. This difference eliminates noise in the image produced by the ART algorithm called "salt and pepper" for its similarity to salt and pepper. Thus, such modification leads to the SIRT, which produces better quality images with less noise. Moreover, the ART and SIRT works for a variety of scanning geometries, not necessarily square arrays. [12].

3.1.2 Simultaneous Iterative Reconstruction Technique for Image Reconstruction

The Simultaneous Iterative Reconstruction Technique is commonly used in electron tomography for image reconstruction. In [34] a modified SIRT named Dimensional Reduction Simultaneous Iterative Reconstruction Technique (DR-SIRT) is proposed as a solution for the Electrical Resistance Tomography (ERT) problems. Tests are carried out in a full configuration setup of transducers. Voltage data is taken in both cases and compared to check if non identify objects are present within the inspection area. Results showed that when increasing the number of electrodes, the image is more accurate. Moreover, comparison in experimental readings between SIRT and DR-SIRT showed that the error using SIRT was 23.8% and using DR-SIRT was 9.73%. Therefore, an addition to the SIRT algorithm has proven to produce better results. In [35], a masked SIRT was presented to obtain more accurate results. A mask filter was used to obtain more accurate values than using only the SIRT algorithm, such values were used in other algorithms to obtain an image reconstruction. Thus, with a modification to the SIRT algorithm better results were

obtained. Similarly, in [36] another addition to the SIRT algorithm is presented. The algorithm presented produced images of higher quality, reducing blurring of the obtained images from the SIRT algorithm.

3.1.3 Fast Marching Method

The Fast Marching Method was first introduced in [37] as a numerical algorithm to describe the evolution of an expanding closed region through a set of points. The Fast Marching Method gives a solution for the Eikonal equation, mathematically expressed as Eq. (13) [38].

$$|\Delta u(x)| = F(x) \ \ in \ \ \Omega, \quad F(x) > 0 \tag{13}$$

$$u = g(x) \ \ on \ \ \Gamma \tag{14}$$

Being Ω, a 2D or 3D space, u is equal to the known function $g(x)$, which is the expanding interface at its initial state in the mesh Γ in Ω and$F(x)$, the new function created by the evolved $g(x)$.

In other words, for the FMM to describe the expanding front of a closed surface, it separates the interior and exterior region. The interior region expands through time. The points inside the region have been computed and have a time at which the expanding front reaches such points. The propagating front in Fig. 3.2 is the selected area of points to be computed. The exterior region includes the points that will be computed when the wave front reaches them [39].

The algorithm performs several iterations until the data obtained from it is equal to the data measured in the experimentation. The arrival times of the waves produce group velocities from which thickness can be calculated with a fixed frequency. The FMM computes for every point in the grid (x,y) the time T at which the wave has traversed (Fig. 3.2). As the wave front proceeds across the grid, the FMM selects the point in the narrow band of points that minimises the time increment, given the values of its neighbours and their speed values. The results of the FMM is the

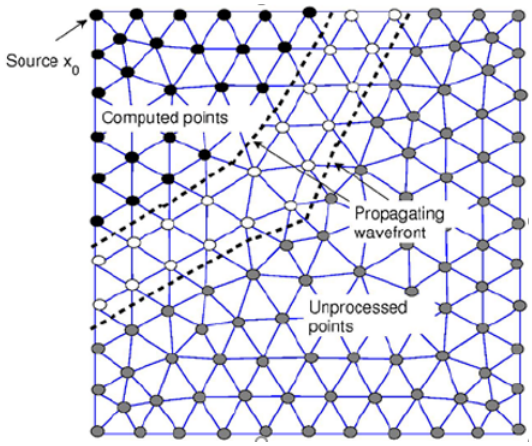

Figure 3.2: Fast Marching Method visualisation. Image from [39].

TOF image [40]. A deeper explanation of the implementation of the Fast Marching Method as well as derivatives and higher accuracy methods are described in [39].

3.1.4 Fast Marching Method in Ultrasound Tomography

In the past, the Fast Marching Method has been used for defect detection. For its effectiveness and accuracy, the FMM was selected to replicate the wave propagation of Ultrasonic Guided Waves traveling through a pipeline in [11]. In this case, being a pipeline with high curvatures, the array of sensors is in a ring configuration and the ray paths of the waves are not in a single direction. The rays take the shortest path, in some cases traveling in two directions (Fig. 3.3a). The FMM takes into consideration the helical path of the rays, solving this issue. Fig. 3.3b illustrates the helical ray path that the FMM computes. Instead of computing it in the normal way as a matrix going downwards, it calculates the ray path in the other direction due to the distance being shorter. That would be the travel path that the ultrasonic waves will take since they are traveling through a pipeline.

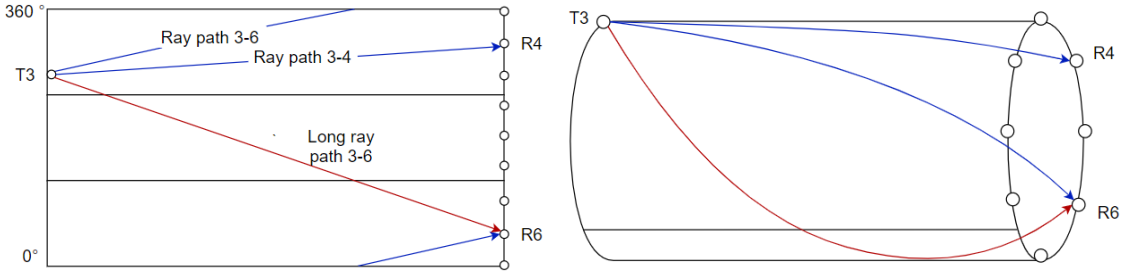

(a) 2-D helical path view

(b) 3-D helical path view

Figure 3.3: Helical path visual representation.

Fig. 3.3a shows the unwrapped pipe and in a 2D form. The transmitters are positioned on the left side and the receivers on the right side, denoted by T and R respectively. Fig. 3.3b shows the real ray path of the ultrasonic guided waves from the transmitter to the receivers and in the unwrapped form. Fig. 3.3a is the representation of the real scenario used in the algorithm of the Fast Marching Method. Due to the configuration in the unwrapped form, the construction of the ray paths from every pair of transmitters to every receiver would be as straight lines, as can be seen in the red line in Fig. 3.3a, named "long ray path 3-6". However, this scenario is not entirely accurate. The wave, being a helical wave, expands in every direction, as shown in Fig. 3.4. Therefore, the wave reaches the sensor faster in the direction of the blue line taking the helical path.

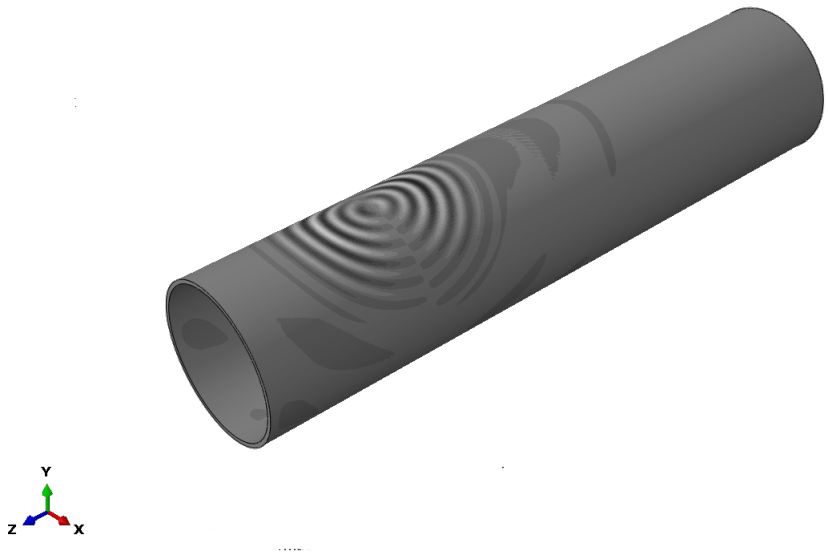

Figure 3.4: Helical wave propagation in a simulation

Continuing with past work, in [41], the Fast Marching Method has been used to consider refraction of x ray projections in ultrasound tomography for breast cancer detection. Using the FMM in this case, generates more accurate TOF data and thus a more accurate reconstructed image. Similarly, the FMM was used for the same purpose as the consideration of the refraction, also called bent-rays, in an ultrasound tomography for defect detection of a plate in [42]. The FMM was used as the first stage of reconstruction of the Hybrid Algorithm for Robust Breast Ultrasound Tomography (HARBUT)

3.2 Proposed FMM-SIRT

Having examined the benefits of the algorithm mentioned before, in this work we propose to make use of two different algorithms to overcome the difficulties of each. Making use of the Fast Marching Method, we can explain better the wave propagation in a circumferential surface (pipeline) and take into account the bent rays and helical path to obtain more accurate results compared to those obtained in simulations and experimentation. Moreover, the use of the SIRT and its ability to adapt the algorithm to a vast nature of geometries, as well as its effectiveness at reducing noise and producing good quality images, will improve the final results.

In Fig. 3.5 a flow chart of the proposed algorithm is shown. First, the FMM is implemented, results TOF results are obtained taking into account the bent-rays and the helical path. Making the results more accurate for the configuration of the object used in this research. If the TOF is not equal, the FMM is not describing the propagation of the waves properly as it should be and changes must be made. Otherwise, if the TOF obtained from the FMM are equal or very similar to the baseline TOF measurements a TOF image is printed. The TOF image contains a TOF measurement saved in every pixel of the image. Now, at this point is where the SIRT is implemented. The TOF from the FMM is used to calculate the difference in time of the waves and the difference is backpropagated using the TOF image that already considers the helical paths and the bent rays in their calculations. If the new TOF obtained from the backpropagation is not equal to the TOF from the data a new iteration is carried out with this new TOF obtained from the previous iteration. Moreover, if it is correct, the TOF image is saved, converted into a velocity image. Finally, the velocity image is converted into a thickness image and it is printed as a result.

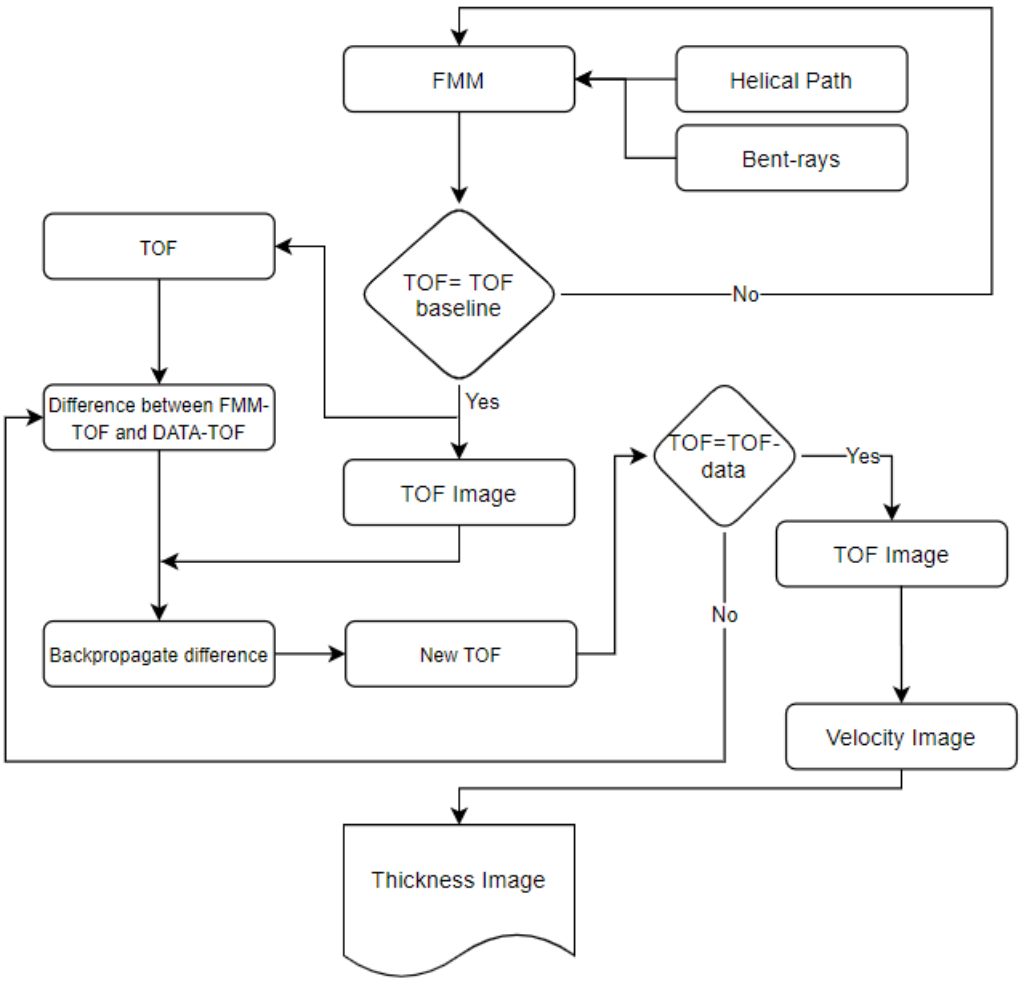

Figure 3.5: FMM-SIRT flow chart

Chapter 4

Simulation Setup

Plenty of software exists to construct different types of models and run various simulation setups in various scenarios. The selection of the proper software for the simulations has been carried out in the research. Several past works in the area, working with EMATs, Ultrasonic Guided Waves and Ultrasound tomography of objects of interest for defect detection, used similar software. The most used software for the simulation of wave propagation at different frequencies in different objects of various materials is Simulia ABAQUS/CAE. We have selected ABAQUS/CAE for its popularity in wave propagation simulations in the area of NDT/NDE.

4.1 Software

ABAQUS/CAE is a software developed by Dassault Systems. The software uses nonlinear finite element analysis to provide different solutions for mechanical, structural, civil, biomedical, and related engineering applications. The main platform of the software can be seen in Fig. 4.1, where it is possible to create the parts of a model from the beginning or import drawings from CAD and SolidWorks and work with them. ABAQUS is a software where the user can create, modify and add materials, dimensions of elements, apply loads in specific points, add boundary conditions, and extract specific data from specific points of the model.

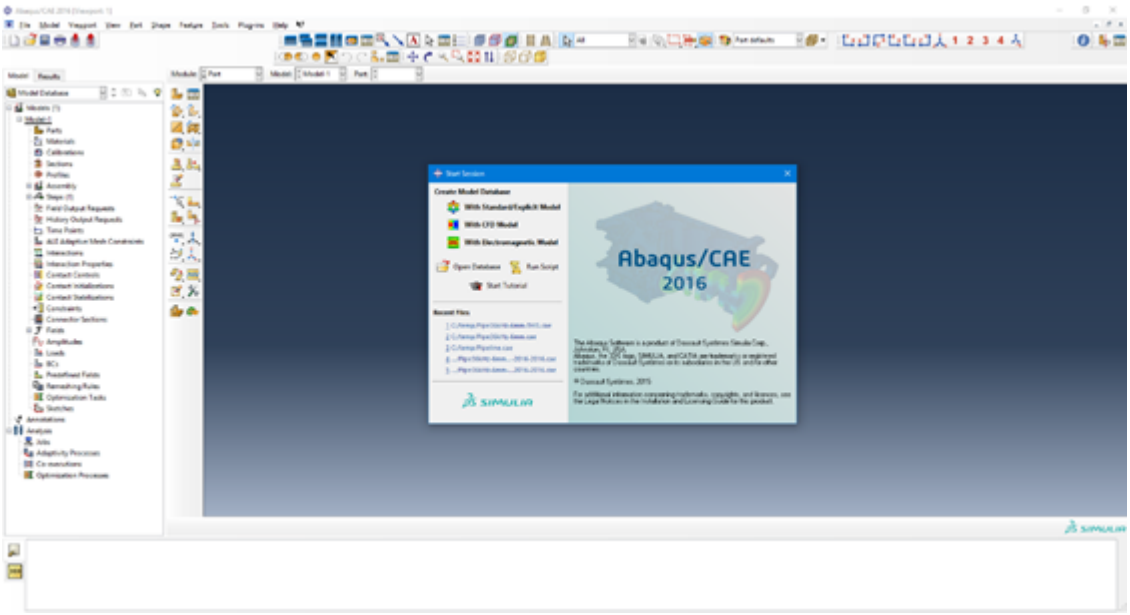

Figure 4.1: Simulia ABAQUS/CAE platform

It is also capable of simulating and creating a visualisation of different scenarios, such as a fluid flowing through a pipeline, collisions of two objects, wave propagation, etc. (Fig. 4.2). The main purpose of using ABAQUS/CAE is to simulate the wave propagation produced by the EMAT, extract the data in the receivers position for further analysis, and process it to identify imperfections in the object inspected. For our purpose, the object of interest is a steel pipe.

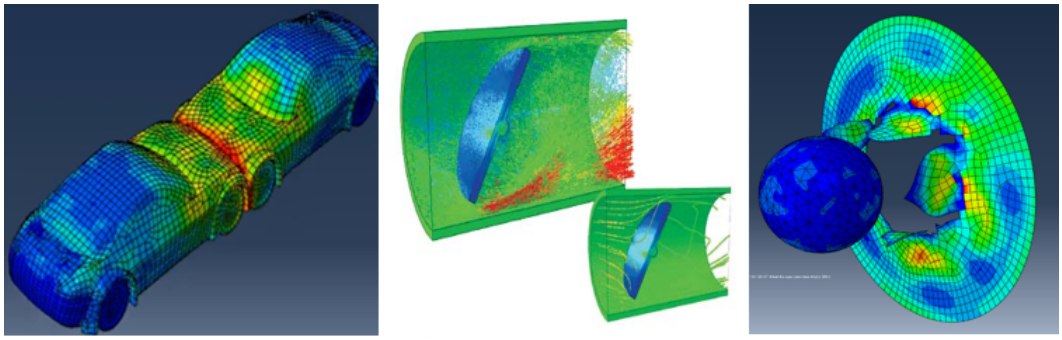

Figure 4.2: Different possible scenarios to simulate in ABAQUS/CAE

4.1.1 Simulation Setup: Pulse-Echo Mode

A first simulation has been carried out to validate simulation. The model has been replicated from [15]. The steel pipe for the simulations has an outer diameter of

114 mm and an inner diameter of 108 mm. The steel has a density of 7800 $kg/m3$, Young's modulus of 209 GPa and Poisson's modulus of 0.28, in order to produce a Torsional $T(0,2)$ wave mode. The operation mode is in Pulse-Echo, referring to a single set of sensors working as transmitter and receivers. The sensors transmit the signal and after that read the reflection of the wave with the defect. The setup of the sensors can be seen in Fig. 4.3. Sensor 1 (S1) is in the outer surface of the pipe, Sensor 2 (S2) is located in the middle of the thickness and Sensor 3 (S3) is at the inner surface of the pipe. The main purpose of this model is to validate simulation replicating results obtained and corroborated with experimentation in [15].

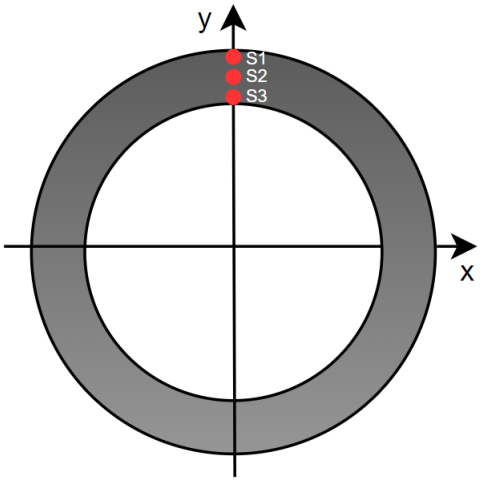

Figure 4.3: Sensors position in the simulation setup pulse-echo mode

Sensors are placed at 25 cm from the left end of the pipe, as shown in Fig. 4.4a. The torsional $T(0,2)$ is produced with a pulse-time signal of 5 cycles at a center frequency of 36kHz and a maximum force value of 100 N. The area in which this force is applied extends 0.2 cm from the left end (Fig. 4.4a). The step time of the simulation is $2.0\mu s$ and the total time of the simulation is $80ms$. The mesh size is $4mm$, 5 to 10 times smaller than the wavelength of $30.5mm$ to correctly appreciate the displacement of the wave (Fig. 4.4b). A frame of the simulation is presented in Fig. 4.4c. Frame 223 in the simulation, where it is clearly visible, is the torsional wave traveling in the negative z direction.

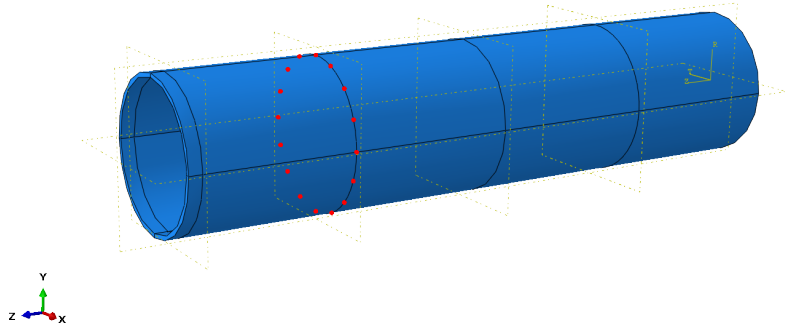

(a) Sensor positions

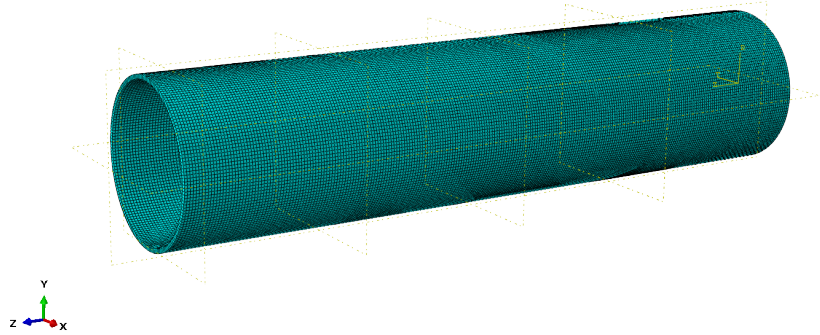

(b) Mesh visualization

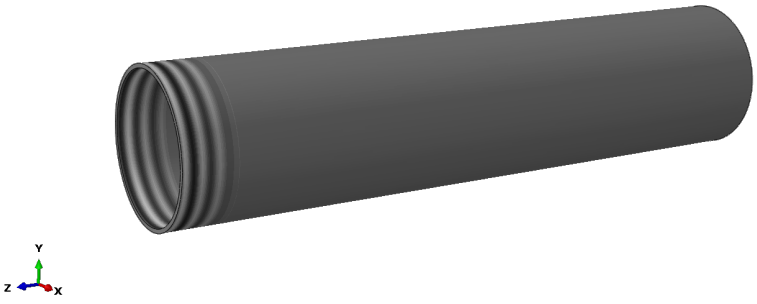

(c) Wave propagation of the T(0,2)

Figure 4.4: Different views of the first pipeline model. (a) Sensor positions in the simulation setup pulse echo. (b) Illustration of mesh size of 4mm in pipeline model. (c) Wave propagation of the T(0,2) at increments of 223/1646 of the simulation.

Four cases with different defects have been simulated to compare results from the readings of sensors S1, S2 and S3 and check the reliability of the software towards changes in the geometry and the effect on the signals. The different defects can be seen in Fig. 4.5. Fig. 4.5a is the baseline case, the pipeline with no defects added. Fig. 4.5b is a rectangle in the axial direction of 200mm long and 50mm wide. Fig. 4.5c is a small rectangle in the x direction with dimensions 40mm long and 2mm wide. Fig. 4.5d is a hole with a 10mm radius.

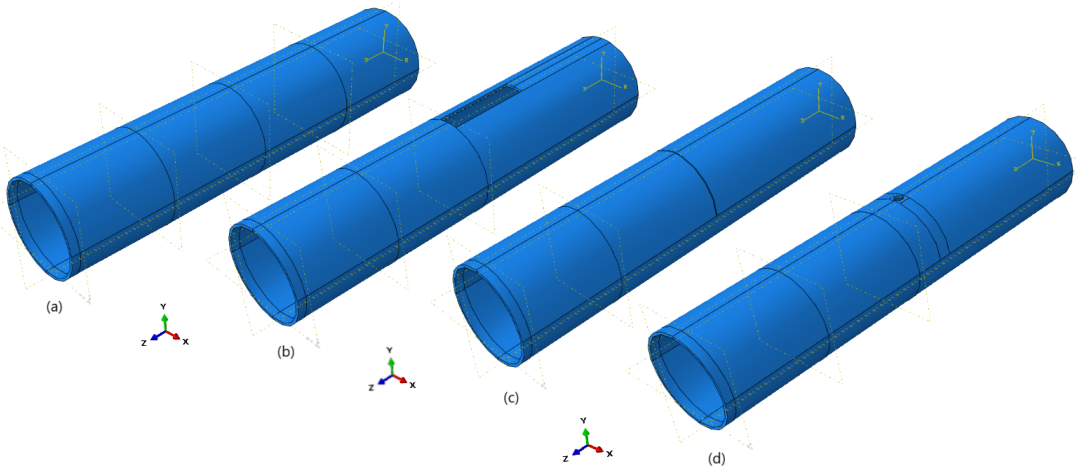

Figure 4.5: Various defects added to the pipeline model. (a) pipeline with no defect. (b) wide rectangle in axial direction. (c) small rectangle in x direction. (d) hole.

The wave propagation through the four cases can be seen in Fig. 4.6. In Fig. 4.6a the first steps of the simulation are shown where the wave is produced and starts to propagate in the -z direction. In Fig. 4.4b it is noticeable that the torsional wave is at the moment when it reaches the defect. Finally, in Fig. 4.6c the defect has reflected some energy of the traveling wave, which travels in the opposite direction to the original wave. However, the original wave preserves its original direction. When the reflected wave reaches the line of sensors, the displacement data of the particles in the pipe under the sensor position is recorded.

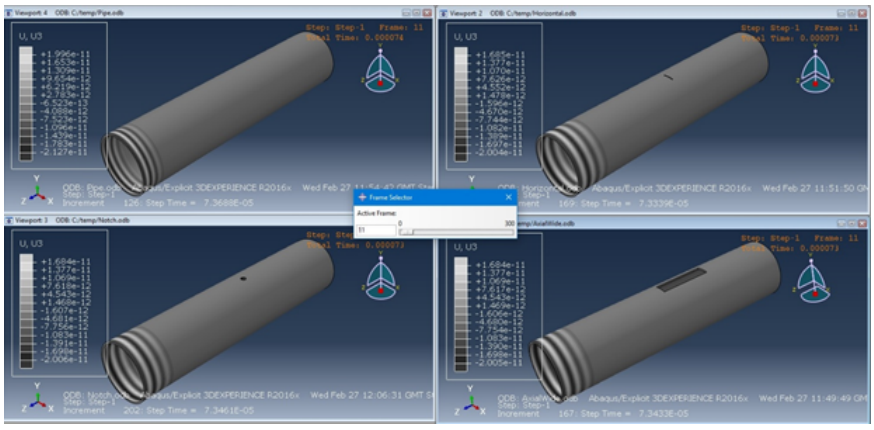

(a) Frame 11/300.

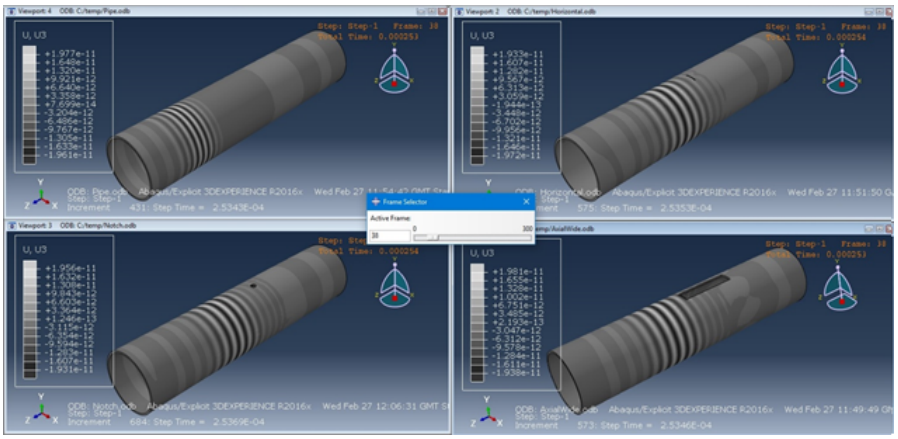

(b) Frame 38/300

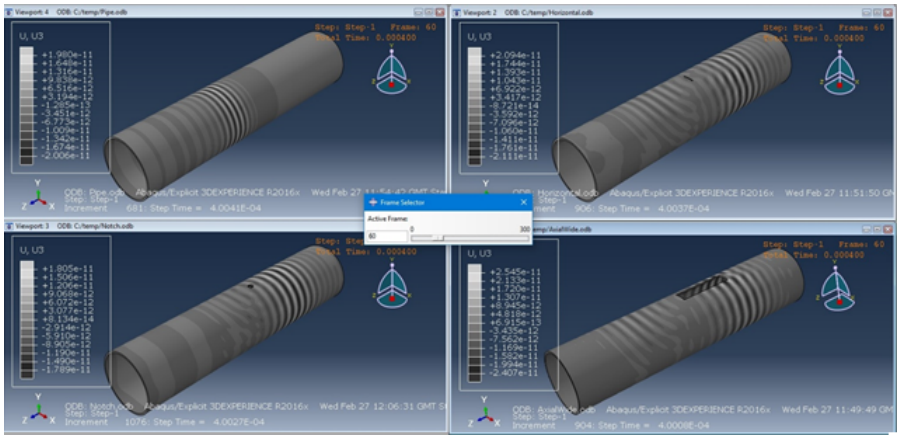

(c) Frame 60/300

Figure 4.6: Simulation of torsional wave propagation with 4 different defects. (a) Early stage of simulation when the wave starts to propagate. (b) Moment when the wave reaches the defect. (c) Moment when part of the energy carried by the wave bounces back.

4.1.2 Simulation Setup : Sixteen Ring Setup

The next simulation carried out work under the principle of through-transmission. A ring of sensor transmitters are placed at 25cm from the left end and the ring of receivers are placed at 25cm from the right end (Fig. 4.7). The purpose of this setup is to perform an ultrasonic tomography to the object inspected. As mentioned in the previous chapter, a tomography is a reconstruction of an object based on its projections. In this case, an ultrasonic tomography is a reconstruction based on the received signals in the receivers. The set of rings builds pairs of every transmitter with every receiver. Every transmitter will transmit the same signal at a different time and the readers will acquire the signal from that transmitter. This sequence is followed until all the transmitters have completely transmitted the signal. The total readings for all Transmitter-Receiver (T-R) pairs is 256. Material properties, step time, step increment and mesh size are the same as the previous simulation mentioned.

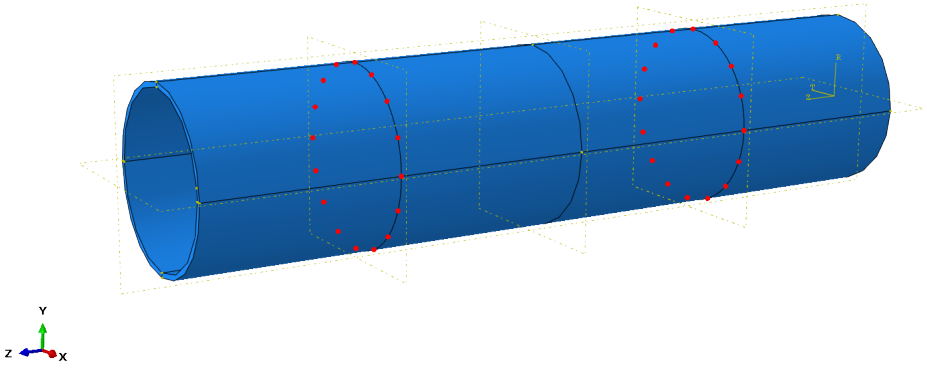

Figure 4.7: Sensor positions in the simulation setup pulse-echo mode

A new sensor arrangement has been implemented for better data organization. The sensors have been named as the cardinal point and the angle at which the sensor is positioned. The angles only range from 0-90°and the angles used are 22°, 45°and 68°. The cardinal points are North (N), East (E), West (W), South (S), Northeast (NE), Northwest (NW), Southwest (SW) and Southeast (SE). The sensor arrangement can be seen in Fig. 4.8.

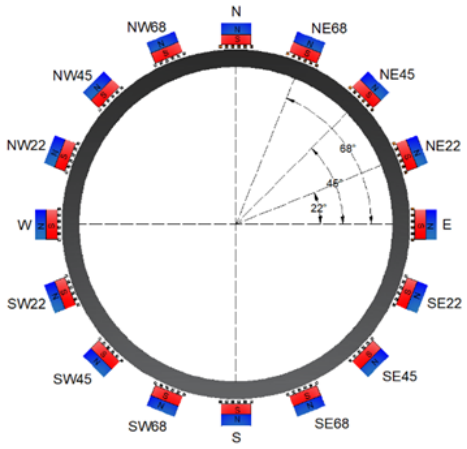

Figure 4.8: Sensor position in the simulation setup pulse-echo mode

A couple of simulations are shown in Fig. 4.9. The wave produced in this simulation is the Lamb wave A0 wave mode at 50kHz. The four simulations shown in Fig. 4.9 are only 4/16 simulations for the baseline model. In Fig. 4.9a the sensor "N" transmits the five cycle signal at a central frequency of 50kHz. In Fig. 4.9b the sensor "E" is the transmitting sensor. The sensor "W" is shown in Fig. 4.9c. Finally, in Fig. 4.9d the sensor "S" is shown. Data has been recorded with the ring of receivers and imported into MatLab for processing and implementation of the algorithm.

Once the simulation data of the baseline model is gathered, the defect is added to the model. The same excitation sequence of the wave as in the baseline model has been carried out and data has been acquired for the damaged model. The defect added is a hole-type defect of 2.5mm radius. This radius has been selected from examination of the past simulation data. The data from simulations has demonstrated that the larger the defect, the higher is the energy reflected. In addition, defects in real life are small cracks due to corrosion. However, for simplification of the simulation and minimize distortion of the wave, a symmetrical hole is used with the purpose of obtaining less disperse data to test the algorithm. The defect can be seen in Fig. 4.10

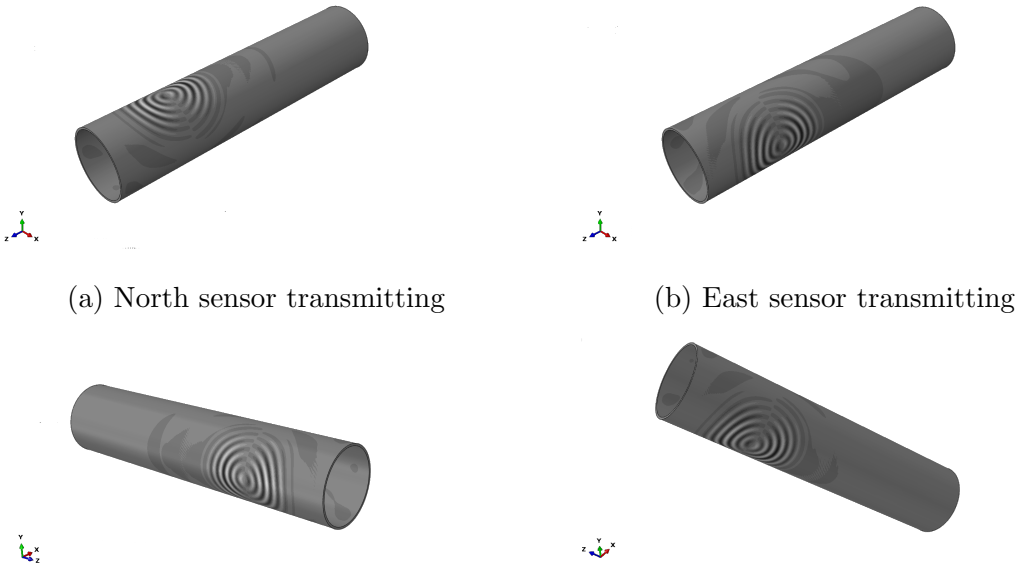

(a) North sensor transmitting

(b) East sensor transmitting

(c) West sensor transmitting

(d) South sensor transmitting

Figure 4.9: Simulation visualization. (a) North (N) sensor transmitting. (b) East (E) sensor transmitting. (c) West (W) sensor transmitting. (d) South (S) sensor transmitting.

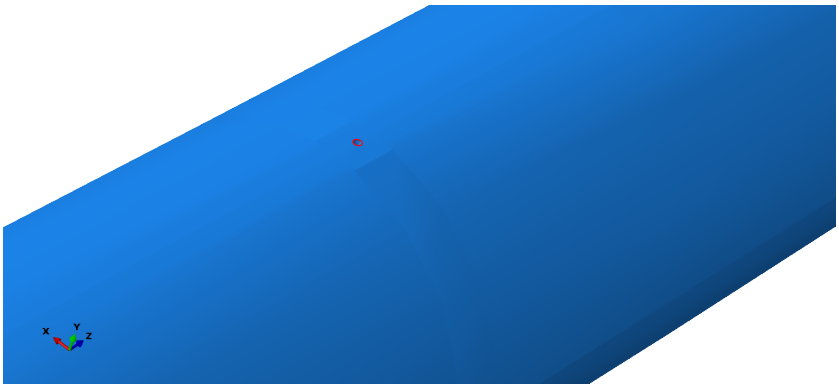

Figure 4.10: Hole type defect used for simulations.

4.1.3 Simulation Setup : Eight Ring

The simulation setup of a ring of eight transducers has some differences. Transmitter and receiver rings are identical to the simulation with a 16-ring setup. The ring setup of this simulation can be seen in Fig. 4.11. The sensors at the angles of 22° and 68° have been suppressed due to space. The outer diameter of the pipeline is 50mm and the inner diameter is 48.3mm

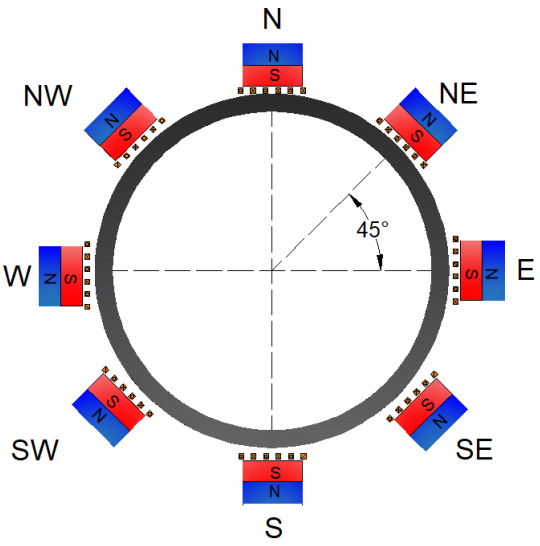

Figure 4.11: Sensor arrangement of 8 ring setup

The model built for this simulation can be seen in Fig. 4.12. In Fig. 4.13a the sensor position is shown. The eight-sensor ring in the arrangement is used for transmitters and receivers. The mesh size in Fig. 4.13b is the same size as previous simulation of 4mm for a good vision of the wave at its high and low points. In Fig. 4.12c a preview of the simulation using the sensor "E" is shown as illustrative of the A0 lamb wave mode at 50kHz traveling through the pipeline. The model in this case appears to be longer than the past simulation. This is due to the diameter of this model being significantly reduced, whilst the longitude remains at 1 meter.

The simulation sequence or procedure of the simulation is the same as the simulation with a 16-sensor ring setup. Following this sequence, the total data acquired are one reading in every receiver for each transmitter in use. A total of 64 signals have been obtained and exported to MatLab for further processing.

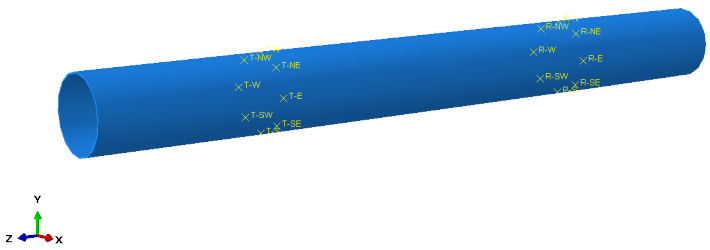

(a) Sensor positions

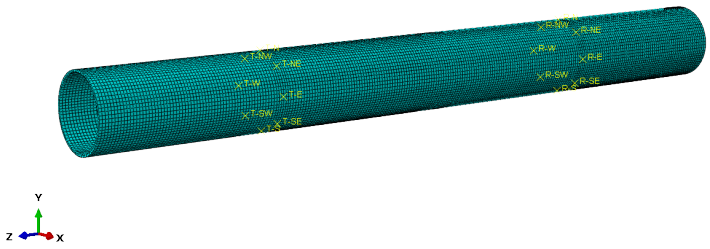

(b) Mesh visualization

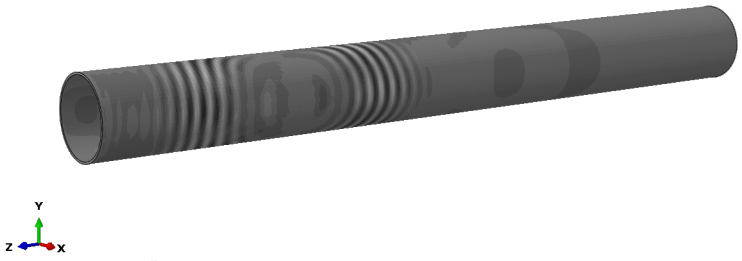

(c) Wave propagation of the A0

Figure 4.12: Different views of the first pipeline model. (a) Sensor positions in the simulation setup of 8 sensor ring (b) Illustration of mesh size of 4mm in pipeline model. (c) Wave propagation of the A0 Lamb wave mode at increment of 538/2497 in the simulation

4.1.4 Simulation Setup: Corrosion Defect Added

In the simulation setup of 8 sensors of EMATs, a defect simulating corrosion has been added to the model. The defect is illustrated in Fig. 4.13. A geometric curve has been subtracted from the entire volume of the pipeline model. The curve represents a growing volume loss as it reaches the deepest point. The defect is 1mm deep, 10.5mm long (z-axis), and 20mm wide (x-axis). It is located at the mid-point between the transmitter ring and receiver ring. A total of 64 signals have been obtained and exported to MatLab for further processing of the information.

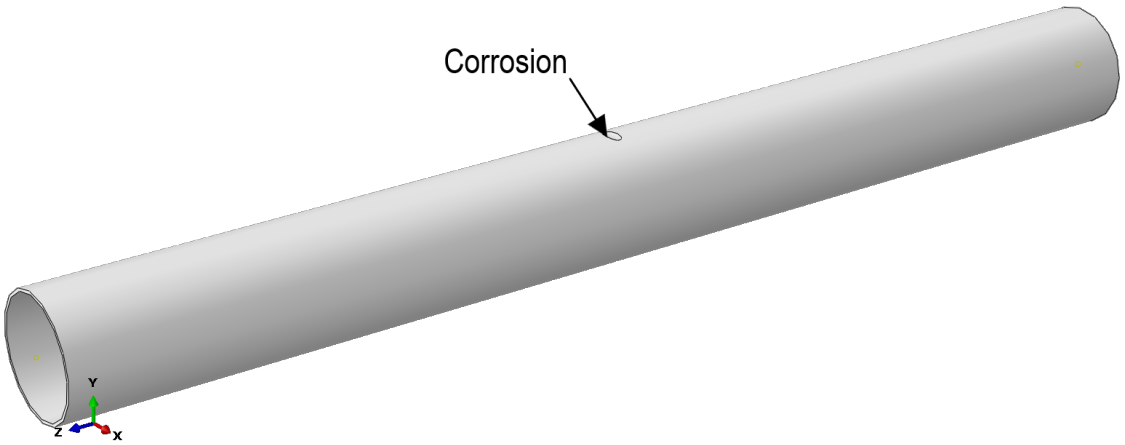

(a) Defect location

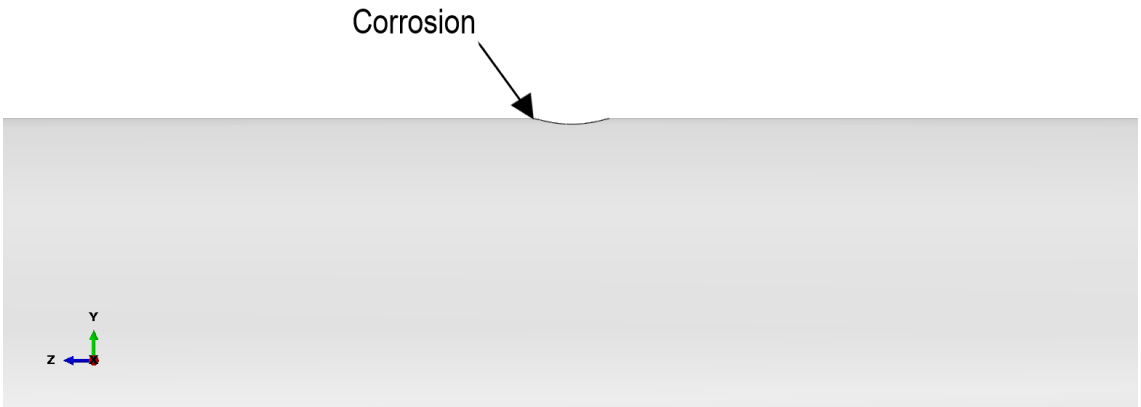

(b) Defect curve visualisation

Figure 4.13: Corrosion defect added.(a) location. (b) visualization

4.2 Data Collection

The data has been collected from the simulations mentioned above. The data is stored in the format of the displacement of the objects surface as a function of time.

4.2.1 Time Of Flight Extraction

Fig. 4.14a shows the raw signal obtained from the transmitted signal of the East (E) transmitter received by the North (N) receiver. The first visible waves in the signal at around 24μs correspond to the S0 lamb waves arriving earlier to the sensor due to its higher speed at the 50kHz of frequency used. The second wave packed in the signal at around 37μs is the A0 Lamb wave mode reaching the sensor later due to its lower speed. In Fig. 4.14b a decibel diagram measuring the decibels in y-axis for a range of frequencies in x-axis. The dominant frequency is represented by a higher value of decibels. From this figure we can see that the fixed frequency used of 50kHz for the excitation is not being received clean. In Fig. 4.14c a spectrogram of the signal is shown to identify the moment at which this frequency appears. In order to clean the data and obtain a signal with a dominant frequency of 50kHz, we applied a low-pass and high-pass filters to clean the signal (Fig. 4.15). By comparing Fig. 4.15a and Fig. 4.14a it is noticeable that the signal has a different shape. The S0 and A0 lamb waves are easier to visually identify. The S0 starts at 25μs and ends around 33μs. On the other hand, the A0 starts at 38μs and ends at 51μs. Moreover, in Fig. 4.15b compared with Fig. 4.14b we can see that frequencies outside of the range of 40-60 kHz have been suppressed due to the implementation of filters. Finally, in Fig. 4.15c the highlighted area is the sample in which the frequency is stronger. The frequency is found in y-axis while the sample number in x-axis. In Fig. 4.15c we can see that all the data is in the same frequency range (45-50kHz). In contrast, Fig. 4.14c is not in the same frequency range.

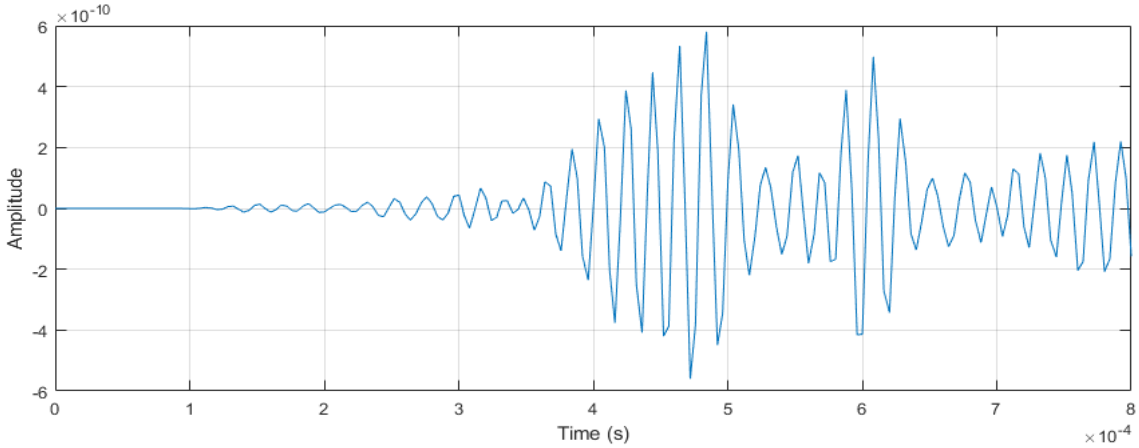

(a) Raw signal

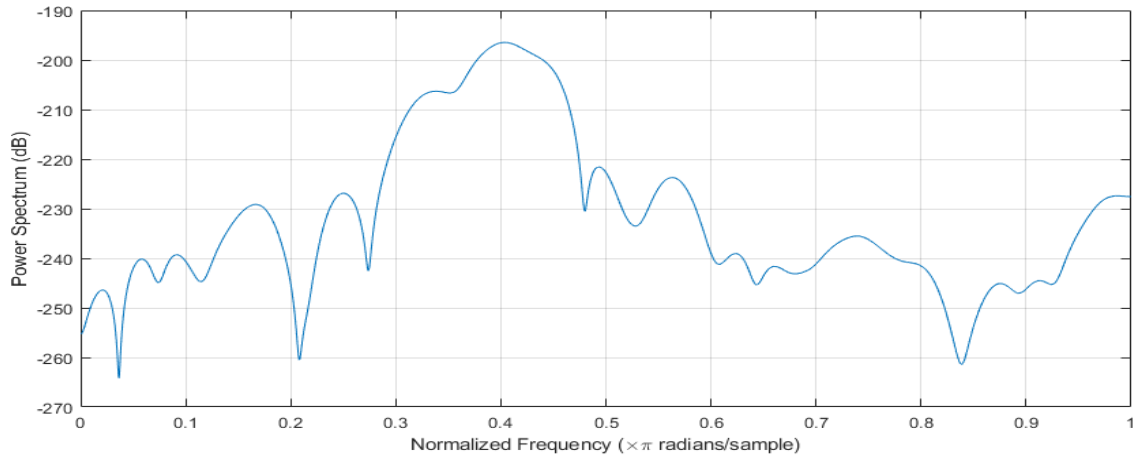

(b) dB visualization of the raw signal

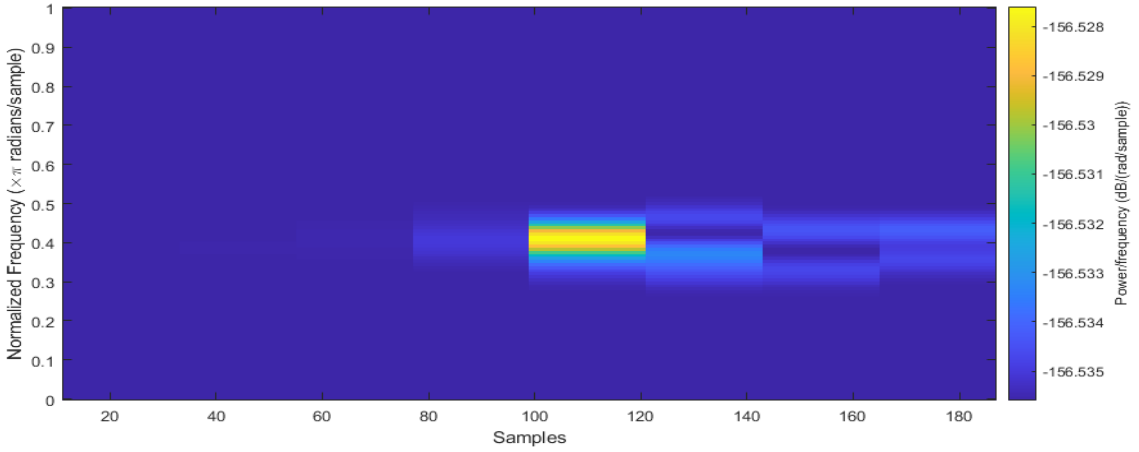

(c) Spectrogram of the raw signal

Figure 4.14: Examination of the obtained signal before processing. (a) raw signal obtained from the readings in ABAQUS. (b) dB ratio for the raw signal. (c) Spectrogram of the raw signal

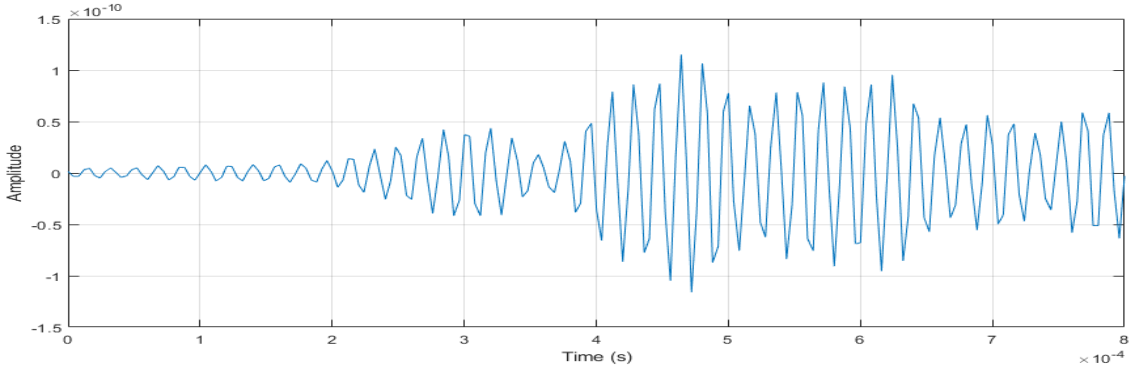

(a) Processed signal

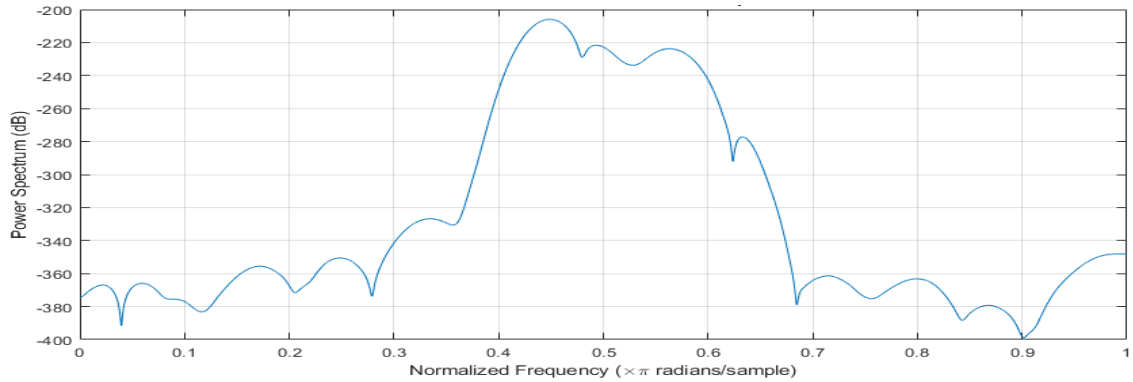

(b) dB visualization of the processed signal

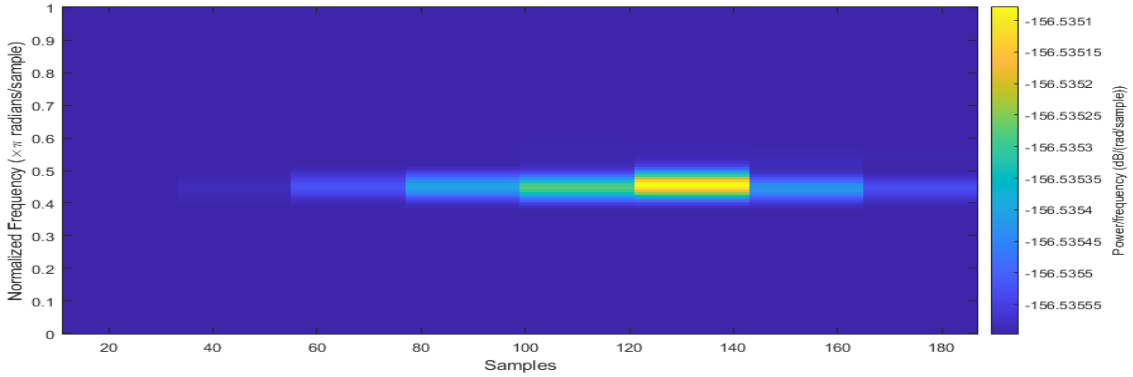

(c) Spectrogram of the processed signal

Figure 4.15: Examination of the obtained signal post-processing. (a) post-processed signal obtained from the readings in ABAQUS. (b) dB ratio for the post-processed signal. (c) Spectrogram of the post-processed signal

The arrival time of the A0 Lamb wave mode has been extracted from the signals obtained in the simulations. The wave is considered to have reached the receiver when the signal crosses the 20% of the maximum value of the Hilbert transform [11]. In Fig. 4.16 we can see the procedure, where the black line represents the 20% of the Hilbert transform of the signal, the blue line with dots represents the Hilbert transform and the red line is the signal read. At the moment of crossing, the time is extracted. This processing procedure is executed for the 256 T-R pairs in the simulation setup of the 16-sensor ring, and with the 64 T-R pairs in the simulation setup of the 8-sensor ring.

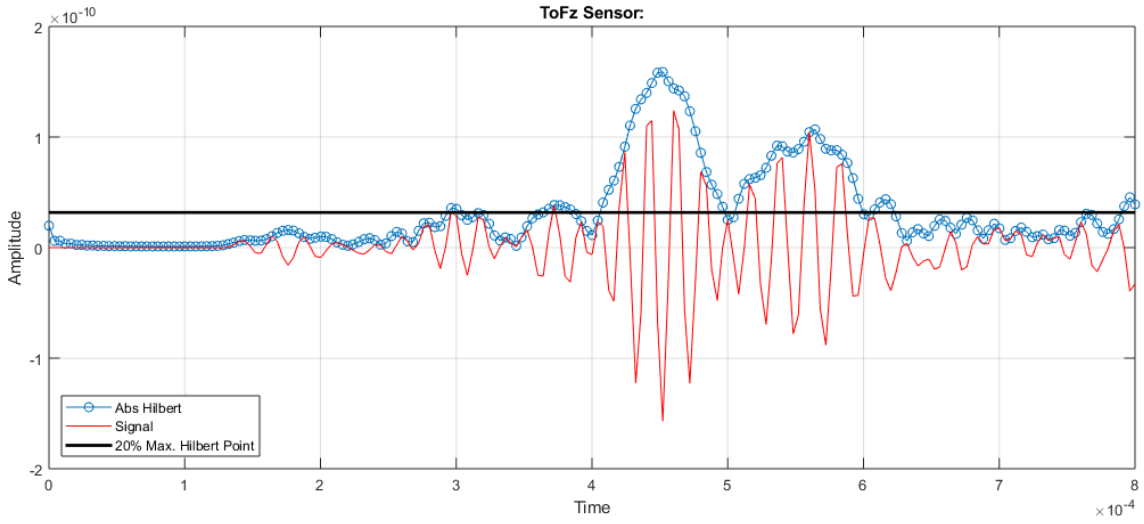

Figure 4.16: Signal obtained in sensor N from transmitter E

4.2.2 Fast Marching Method Implementation

The FMM has been used in order to obtain the TOF of every pixel of the image to be reconstructed. The TOF map or image obtained from the FMM can be seen in Fig. 4.17 and Fig. 4.18. These images represent the wave propagation of the wave transmitted from every transmitter. The algorithm creates an expanding wavefront, which starts at a certain position depending on the acting transmitter, and expands as the wave expands in reality and in simulations. Moreover, as the wavefront expands through the pixels, the time at which it reaches the pixel is recorded in the position of the pixel.

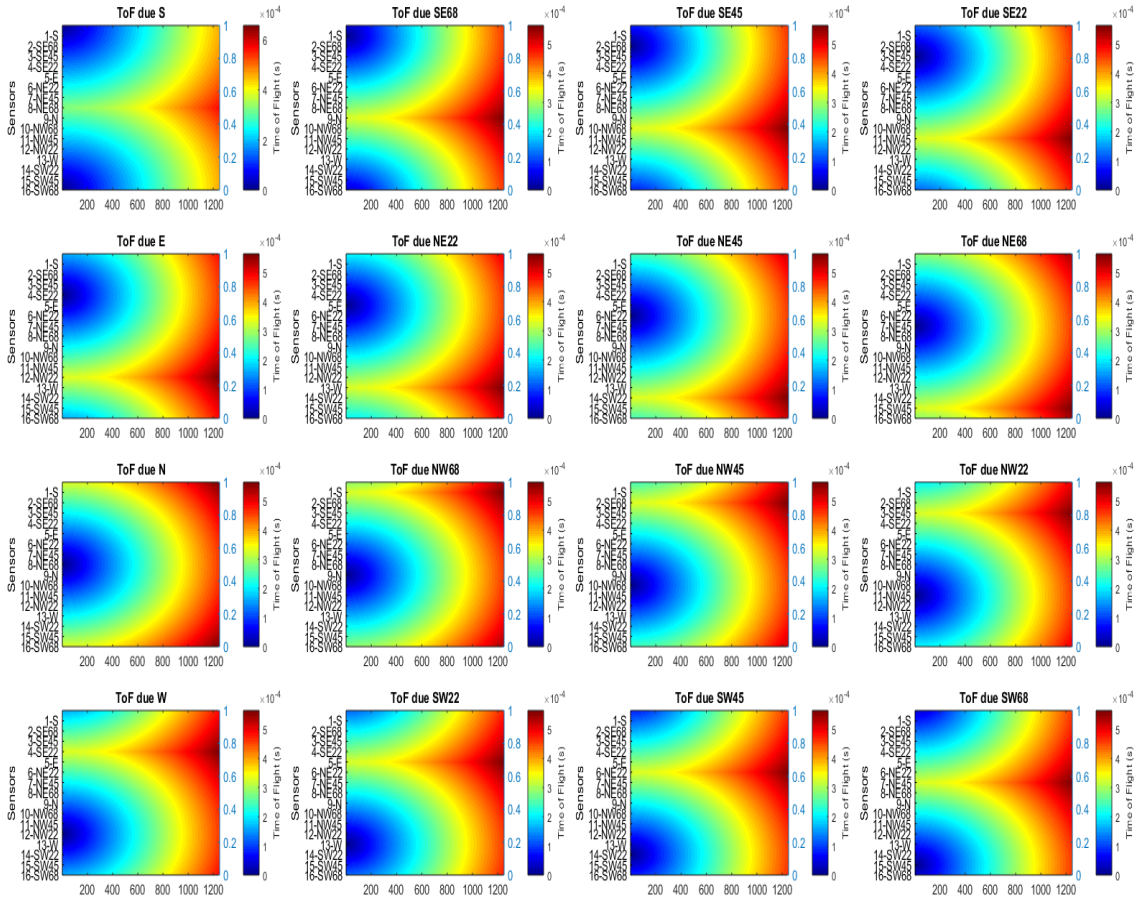

Figure 4.17: TOF of every T-R pair 16 sensor ring simulation setup defect-free

The colour of the images represents a magnitude. The relation of color and magnitude is shown in the colour bar at the right of every graph, which ranges from 0 - 50ms in Fig. 4.17 and 0 - 60ms in Fig. 4.18.

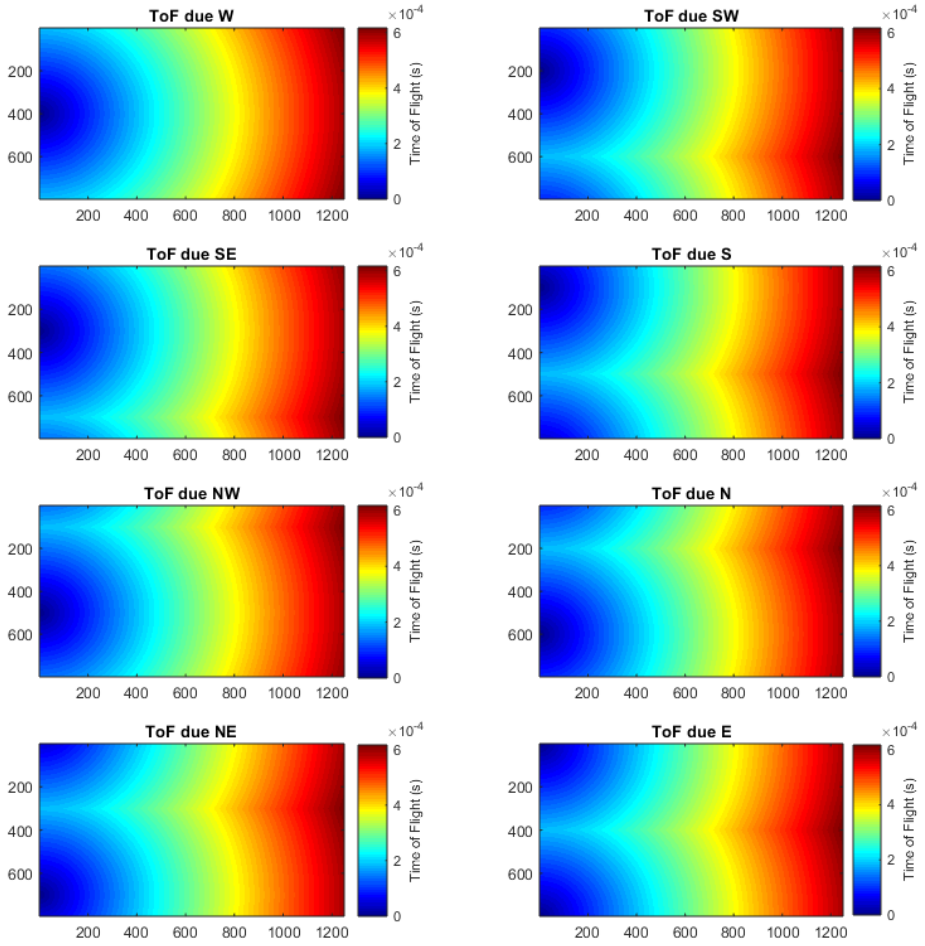

Figure 4.18: TOF of every T-R pair 8 sensor ring simulation setup defect-free

4.2.3 Simultaneous Iterative Reconstruction Technique Implementation

The computational operations of the SIRT algorithm were carried out and the ray paths of the T-R pairs were established. Every transmitter-receiver pair can be seen in Fig. 4.19. In this image, the y-axis represents pixels in the vertical position (unwrapped circumference) and x-axis pixels in the horizontal position (length). All ray paths start from the transmitter position and expand until they reach the receiver position. Moreover, the helical path and the bent rays are considered already in the FMM algorithm.

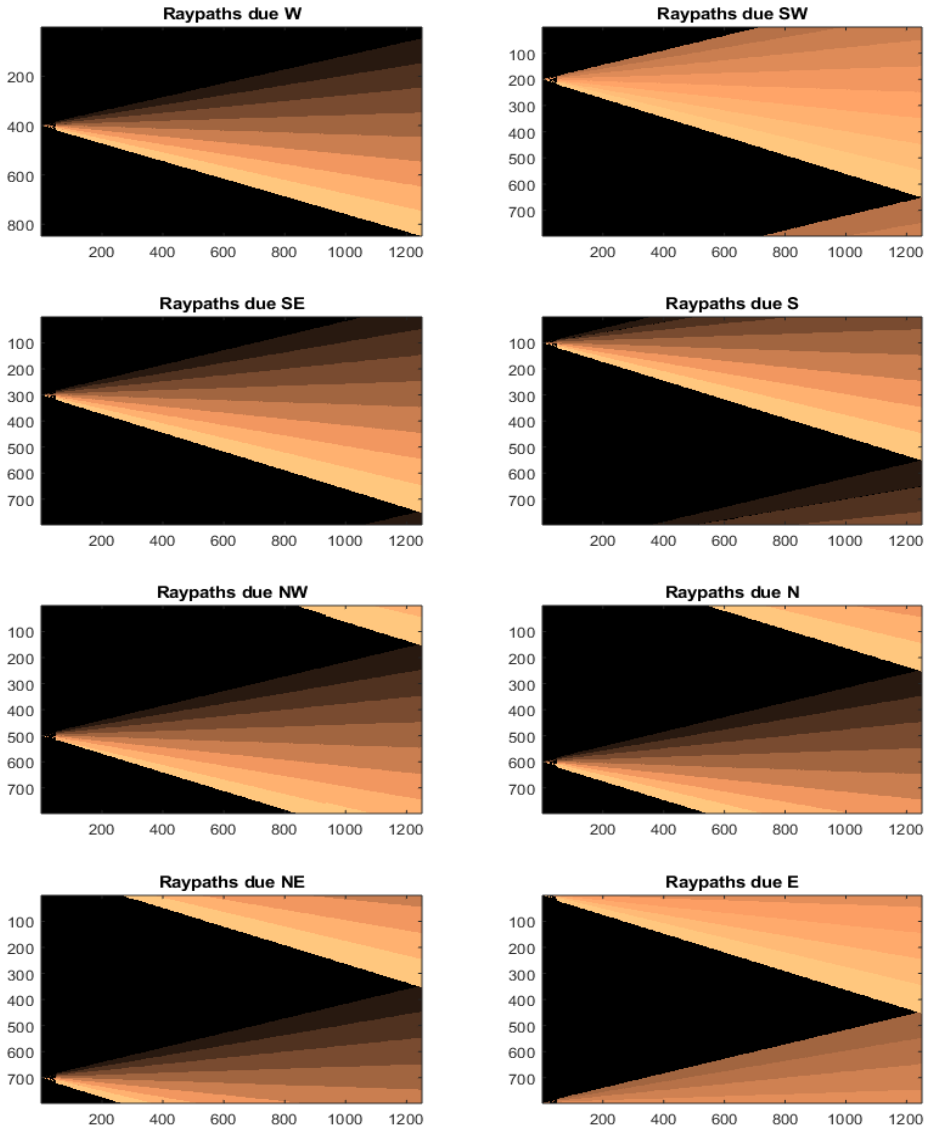

Figure 4.19: Every T-R pair of 8 sensor ring simulation setup

The pixels included in the ray path of a specific T-R pair are extracted from the TOF map obtained from the FMM. This can be visualized in Fig. 4.20. In Fig. 4.20a and Fig. 4.20b the pixels from the FMM image that are within the range of positions of any of the ray path of any T-(all receivers) pairs are extracted and used for the resulting new image shown. The difference in the arrival time of the defect free model and the presence of defect model are compared and the difference is backprojected. The pixels inside the range of the ray path of the transmitter-receiver pair will be taken into account for the backprojection for the T-R pairs. This sequence is repeated for all TOF maps from the FMM and the ray paths from the SIRT.

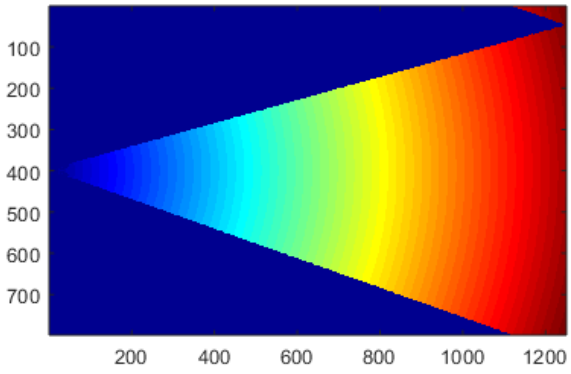

(a) Pixels contained in the range of the ray paths of transmitter N.

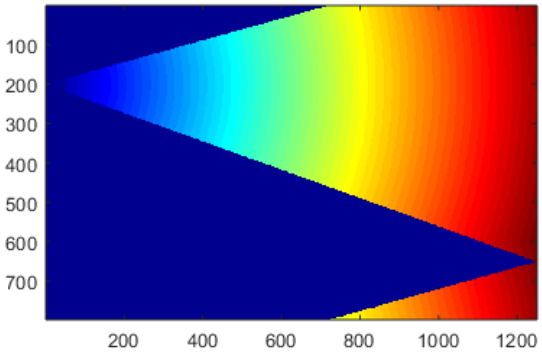

(b) Pixels contained in the range of the ray paths of transmitter E.

Figure 4.20: FMM and SIRT implementation

4.3 Results

4.3.1 Time of Flight

The arrival times extracted from the data can be seen in Fig. 4.21 to Fig. 4.24. The y axis of the graphs represents the time, and the x axis, the sensor. The curve illustrates the time at which the wave reaches the specific sensor in the x axis. In the subtitle of these figures is the name of the sensor that is transmitting the signal. In theory, the waves should reach the sensor with the shortest distance faster than the others, for example, if sensor W is transmitting, the receiver W should read the wave faster than the rest of the receivers because the distance between the W-W (T-R) is shorter. From the graphs in Fig. 4.21 to Fig. 4.24 we can conclude that they agree with this logic and measurements are correct. The valley of the curve moves according to the sensor that is transmitting. In the case of the N transmitter, the N receiver has the shortest time.

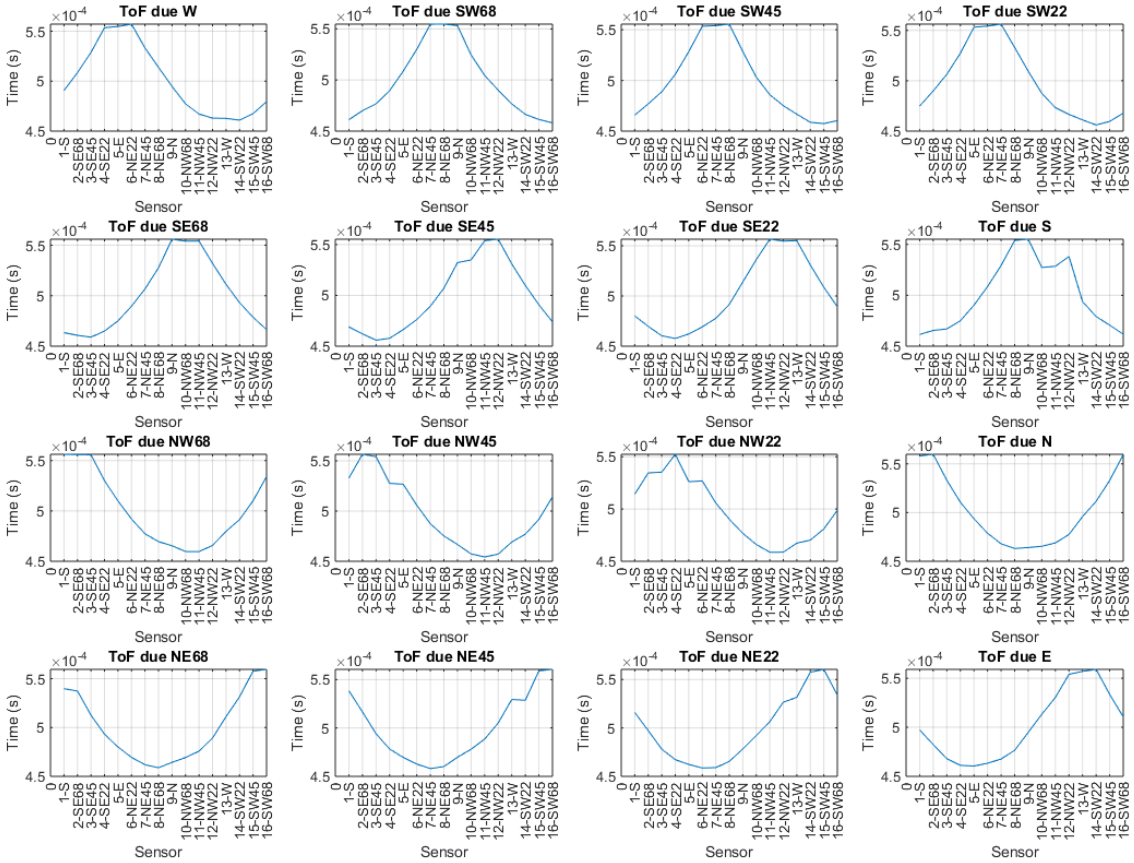

Figure 4.21: TOF of every T-R pair for 16 sensor ring simulation setup defect free.

In Fig. 4.21 the TOF from the 16 transducer ring simulation setup is shown. The curves from Fig. 4.21 are smoother in their variations than Fig. 4.22. The TOF from the 16 sensor ring simulation setup with defect added in Fig. 4.22 is higher, of the order of 50-55ms compared with the simulation with no defect added (Fig. 4.21), in which the TOF ranges from 46-55ms.

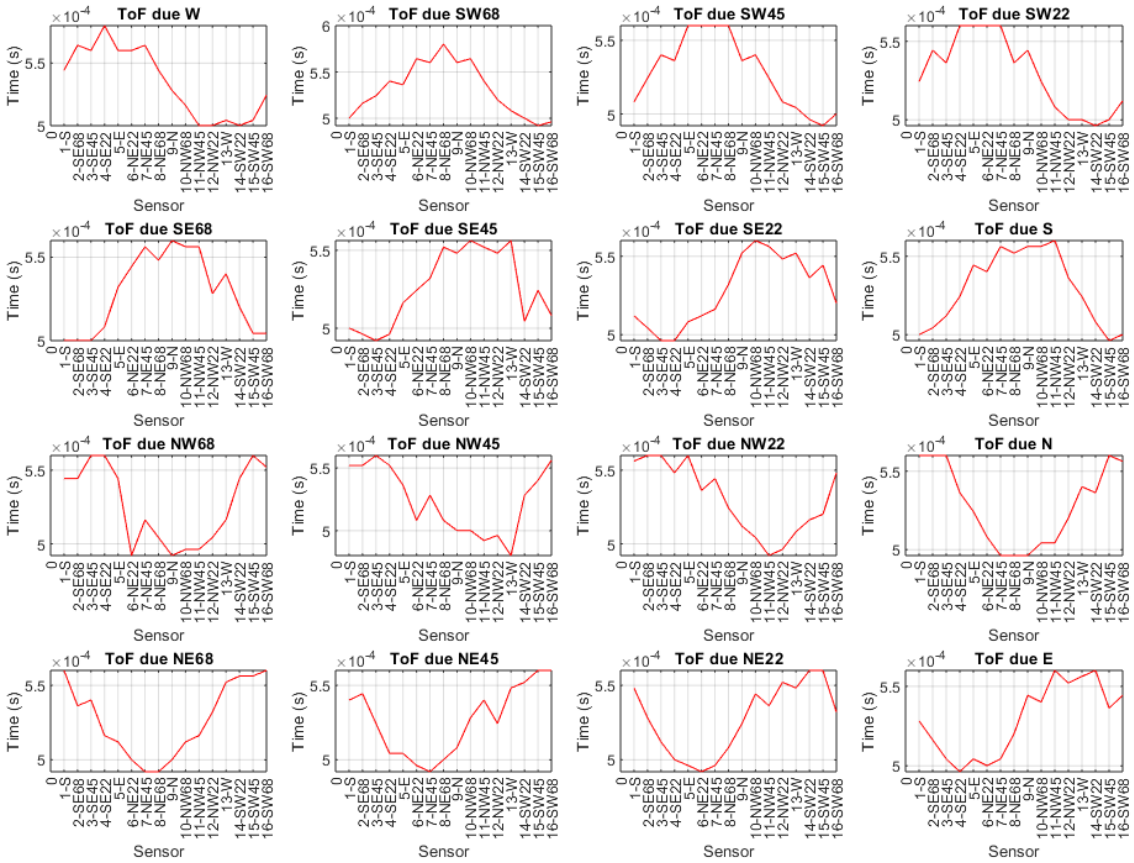

Figure 4.22: TOF of every T-R pair for 16 sensor ring simulation setup with defect added.

In Fig. 4.23 the TOF of the 8 sensor ring simulation setup defect free are shown. The TOF results maintain the theory explained above. The curves of these images are less smooth compared with the 16-sensor ring simulation setup due to only half of the sensors being used in this case. The high jumps in time between sensors can be seen due to the missing sensors used in the other simulation setup. In comparison, TOF obtained from data of the simulated model defect free range from 38 - 42ms and, with defect added, 34 - 40ms.

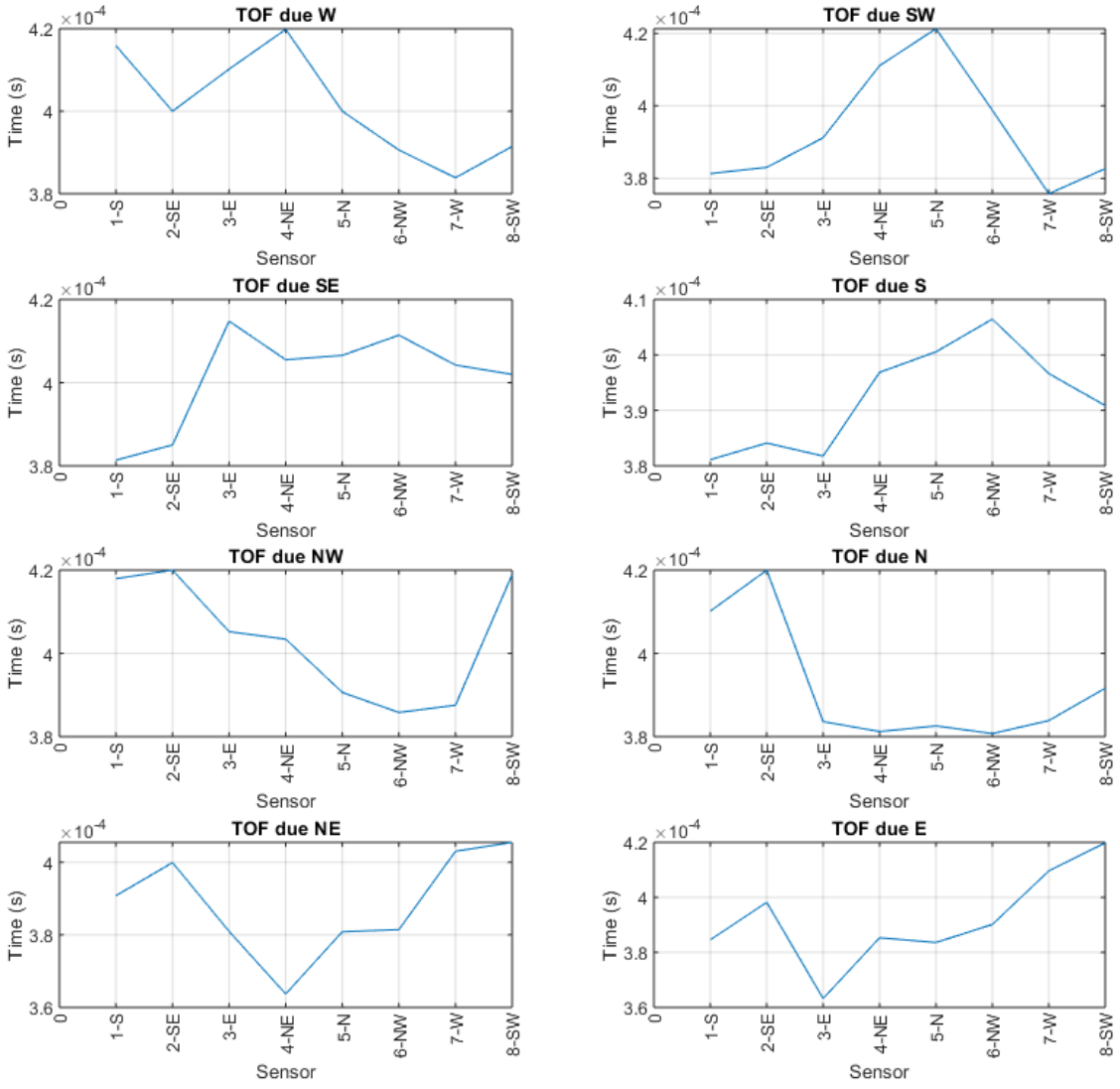

Figure 4.23: TOF of every T-R pair for 8 sensor ring simulation setup defect free.

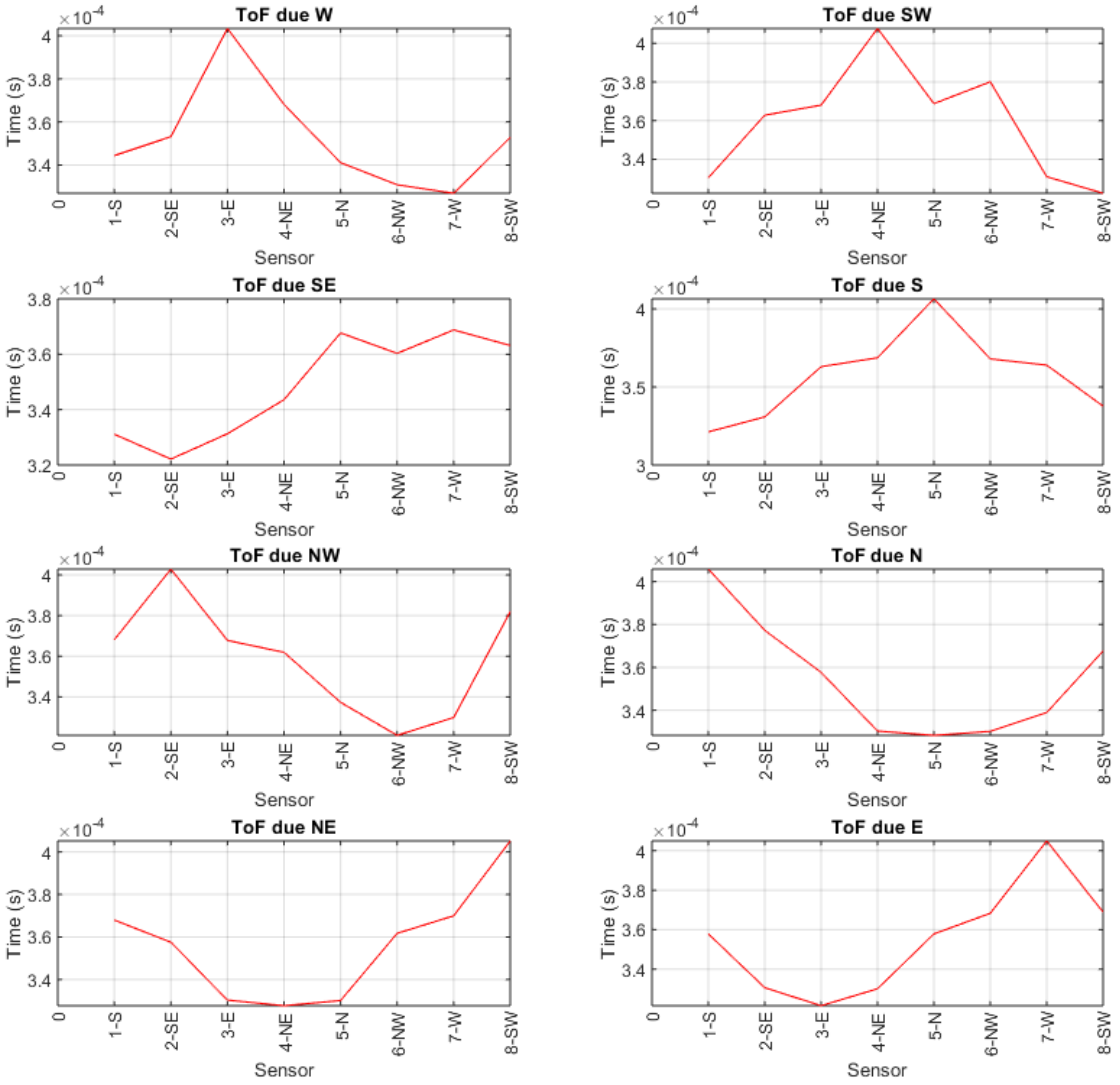

Figure 4.24: TOF of every T-R pair 8 sensor ring simulation setup with defect added

4.3.2 Fast Marching Method Expanding Wavefront

The TOF obtained from the defect free model is then compared with the TOF from the FMM. In Fig. 4.25 and Fig. 4.27 the TOF comparison of the 8 and 16 sensor ring of every transmitter-receiver pair is shown. The blue curve represents the TOF from the FMM, the red curve is the defect free simulation, and the yellow curve is the TOF simulation with defect added. Defect free FMM TOFs are similar, and the valley and crest are very similar in magnitude. They are both attached to the logic of the nearest sensor, having less time in the nearest sensor to the transmitter.

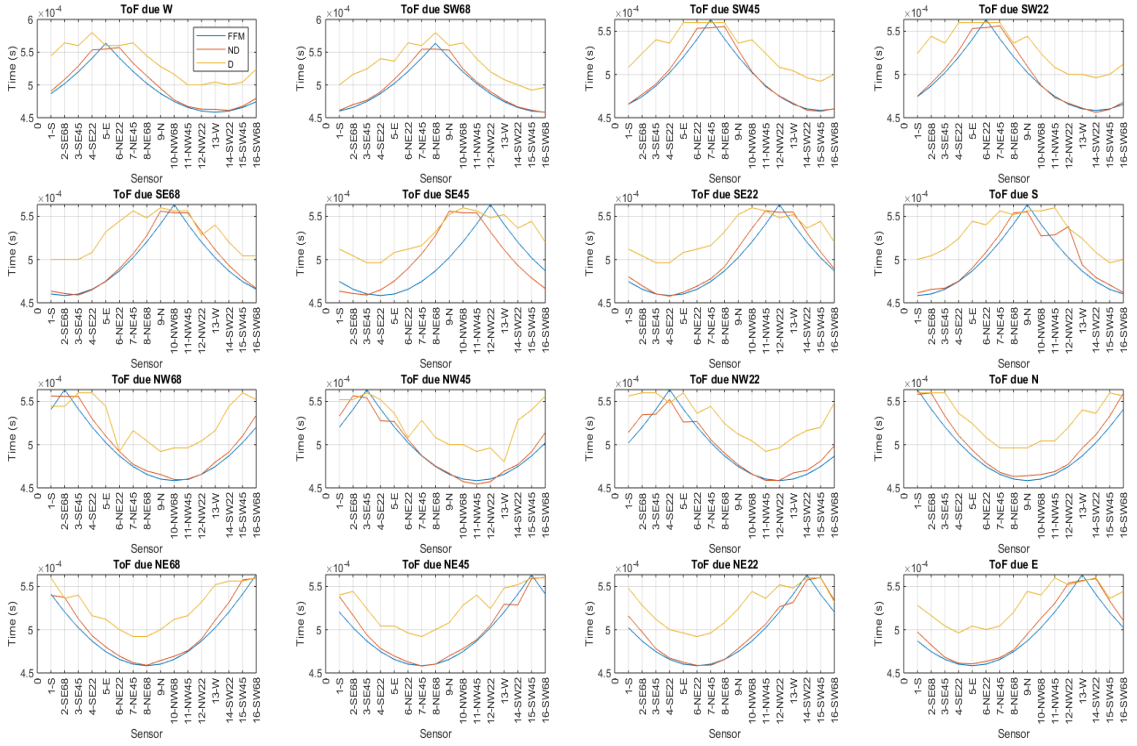

Figure 4.25: TOF comparison. Blue curve is the TOF from FMM. Red curve is the TOF from the defect free model. Yellow is the TOF from the model with defect added.

The difference in % between the defect free and FMM readings are shown in Fig. 4.26 and Fig. 4.28, where the y axis represents the error for % in each T-R pair. An acceptable median error in the TOF obtained from the FMM and defect free simulation is about 7%. The error is obtained from the relation of the T-R pair between the defect free data and the Fast Marching Method expanding wave-front propagation.

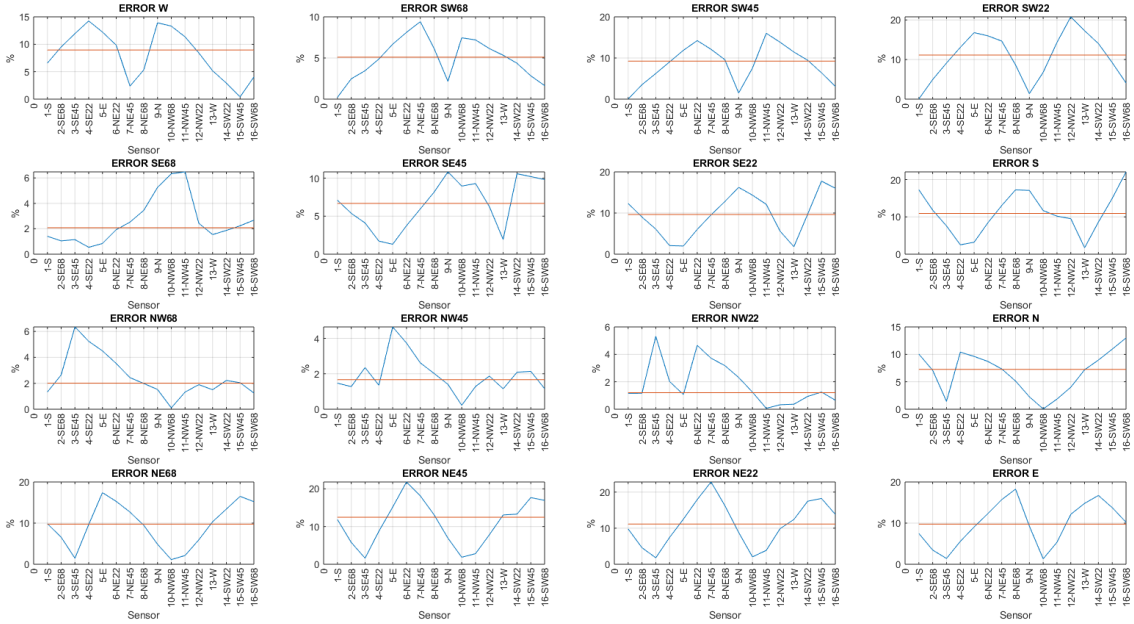

Figure 4.26: Error % of TOF from FMM and defect free data of 16 sensor ring simulation setup

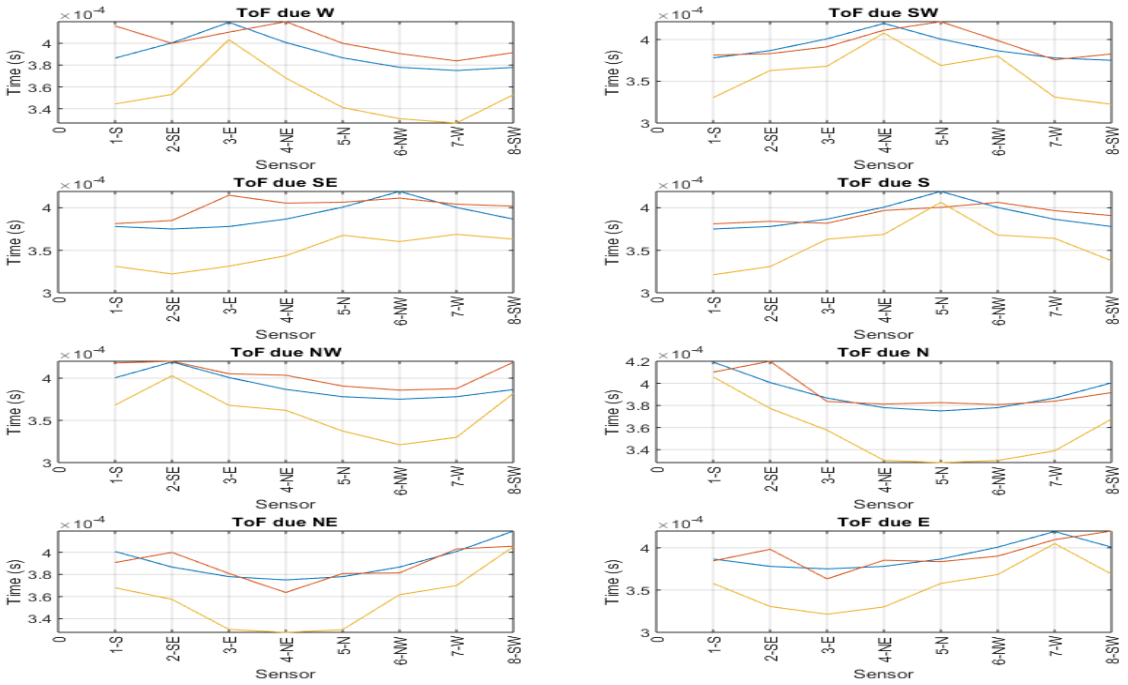

Figure 4.27: TOF comparison. Blue curve is the TOF from FMM. Red curve is the TOF from the defect free model. Yellow is the TOF from the model with defect added.

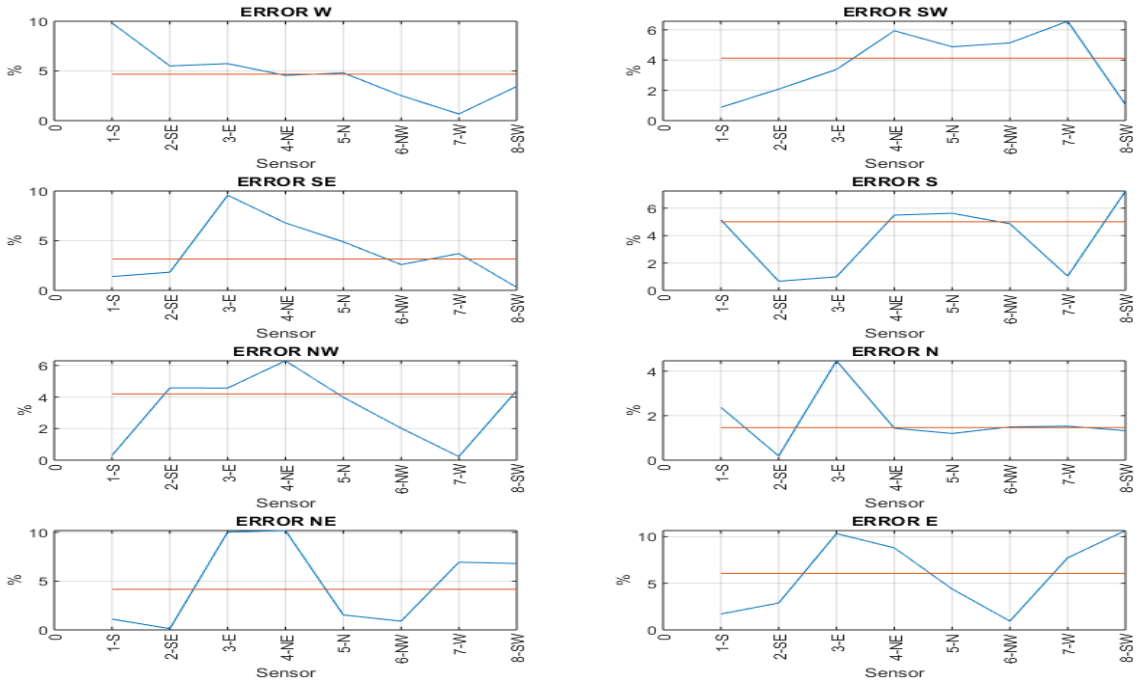

Figure 4.28: Error % of TOF from FMM and defect free data of 8 sensor ring simulation setup

4.3.3 Backprojection

The backprojection is implemented in order to locate the defect backpropagating the difference in TOF. The ray paths shown in section 4.2.3 are used to extract the TOF from the expanding wavefront propagated with the Fast Marching Method in section 4.2.2. The subtracted image is a TOF image, which only includes the TOF that are inside the ray paths (Fig. 4.29 - 4.30). The delay in time of every ray path was back-propagated onto its respective ray path.

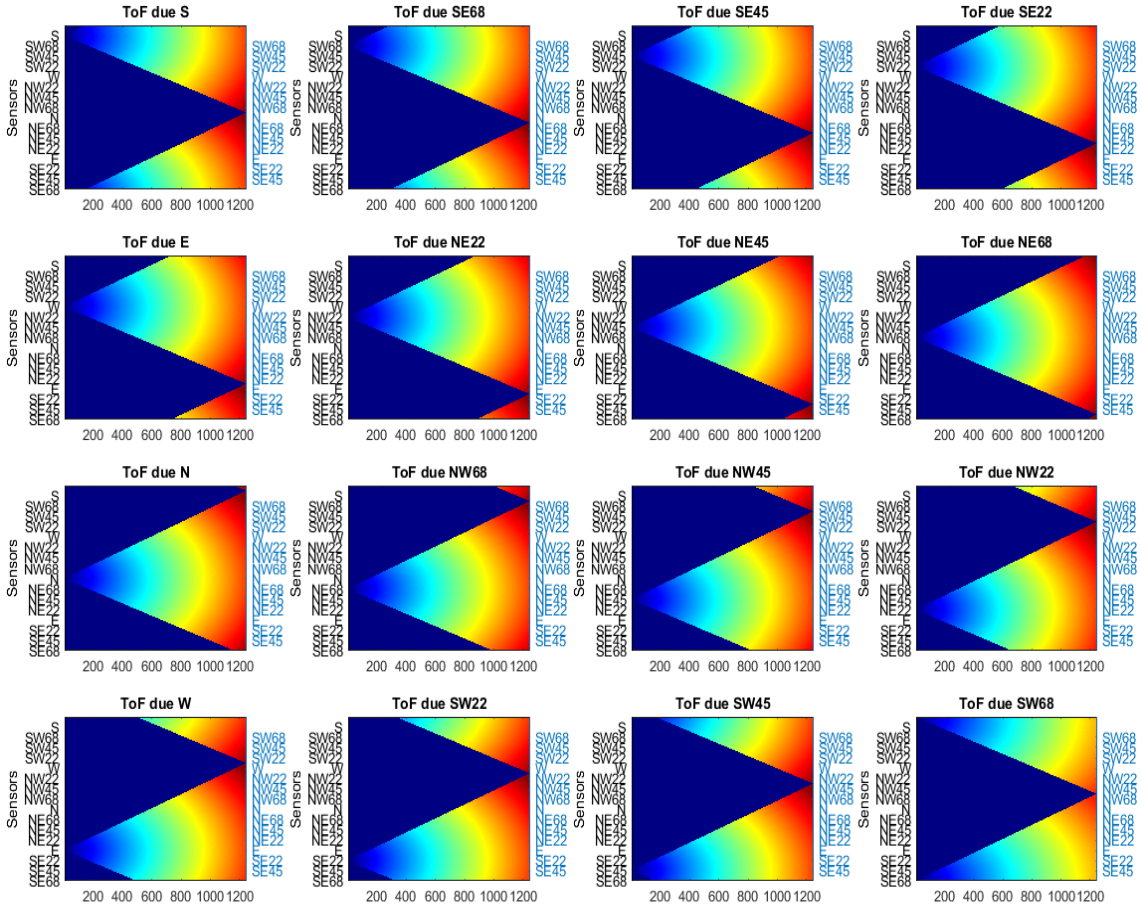

Figure 4.29: Every T-R pair of 16 sensor ring simulation setup

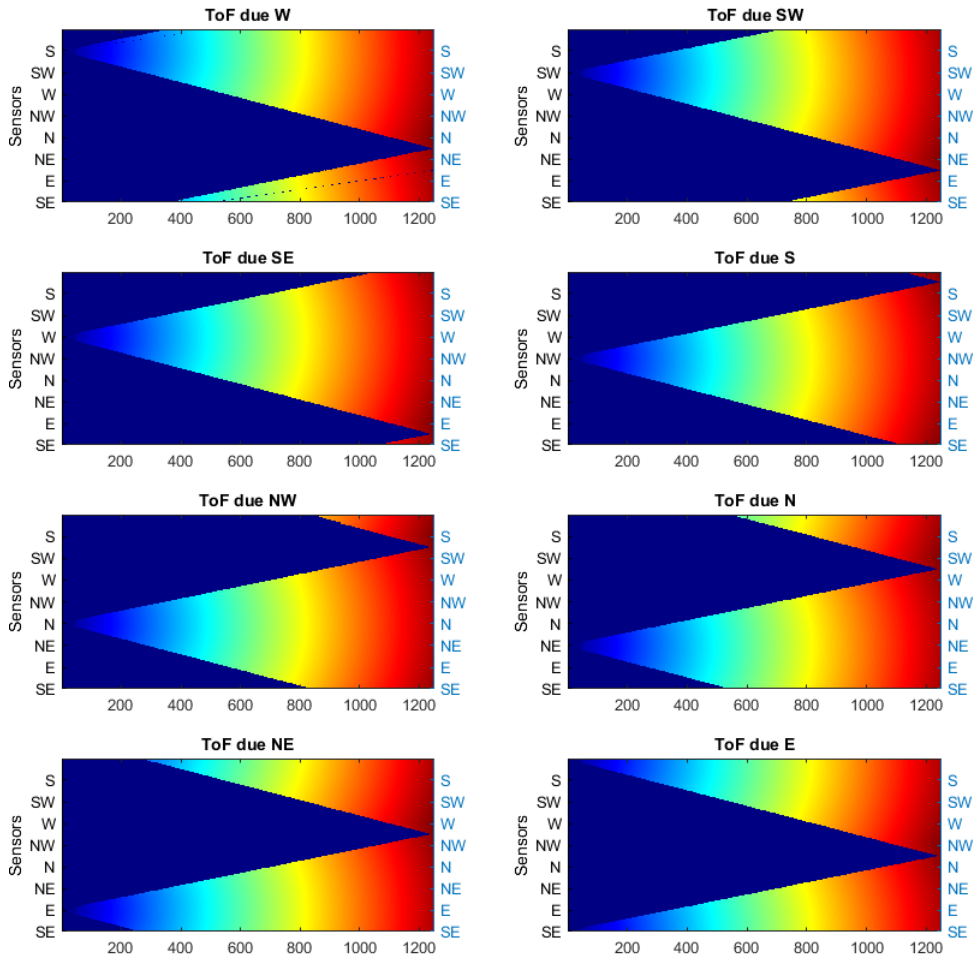

Figure 4.30: Every T-R pair of 8 sensor ring simulation setup.

The ray paths were analyzed one by one. Back-propagating the difference in the arriving time of the readings of the defect-free and with defect added cases. The difference in TOF has been converted into pixels and moved back through the respective ray path. The result is a defined area on the ray path pointing the defect location. In Fig. 4.31 and Fig. 4.32 the detection of the defect is shown. In Fig. 4.31 the defect located in the center of the area of interest is detected using the FMM-SIRT algorithm proposed in this work. In Fig. 4.32 the defect was located using an arrangement of 8 transducers and 8 receivers. In both cases the defect was selected to be in the exact center of the area of interest.

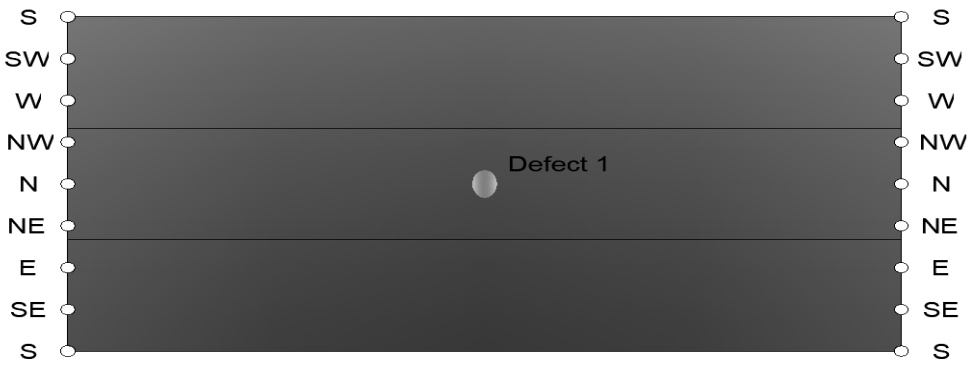

(a) Visual representation of the corrosion defect type position in the pipe

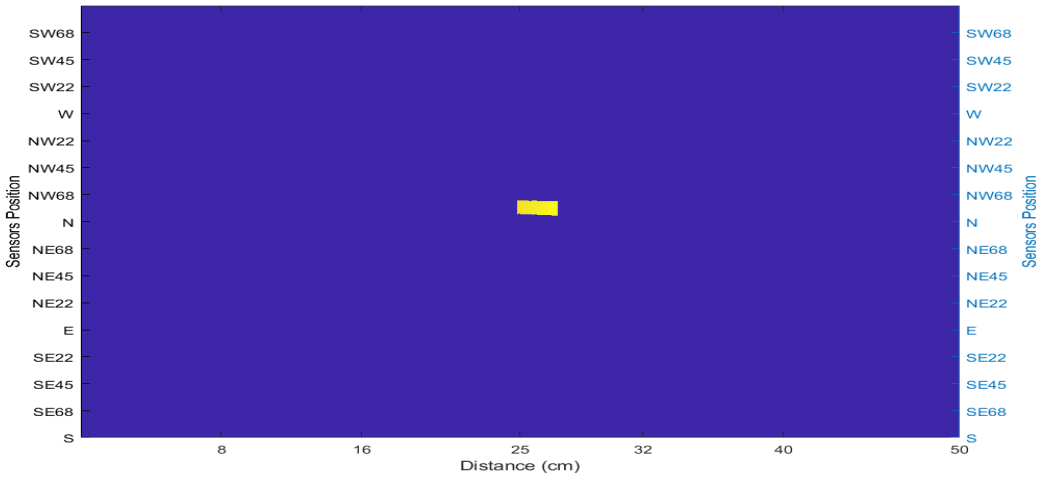

(b) Defect detection through the FMM-SIRT algorithm.

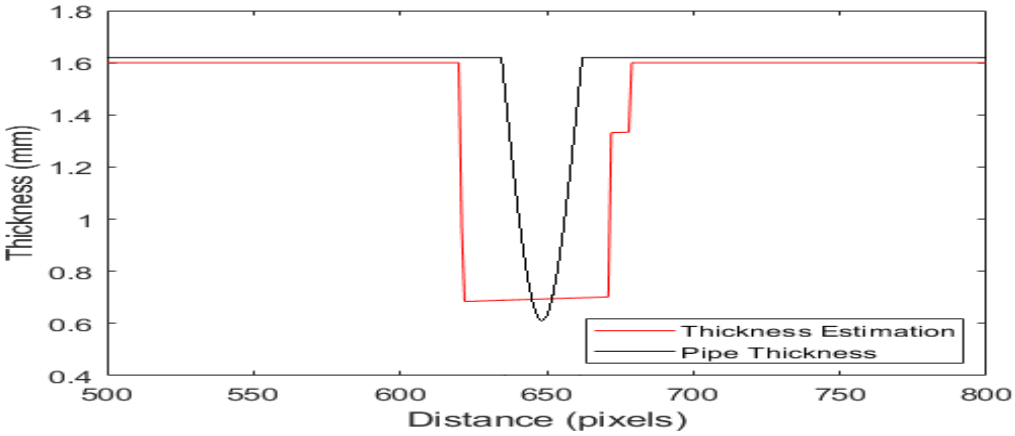

(c) Thickness estimation through the FMM-SIRT algorithm.

Figure 4.31: Defect (a) position, (b) detection and (c) estimation of depth using the 16 transducer arrangement and the implementation of the FMM-SIRT algorithm.

(a) Visual representation of the corrosion defect type position in the pipe

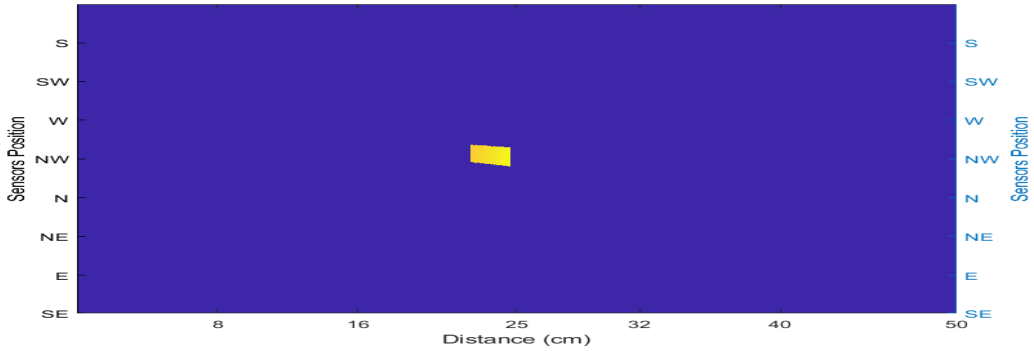

(b) Defect detection through the FMM-SIRT algorithm.

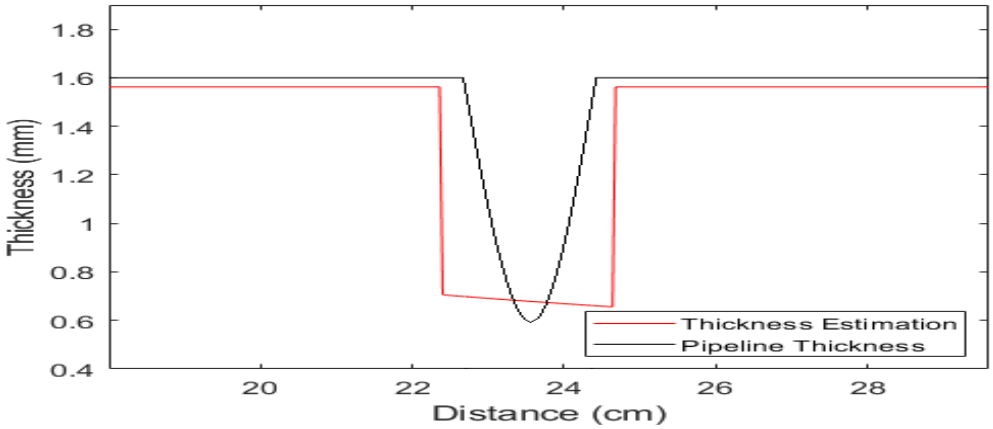

(c) Thickness estimation through the FMM-SIRT algorithm.

Figure 4.32: Defect (a) position, (b) detection and (c) estimation of depth using the 8 transducer arrangement and the implementation of the FMM-SIRT algorithm.

The algorithm was tested for different locations of defects. A second defect was added in a different position in the pipe. The new defect has been placed closer to the receiver ring and between the SW and W lines position. The algorithm was able to successfully detect the defect despite the different position. In Fig. 4.33 is shown the location of the defect added in the model (Fig. 4.33a) and the detection through the FMM-SIRT algorithm (Fig. 4.33b).

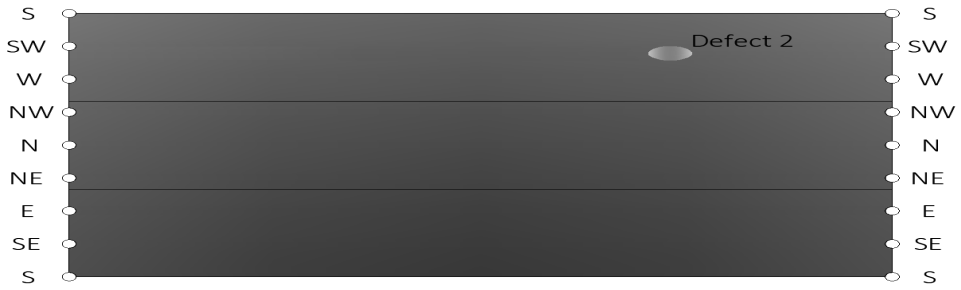

(a) Visual representation of the corrosion defect type position in the pipe

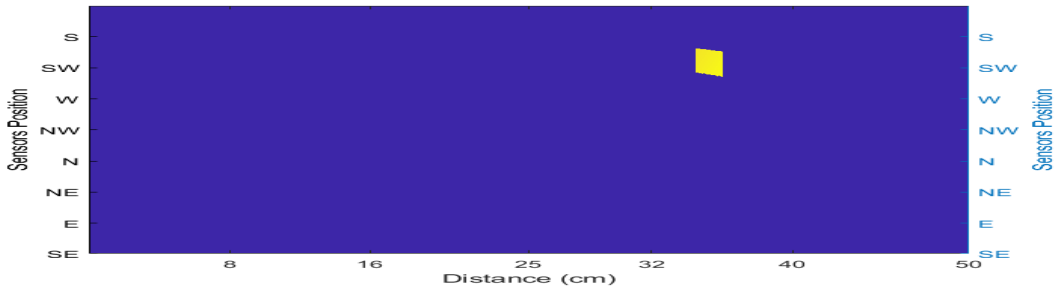

(b) Defect detection through the FMM-SIRT algorithm.

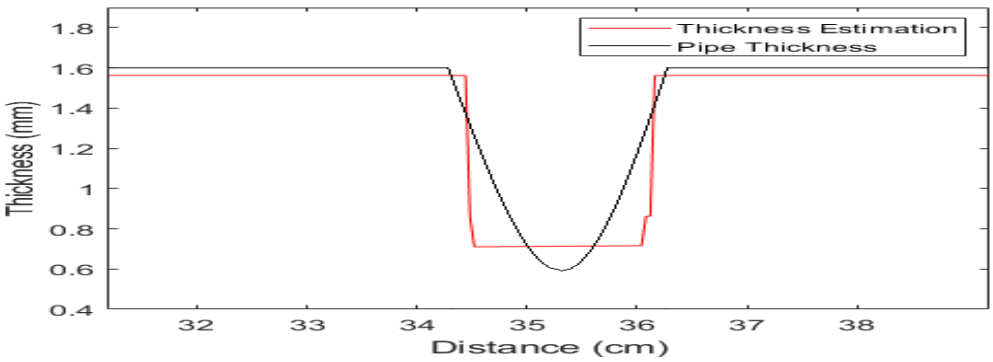

(c) Thickness estimation through the FMM-SIRT algorithm.

Figure 4.33: Defect (a) position, (b) detection and (c) estimation of depth using the 8 transducer arrangement and the implementation of the FMM-SIRT algorithm.

Chapter 5

Experimentation

The experimentation setup is presented in this chapter. Circuit diagrams, devices and test objects specifications are presented. The complete experimentation setup and all specific functions of every circuit, device and objects are explained.

In chapter 2, we discussed the specifications of the EMAT transducer. The coil consists of a copper wire of $0.0148in$ of diameter. The diameter of the magnets is $20mm$ and they are $10mm$ in height, with a strength of $0.51T$. The magnets and the coil are held by a 3D printed case made of Polylactic Acid (PLA). The holder case has a hole in the bottom which allows the current flowing through the coil to induce the eddy currents in the pipe surface. The bottom hole is smaller than the diameter of the coil but enough to allow the induction.

5.1 Experimentation Setup and Transducer Functionality Validation

A first experiment is carried out in order to verify the functionality of the transducer. The waveform of the induced current in the coil is created in the PC and induced into the coil by the National Instruments 6218 (NI-6218). The waveform can be seen in Fig. 5.1. It is a five-cycle tone burst at a center frequency of 10kHz. Before reaching the transducer, the signal passes through a pre-amplifier circuit (Fig. 5.2), which amplifies the signal by 5.6 times. After passing through the pre-amplifier, it reaches another amplifier TPA3116D2, to amplify the signal a further 10 times.

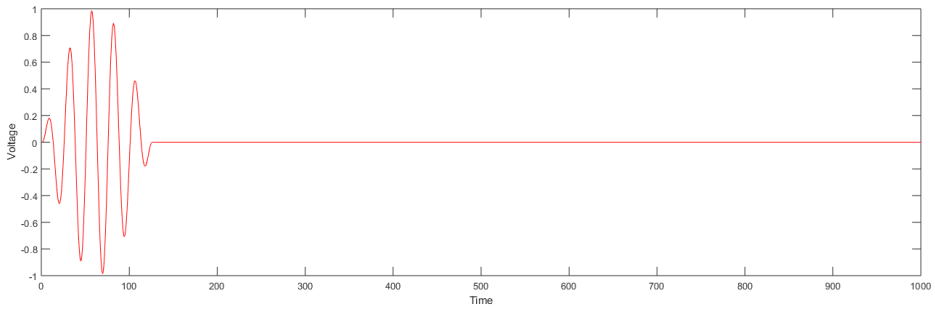

Figure 5.1: Impulse signal at 10kHz.

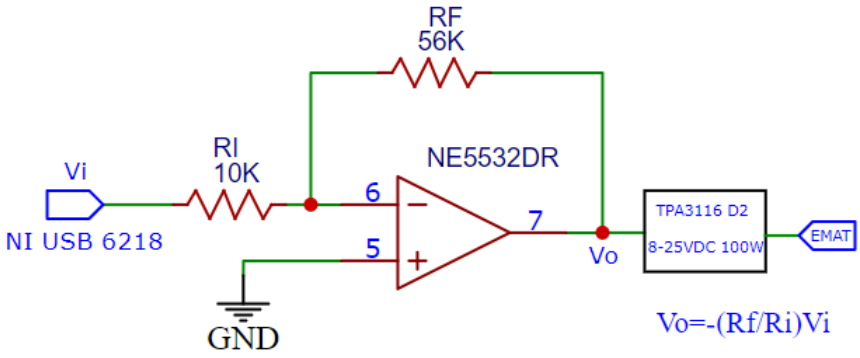

Figure 5.2: Transmitter amplifier circuit.

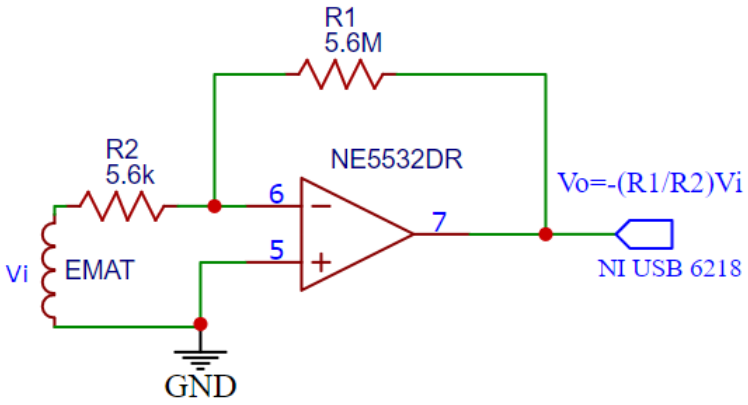

Figure 5.3: Receiver amplifier circuit.

The received signal before reaching the NI USB 618-4 passes through another amplifier (Fig. 5.3). The generated signal in the coil by Faraday's Law is amplified 1000 times and read by the NI USB 6218. The read signal is displayed in Fig. 5.4. The maximum amplitude of the received signal is about 0.4V and has a TOF of 5.96×10^{-4} seconds. The SNR of the signal is 1.5dB, which is considerably lower for being a weak signal. However, the Lamb wave A0 mode is detectable and the Time of Flight is obtainable.

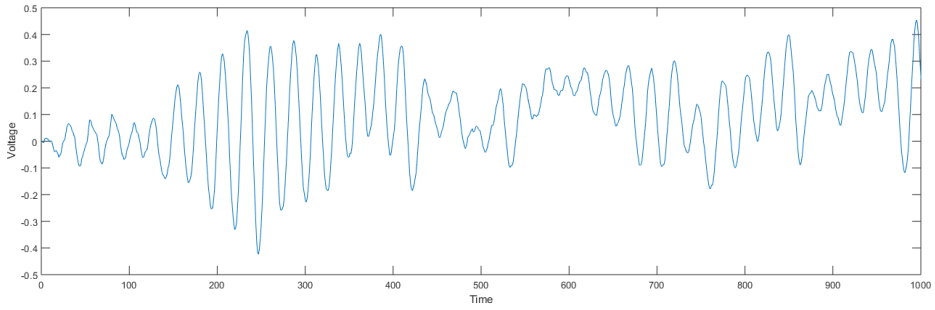

Figure 5.4: Signal transmitted from the transducer.

Despite the signal not being entirely pure, the waveform is preserved and can be visually identified.

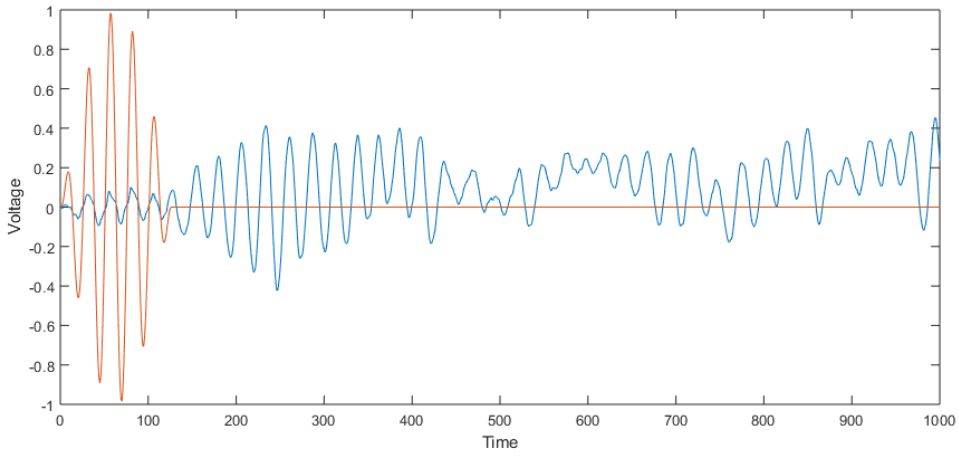

Figure 5.5: Experimentation signals. Red curve impulse signal at 10kHz. Blue curve read signal.

In order to achieve transmission at the frequency of 50kHz, the transmitter amplifier (Fig. 5.2) was modified. Another amplifier TPA3116D2 has been selected with a higher frequency operation range. In Fig. 5.6 the transmitted signal at 30, 40 and 50 kHz can be seen. These signals at the frequencies mentioned were transmitted as a test to check the functionality of the transducer. The transmitted signals preserve the waveform of the induced signal to the coil in the readings. Therefore, the transducer is able to transmit signals successfully at a range of frequencies of 10 to 50 kHz.

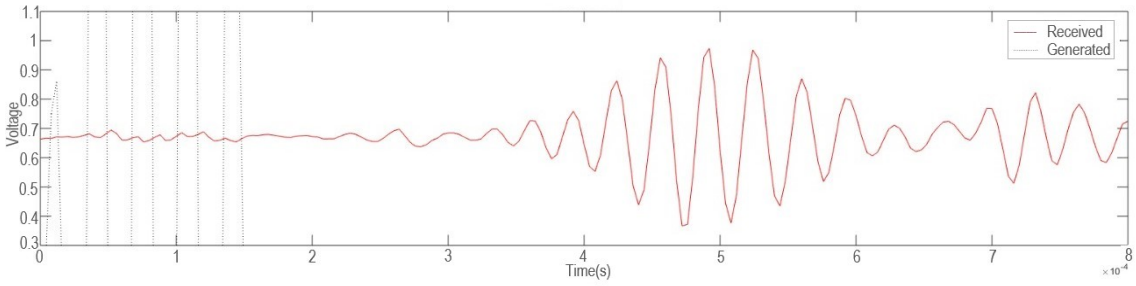

(a) Transmitted signal at 30kHz.

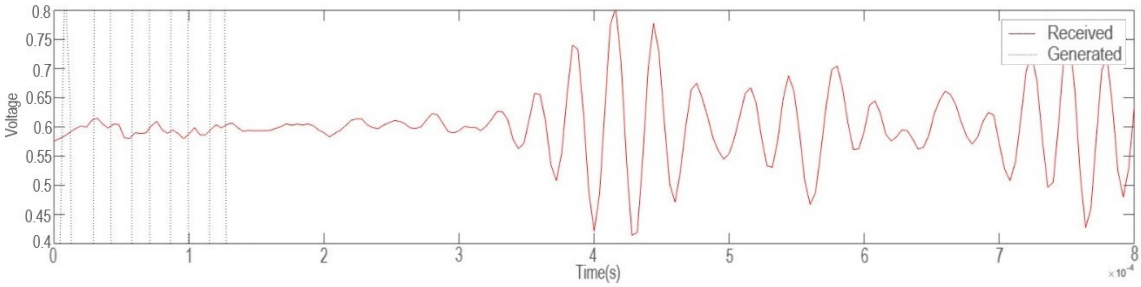

(b) Transmitted signal at 40kHz.

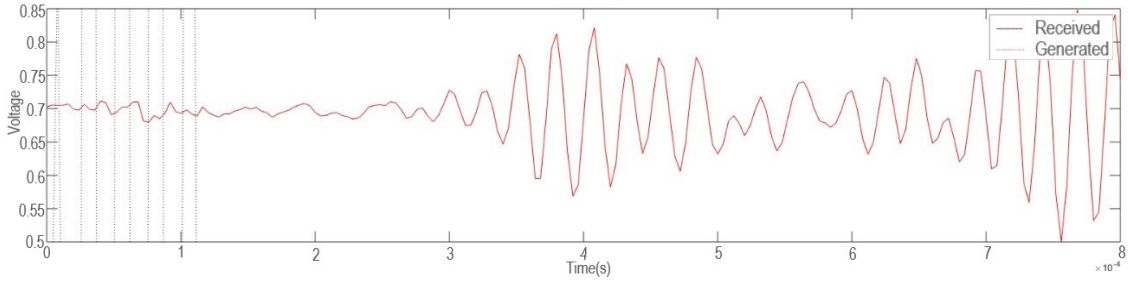

(c) Transmitted signal at 50kHz.

Figure 5.6: Transmitted signals at 30, 40 and 50 kHz

In Fig. 5.7 a flow diagram of the experimentation procedure is shown. As mentioned previously, the five-cycle tone burst signal is created in the PC and transmitted to the transmitter amplifier by the NI USB-6218. The signal, reaches the EMAT to create the waves. The receivers obtain the signal and before reaching the NI USB-6218 are amplified by a receiver amplifier. After, the signals are processed in the PC.

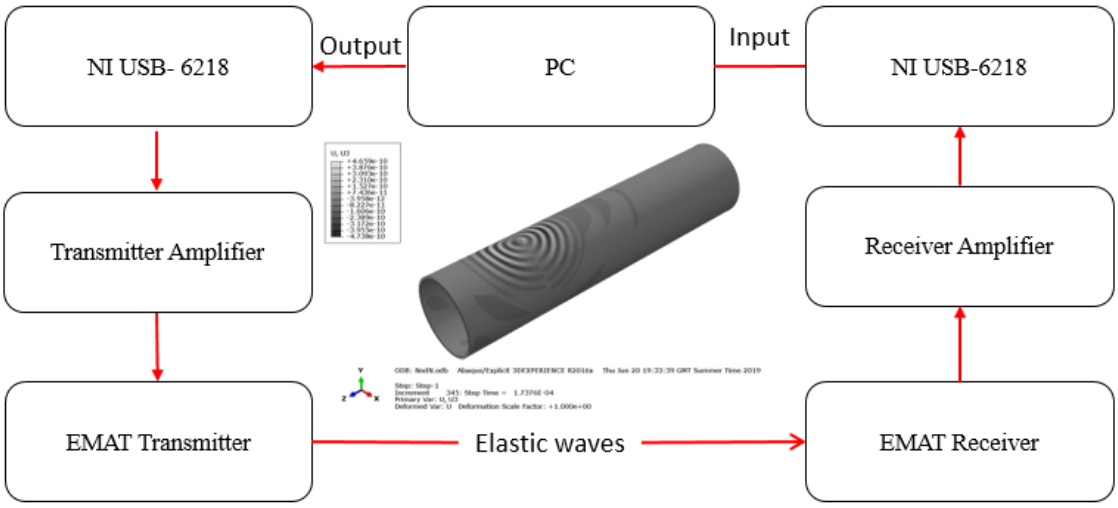

Figure 5.7: Experimentation setup diagram.

The experimental test rig can be seen in Fig. 5.8. The transducers are attached by magnetism to the steel pipe. The induction coil of the EMAT is at a lift-off distance of 1mm. Lamb waves are excited in every transducer one at a time, and all receiver transducers read the signal from the transmitter. A total of 64 signals were obtained for further processing. Moreover, the pipe is a 1m long steel with an outer diameter of 50mm and 1.7mm thickness. The transmitter ring is located 25cm from the left end and the receiver ring is located 25 cm from the right end, as in the simulations. Key names are given to the sensors location as in Fig. 4.11.

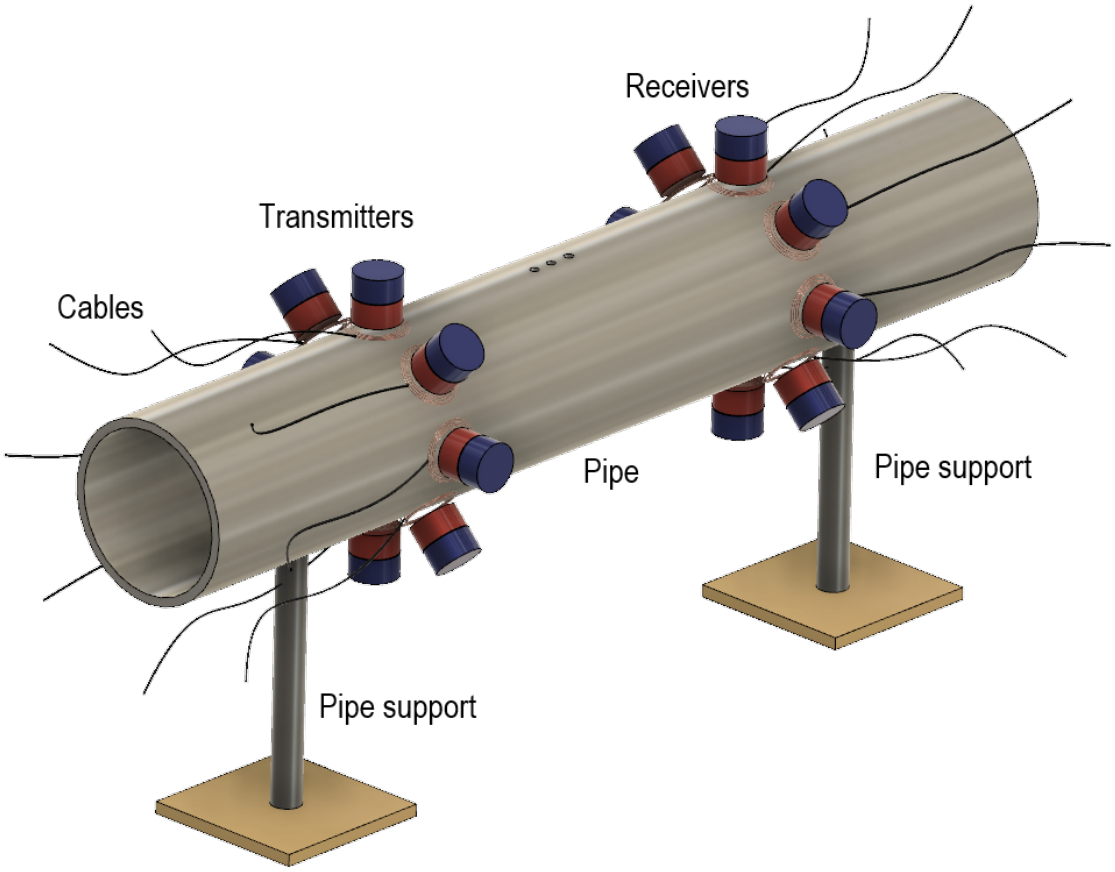

Figure 5.8: Experimentation rig. EMAT transmitter and receiver rings are shown in each side of the defect. Two supports to give stabilization to the pipe were used.

5.2 Experimentation Results

Data was stored using the same system as in the simulations. In this experimentation the readings were voltage instead of displacement. This voltage is generated from the EMAT receiver, the displacement of the particles disturbs the magnetic field and by Faraday's law generates a voltage in the coil. The readings were amplified by the receiver amplifier (Fig. 5.3) and read into the PC by the NI-USB 6218 interface. The data obtained was further processed for the algorithm previously presented.

5.2.1 Time Of Flight

In Fig. 5.9, 5.11 and 5.12 the Times Of Flight of the wave are presented. In Fig. 5.9 the Time Of Flight of the undamaged pipeline is shown. The curves have the same tendency, reaching the closest receiver first depending on the transducer transmitting in each case. This trend is to have the lowest TOF in the nearest receiver sensor. The TOF ranges from $54ms$ to $58ms$ for the undamaged pipe.

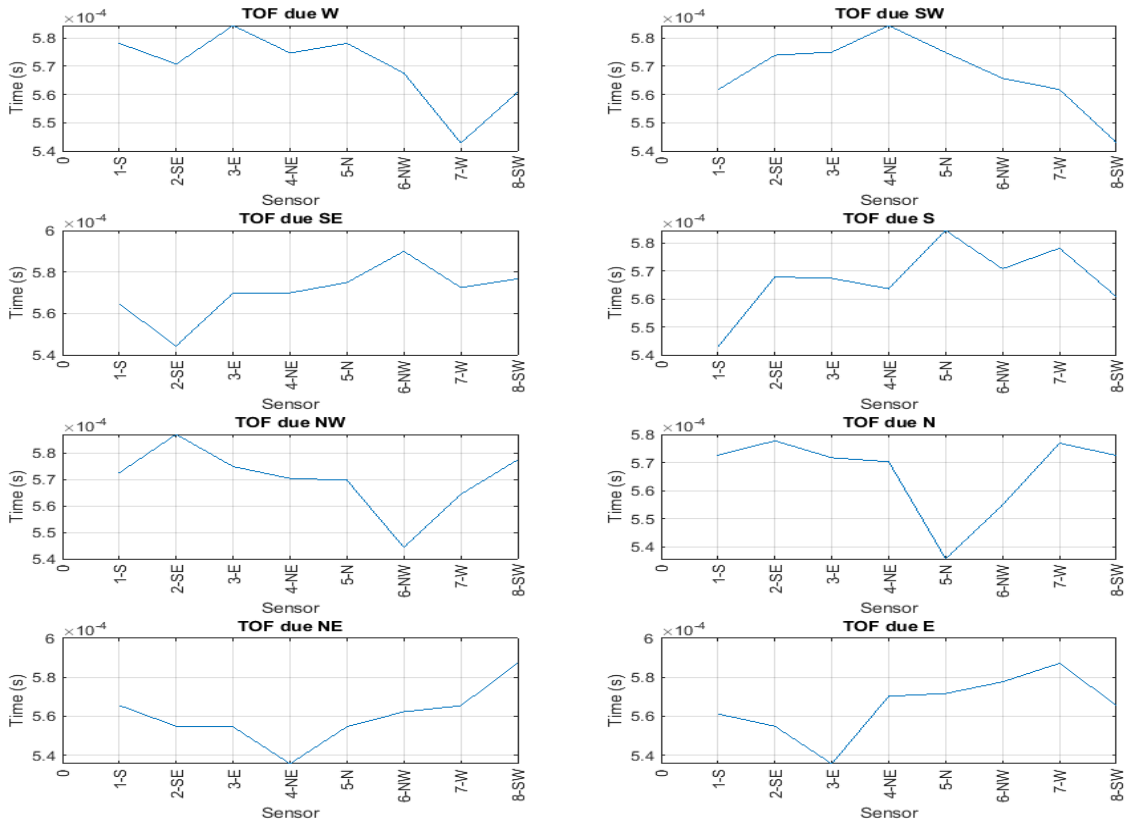

Figure 5.9: Experimentation TOF for the undamaged pipe.

The pipe used for the experimentation has been used in previous work. The 1m pipe has a defect with which we will work for our experimentation. The defect is three small diameter holes located in the middle of the pipeline longitude, at 50cm from each end. The three small holes are 1cm separated from each other. In Fig. 5.10 the defects can be seen. The diameter of the holes is 2mm.

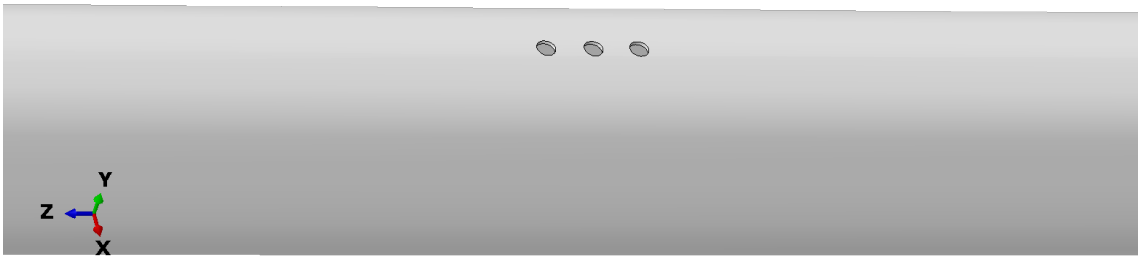

Figure 5.10: Defect added to experimentation pipe.

In Fig. 5.11 the Time Of Flight for the damaged pipe can be seen. The TOF range from $54ms$ to 60-$65ms$ for the damaged pipe. The ray paths that are most affected are the ones that pass where the defect is located.

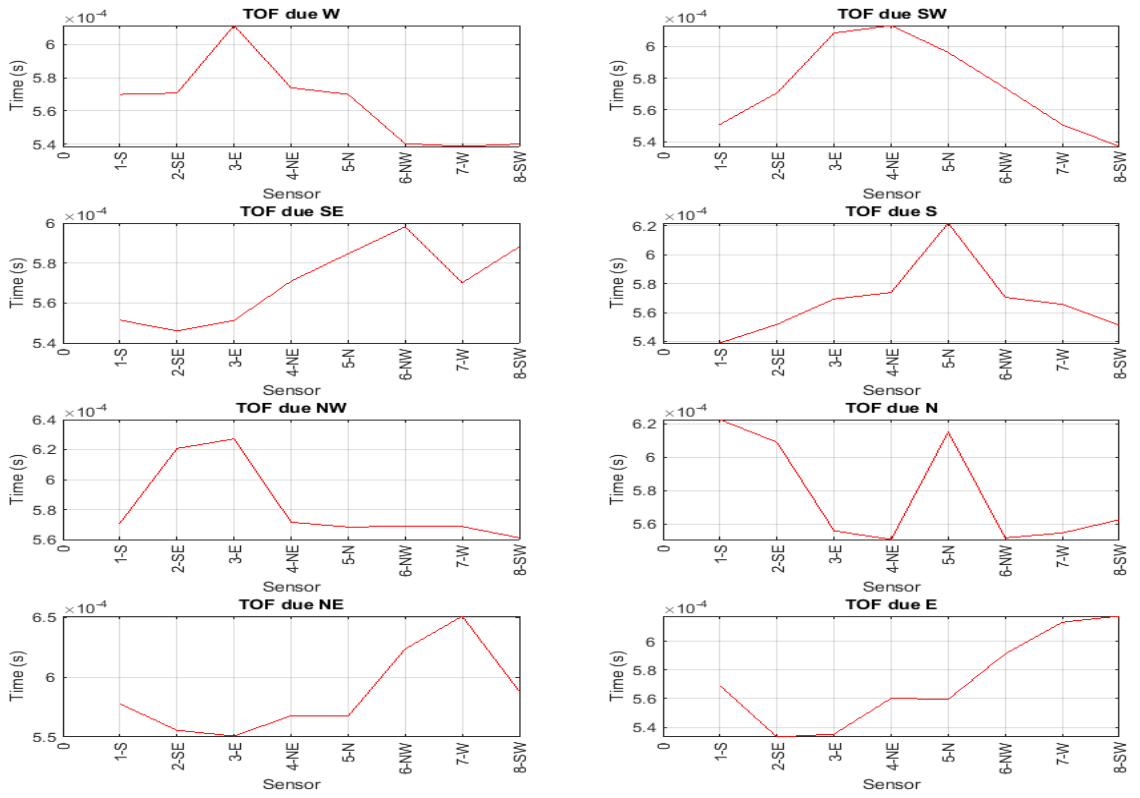

Figure 5.11: Experimentation TOF for the damaged pipe.

In Fig. 5.12 the comparison between the Time Of Flight obtained from the undamaged pipe, damaged pipe and the FMM can be seen. The blue curve represents the TOF obtained from the FMM, the red curve represents the undamaged case and the yellow curve is the damaged pipe. In this comparison we can see the ray paths that are the most affected due to the addition of a defect in the pipe. In the TOF due to the "N" transmitter, the receiver "N" has a big difference in the arrival time compared with the undamaged case and the FMM. This discrepancy is caused by the damage, which produces a reflection in the waves traveling through the pipeline and prevents the wave from travelling as in the undamaged case. This prevention is reflected in a delay of the wave reaching the transducer. Therefore, the wave reaches the sensor later and obtains a higher TOF.

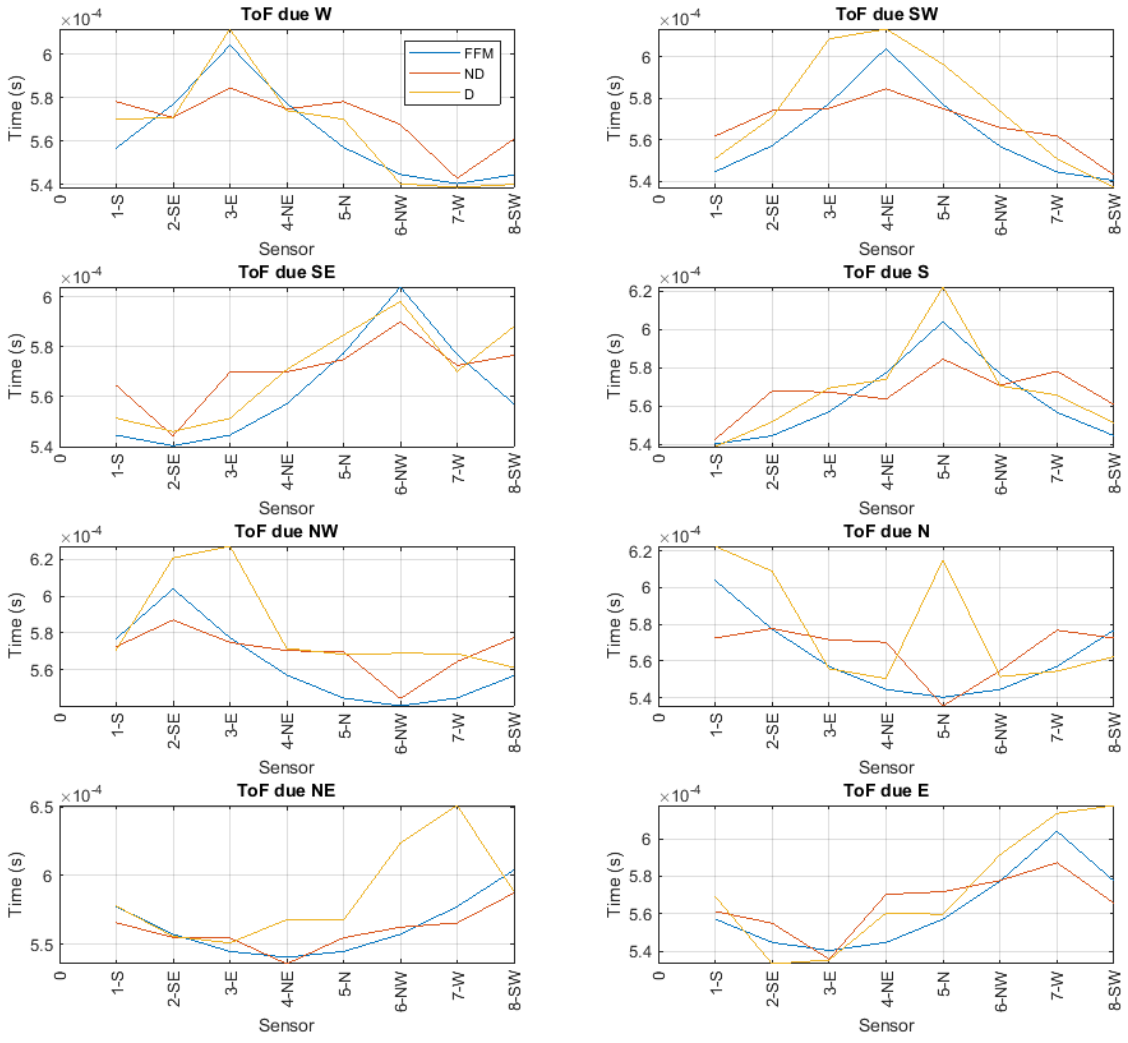

Figure 5.12: TOF comparison.

The image obtained from the algorithm is shown in Fig. 5.13. The image generated with the algorithm highlights the area of the pipeline where the defect is found (Fig. 5.13a). In both sides of the image the position of the sensors are shown. In the horizontal axis the distance in cm is shown. In Fig. 5.13b the thickness estimation across the line in Fig. 5.13a is shown. The thickness data is extracted and represented as a blue curve and the original thickness of the pipeline is represented as a black dashed line. The y axis represents the thickness in mm and the x axis is the horizontal distance in cm.

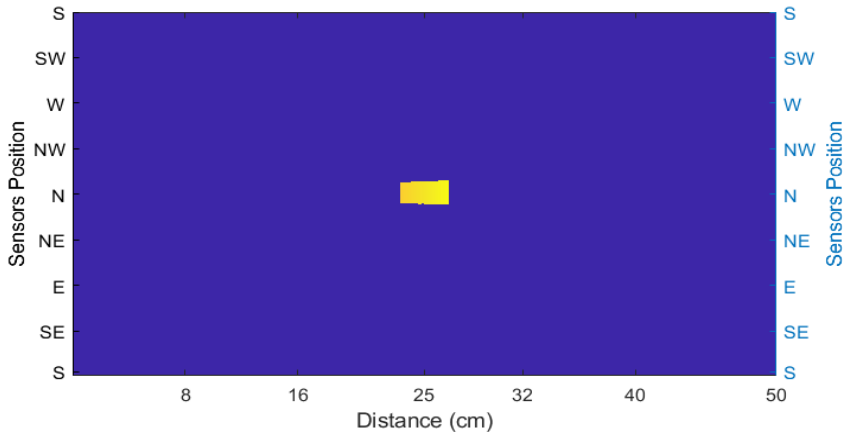

(a) Defect location with FMM-SIRT

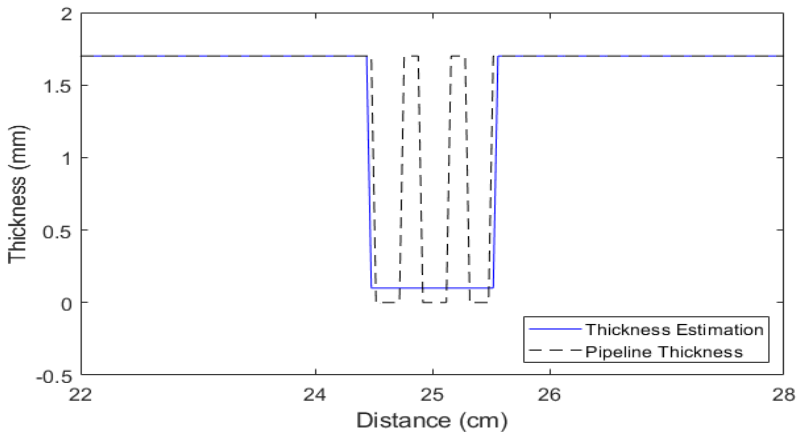

(b) Thickness of pipeline

Figure 5.13: Defect quantification. (a) defect location using the FMM-SIRT algorithm. (b) Thickness of pipe in the section of interest.

5.3 Concluding remarks

In this chapter, experimentation has been carried out. The functionality of the transducer has been tested at frequencies of 30, 40 and 50 kHz. The experimentation process is explained and illustrated. Additionally, the experimentation rig is shown in Fig. 5.8. Moreover, results from experiments, TOF in the defect free section and in the presence of a defect as well as data processed with the proposed algorithm and the achieved image are shown in section 5.2.

Chapter 6

Conclusions

In this thesis, the main objective was to quantify a defect in the wall of the pipe using ultrasonic guided waves using A0 Lamb wave mode at a frequency of 50kHz. This frequency was selected due to the steep change in the dispersion curve of the wave at this frequency range. Being highly variant the wave has more sensitivity to variations in the medium in which it is traveling through. A change in the medium can be identified through a change in the velocity of the wave.

The total number of simulations ran in this work reached to 56. From the total simulations ran, 16 correspond to the 16 transducer arrangement in the defect free situation. Another 16, correspond to the 16 transducer arrangement, however these simulations correspond in the presence of a defect. Additionally, there are 8 simulations from the 8 transducer arrangement in a defect free case, and 8 in the presence of a defect. The remaining 8 simulations from the defect in a different position other than in the center of the area of interest. The wave was produced by an impulse force with the frequency of 50kHz in the area of the transducer position. A sequence of simulations was carried out in order to extract all the data from every transducer position depending on the arrangement used. For the 16 arrangement, 256 pairs of T-R were analyzed and data were collected. Additionally, for the arrangement of 8 transducers ring and the 64 pairs of T-R were analyzed and data was extracted. This procedure was carried out for both scenarios (defect free and in a presence of a defect). An algorithm was built to process data. The TOF

was extracted from the data obtained in the simulations. The TOF was considered to be at the moment when the 20% of the maximum energy recorded in the data crossed the Hilbert transform of the signal. This procedure was carried out for the 704 signals obtained. Additionally, the TOF are compared for the defect free and in a presence of a defect cases. The maximum difference in every transmitter-receiver pair were backpropagated until an image with the location of the defect was achieved. Using the dispersion curve of the Lamb waves, the previous image is converted into a thickness map.

The excitation device has been built based on previous work carried out in the research area. The EMAT transducer uses a sufficiently strong magnet, capable of delivering the necessary strength to produce the A0 wave mode in accordance with a circular coil in a "donut" shape, with a 10 mm inner diameter, 28 mm outer diameter and 42 turns in a double layer configuration. A holder case was built in order to maintain this component in its right position. The blueprints are presented in Fig. 2.4. The specification of components of the device can be seen in Table 2.1. The EMAT built successfully produced A0 Lamb wave (Fig. 5.6). A transmitter amplifier was used to amplify the signal 5.6 times and it was transmitted to the coil by the laboratory equipment available (Fig. 5.2). Additionally, another amplifier was built to amplify by 1000 times the signal read in the receivers (Fig. 5.3). Tests were conducted in order to check the functionality of the device. In Fig. 5.5 and Fig. 5.6 the device and the entire experimentation setup was tested, transmitting signals using the frequency of 10, 30, 40 and 50 kHz.

From the comparison between the TOF obtained in the experimentation and the TOF extracted from the simulation, we can highlight some interesting findings. Although the TOF in the experimentation was higher than in the simulation, the shape of the signal was preserved. This point out that the waves travelled from the same ray path as in the simulation. The experimentation TOF differ around $15 - 20ms$. The main reason of this is the excitation mechanism. In the simulation

case, the wave was produced by an impulse of a concentrated force. Differently, in the experimentation the excitation of the wave was carried out by the conversion of the electromagnetic forces to acoustic forces, which is not very efficient. Nevertheless, the wave produced and the frequency used, were the same. Further work can be made in the difference of producing waves mechanically with an impulse and with the conversion of energy.

Results show the location successfully. However, the shape shown in the image obtained is not precisely the shape of the defect as can be seen in Fig. 4.31, 4.32 and 4.33. The reason for this inaccurate shape is the limited view configuration. As the name states it, is a limited view of the area of interest. The sensors are placed only in two straight lines in both sides of the area. For such configurations the rays only travel from one side to the other, detecting irregularities as presented in this research. Using a full view configuration, the entire area is surrounded by sensors, giving a full view of the area of interest. Extra rays will be traveling through the area from the top to the bottom of the image. The resulting image would be similar to what we obtained except for more accurate shape of the defect detected by the algorithm due to the extra data obtained from different positions.

The quantification of the defect has been achieved to an accuracy of 80% in the experimentation. This accuracy is due the high complexity of the defect for the limited view configuration. On the other hand, quantification of the corrosion defects simulated is higher. For the simulation cases where corrosion defects were used, the quantification starts with an abrupt start instead of a smooth curve as the corrosion defect is presented. Due to this, the algorithm decreased the accuracy of the quantification of the thickness map in the area of interest. Therefore, the algorithm is capable of locating the defect and quantifying the pipe wall successfully.

In Fig. 6.1 a comparison of the results of the three cases are shown. The thickness map on the left side and its respective velocity on the right side are shown. The experimentation case is shown first in Fig. 6.1a and Fig. 6.1b. Corrosion defect 1 is shown in Fig. 6.1c and Fig. 6.1d. Finally, corrosion defect 2 in Fig. 6.1e and Fig. 6.1f.

From the results comparison we can conclude that the resulting quantification of the defect has always the same shape. The shape begins with an abrupt change of thickness instead a smooth decreasing of it in the three graphs. For the experimentation case, the major issue is the alternated three-hole defect in the length direction of the pipe. The areas between holes were not detected due to the limited view configuration. However, it is the case where more accurate results were obtained. The high accuracy is because of the hole defect. The holes represent an abrupt change in thickness as the algorithm presents the results. Moreover, for the corrosion defects the maximum depth of the defect was obtained with an 85% accuracy and an overall accuracy of 80-90%. Moreover, in all cases the location of the defect obtained by the algorithm agrees with the real position of the defect in the simulations and in the experimentation.

The area still has plenty of improvement to make. One of the most difficult areas is the lack of efficiency of the transducer during the conversion from electromagnetic energy into acoustic energy. The device needs a very high supply of electric energy in order to produce a low amount of acoustic energy while transmitting signals. On the other hand, while receiving, the reverse process is still a problem. The conversion from low acoustic energy to electric energy is very deficient. Improvements are needed in the efficiency part of the device. Moreover, the addition of algorithms-based frequency domain analysis could be implemented with the time domain algorithms to get the most of both types and to achieve better results.

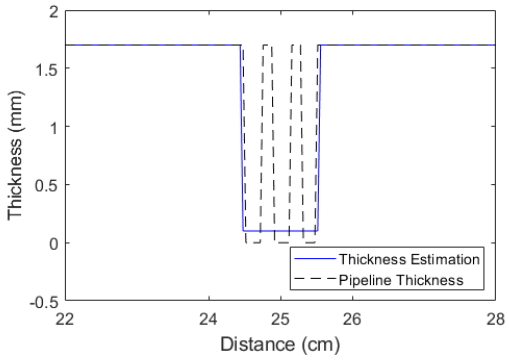

(a) Experimentation thickness estimation

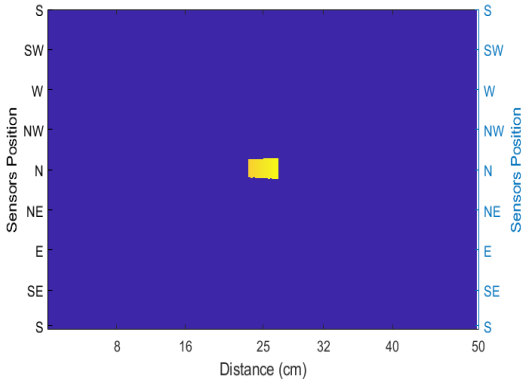

(b) Experimentation velocity map

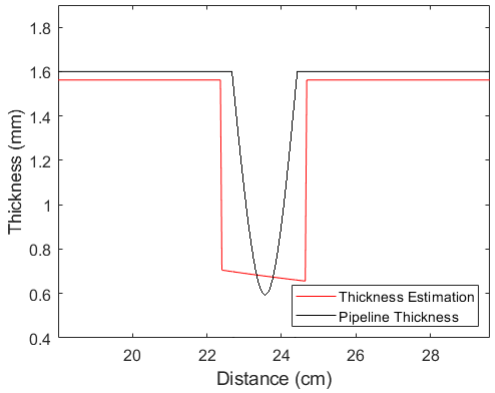

(c) Corrosion defect 1 thickness estimation

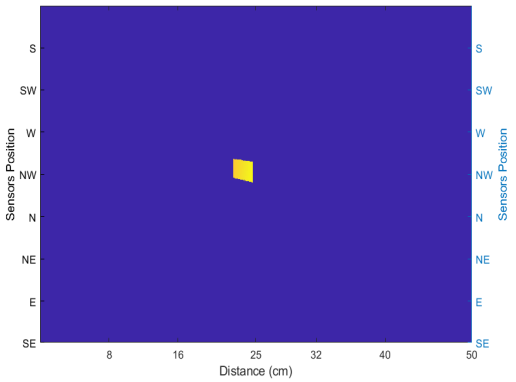

(d) Corrosion 1 velocity map

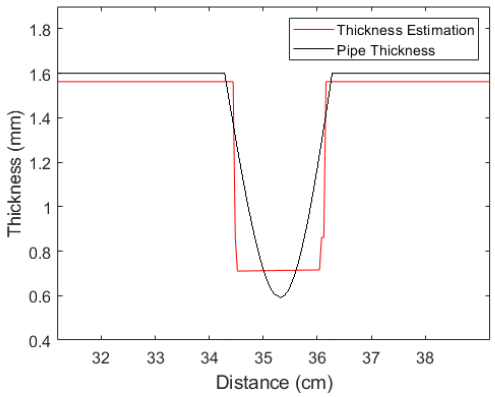

(e) Corrosion 2 thickness estimation

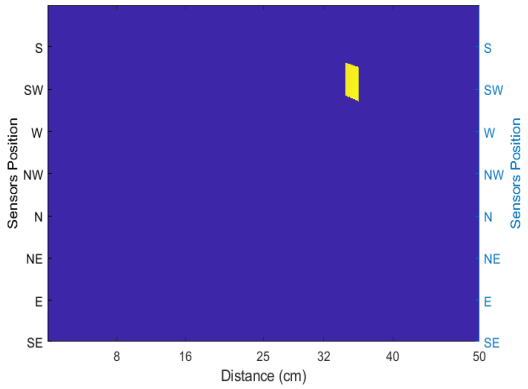

(f) Corrosion defect 2 velocity map

Figure 6.1: Results comparison.

References

[1] Edmonton Journal, "Eight dead, four injured in gas explosion." https://archive.vn/20130215215441/http://www.edmontonjournal.com/1962+Eight+dead+four+injured+explosion/7823967/story.html, note = Accessed, December 10, 2019, 1962.

[2] Government of Canada, "Pipeline investigation report p97h0063." http://www.bst-tsb.gc.ca/eng/rapports-reports/pipeline/1997/p97h0063/p97h0063.html, 1997. Accessed, December 10, 2019.

[3] Electrek Green Energy Brief, "Keystone oil spill in north dakota." https://electrek.co/2019/11/01/egeb-keystone-pipeline-oil-spill-north-dakota-us-green-energy-grows, 2018. Accessed, December 10, 2019.

[4] NDT Resource Center, "About ndt." https://www.nde-ed.org/AboutNDT/aboutndt.htm, 2018. Accessed, December 11, 2019.

[5] R. Dhayalan, K. Balasubramaniam, and C. Krishnamurthy, "Numerical simulation of pulsed meander coil EMAT," in *AIP Conference Proceedings*, vol. 1211, pp. 972–979, AIP, 2010.

[6] H. Boughedda, T. Hacib, M. Chelabi, H. Acikgoz, and Y. Le Bihan, "Electromagnetic acoustic transducer for cracks detection in conductive material," in *2015 4th International Conference on Electrical Engineering (ICEE)*, pp. 1–4, IEEE, 2015.

[7] B. Igarashi, G. Alers, and P. Purtscher, "Magnetostrictive EMAT efficiency as a materials characterization tool," in *Review of Progress in Quantitative Nondestructive Evaluation*, pp. 1485–1492, Springer, 1998.

[8] J. Rose, *Ultrasonic guided waves in solid media*. Cambridge University Press, 2014.

[9] American Society for Testing and Materials, "Standard guide for electromagnetic acoustic transducers (EMATs)," in *Designation: E1774 - 96*, pp. 1–8, ASTM, 1996.

[10] P. Belanger, P. Cawley, and F. Simonetti, "Guided wave diffraction tomography within the born approximation," *IEEE Transactions on Ultrasonics, Ferroelectrics, and Frequency Control*, vol. 57, no. 6, pp. 1405–1418, 2010.

[11] M. Seher, *From EMAT to image: practical guided wave tomography*. PhD thesis, Imperial College London, 2015.

[12] E. Malyarenko and M. Hinders, "Fan beam and double crosshole lamb wave tomography for mapping flaws in aging aircraft structures," *The Journal of the Acoustical Society of America*, vol. 108, no. 4, pp. 1631–1639, 2000.

[13] B. Herdovics and F. Cegla, "Structural health monitoring using torsional guided wave electromagnetic acoustic transducers," *Structural Health Monitoring*, vol. 17, no. 1, pp. 24–38, 2018.

[14] A. Tatarinov, E. N. Barkanov, E. Davydov, and M. Mihovski, "T-and l-types of long-range guided waves for defect detection," in *Non-destructive Testing and Repair of Pipelines*, pp. 15–29, Springer, 2018.

[15] A. Nasedkina, A. Alexiev, and J. Malachowski, "Numerical simulation of ultrasonic torsional guided wave propagation for pipes with defects," in *Advanced Materials*, pp. 475–488, Springer, 2016.

[16] P. Huthwaite, R. Ribichini, P. Cawley, and M. J. Lowe, "Mode selection for corrosion detection in pipes and vessels via guided wave tomography," *IEEE Transactions on Ultrasonics, Ferroelectrics, and Frequency Control*, vol. 60, no. 6, pp. 1165–1177, 2013.

[17] A. Volker and J. Bloom, "Experimental results of guided wave travel time tomography," in *AIP Conference Proceedings*, vol. 1335, pp. 215–222, AIP, 2011.

[18] K. Leonard and M. Hinders, "Guided wave helical ultrasonic tomography of pipes," *The Journal of the Acoustical Society of America*, vol. 114, no. 2, pp. 767–774, 2003.

[19] K. Leonard and M. Hinders, "Lamb wave tomography of pipe-like structures," *Ultrasonics*, vol. 43, no. 7, pp. 574–583, 2005.

[20] S. Huang, S. Wang, W. Li, and Q. Wang, *Electromagnetic Ultrasonic Guided Waves*. Springer Series in Measurement Science and Technology, Springer Singapore, 2016.

[21] Y. Wang, X. Wu, P. Sun, and J. Li, "Enhancement of the excitation efficiency of a torsional wave PPM EMAT array for pipe inspection by optimizing the element number of the array based on 3-d fem," *Sensors*, vol. 15, no. 2, pp. 3471–3490, 2015.

[22] B. Igarashi, G. Alers, and P. Purtscher, "Magnetostrictive EMAT efficiency as a materials characterization tool," in *Review of Progress in Quantitative Nondestructive Evaluation*, pp. 1485–1492, Springer, 1998.

[23] S. Dixon and S. Palmer, "Wideband low frequency generation and detection of lamb and rayleigh waves using electromagnetic acoustic transducers (EMATs)," *Ultrasonics*, vol. 42, no. 10, pp. 1129–1136, 2004.

[24] J. Tkocz, D. Greenshields, and S. Dixon, "High power phased EMAT arrays for nondestructive testing of as-cast steel," *NDT & E International*, vol. 102, pp. 47–55, 2019.

[25] M. Clough, M. Fleming, and S. Dixon, "Circumferential guided wave EMAT system for pipeline screening using shear horizontal ultrasound," *NDT & E International*, vol. 86, pp. 20–27, 2017.

[26] B. Ren and J. Xin, "In-line inspection of unpiggable buried live gas pipes using circumferential EMAT guided waves," in *AIP Conference Proceedings*, vol. 1949, p. 020019, AIP Publishing, 2018.

[27] S. Hill, S. Dixon, P. Rajagopal, and K. Balasubramaniam, "A new electromagnetic acoustic transducer design for generating torsional guided wave modes for pipe inspections," in *AIP Conference Proceedings*, vol. 1806, p. 050003, AIP Publishing LLC, 2017.

[28] M. Seher, P. Huthwaite, M. Lowe, P. Nagy, and P. Cawley, "Numerical design optimization of an EMAT for A0 lamb wave generation in steel plates," in *AIP Conference Proceedings*, vol. 1581, pp. 340–347, AIP, 2014.

[29] P. Wilcox, M. Lowe and P. Cawley, "The excitation and detection of lamb waves with planar coil electromagnetic acoustic transducers," *IEEE Transactions on Ultrasonics, Ferroelectrics, and Frequency Control*, vol. 52, no. 12, pp. 2370–2383, 2005.

[30] S. Wang, S. Huang, A. Velichko, P. Wilcox, and W. Zhao, "A multi-objective structural optimization of an omnidirectional electromagnetic acoustic transducer," *Ultrasonics*, vol. 81, pp. 23–31, 2017.

[31] W. Sun, G. Liu, H. Xia, and Z. Xia, "A modified design of the omnidirectional EMAT for antisymmetric lamb wave generation," *Sensors and Actuators A: Physical*, vol. 282, pp. 251–258, 2018.

[32] K. Ladas and A. Devaney, "Generalized ART algorithm for diffraction tomography," *Inverse Problems*, vol. 7, no. 1, p. 109, 1991.

[33] R. Gordon, R. Bender, and G. Herman, "Algebraic reconstruction techniques (ART) for three-dimensional electron microscopy and x-ray photography," *Journal of theoretical Biology*, vol. 29, no. 3, pp. 471–481, 1970.

[34] S. Ren, J. Zhao, and F. Dong, "Dimensionality reduced simultaneous iterative reconstruction technique for electrical resistance tomography," *Flow Measurement and Instrumentation*, vol. 46, pp. 284–291, 2015.

[35] A. Zürner, M. Döblinger, V. Cauda, R. Wei, and T. Bein, "Discrete tomography of demanding samples based on a modified SIRT algorithm," *Ultramicroscopy*, vol. 115, pp. 41–49, 2012.

[36] H. Banjak, T. Grenier, T. Epicier, S. Koneti, L. Roiban, A.-S. Gay, I. Magnin, F. Peyrin, and V. Maxim, "Evaluation of noise and blur effects with SIRT-FISTA-TV reconstruction algorithm: Application to fast environmental transmission electron tomography," *Ultramicroscopy*, vol. 189, pp. 109–123, 2018.

[37] J. Sethian, "A fast marching level set method for monotonically advancing fronts," *Proceedings of the National Academy of Sciences*, vol. 93, no. 4, pp. 1591–1595, 1996.

[38] J. Sethian, "Fast marching methods," *SIAM review*, vol. 41, no. 2, pp. 199–235, 1999.

[39] J. Bærentzen, "On the implementation of fast marching methods for 3D lattices," tech. rep., Informatics and Mathematical Modelling, Technical University of Denmark, DTU, 2001.

[40] S. Li, K. Mueller, M. Jackowski, D. P. Dione, and L. H. Staib, "Fast marching method to correct for refraction in ultrasound computed tomography," in *3rd IEEE International Symposium on Biomedical Imaging: Nano to Macro, 2006.*, pp. 896–899, IEEE, 2006.

[41] S. Li, K. Mueller, M. Jackowski, D. P. Dione, and L. H. Staib, "Fast marching method to correct for refraction in ultrasound computed tomography," in *3rd IEEE International Symposium on Biomedical Imaging: Nano to Macro, 2006.*, pp. 896–899, IEEE, 2006.

[42] P. Huthwaite and F. Simonetti, "High-resolution guided wave tomography," *Wave Motion*, vol. 50, no. 5, pp. 979–993, 2013.

Appendix A

Publications

The following is a one-page digest that was submitted and accepted for the Conference on Electromagnetic Field Computation (CEFC 2020), which includes the simulation part of this thesis.

Quantitate Evaluation of a Oil Pipeline Crack Using Electromagnetic Acoustic Transducer (EMAT) and Numerical Simulation

Ivan Lazcano[1] and Dr. Qing Wang[1]

[1]Durham University, Department of Engineering, Durham, United Kingdom
ivan.f.lazcano-guzman@durham.ac.uk qing.wang@durham.ac.uk

***Abstract*—Defect detection is of great importance in the oil and gas industry. Quantifying the depth of a defect is achievable with ultrasonic guided waves and Electromagnetic Acoustic Transducer (EMAT). Producing Lamb waves and using their dispersive properties, the velocity variations of these waves travelling within the pipe boundaries can be converted into thickness using a fixed frequency. The Hybrid Algorithm for Robust Breast Ultrasound Tomography (HARBUT) algorithm is employed to achieve this quantification and obtain a thickness map of the pipeline. This project aims to successfully detect a hole defect with a radius of 2.5mm using numerical simulation and experimentation using the HARBUT algorithm in both cases. Using an algorithm based on the Fast Marching Method (FMM), we have obtain the arrival times of the wave in every point of the area of interest for further processing to a thickness image using the dispersion curves.**

***Index Terms*—EMAT, HARBUT Algorithm, Non-destructive testing, Lamb Waves, Ultrasonic Guided Waves**

I. Methodology

The EMAT is a non-destructive testing (NDT) technology principally composed of a coil and a magnet or electromagnet above the coil. The transducer generates acoustic waves electromagnetically using the principle of Lorentz Force. The Lorentz Force is a force that makes the particles of the material vibrate generating elastic waves. The Lorentz force is generated due to the magnet or electromagnet generating a static magnetic that field interacts with the Eddy Currents produced by the AC current induced in the coil. Lamb waves are known for being velocity dependent on the frequency of excitation and the thickness of the medium, also known as, the dispersion relationship. Making use of this relationship we can estimate the thickness of the pipe wall[1].

II. Simulations and Algorithm

A model has been built in order to simulate the wave propagation. A pipeline with a thickness of 6 mm and outer diameter of 114 mm has been selected for the simulations. A line of 16 transmitters was placed 250 mm from the left end of the pipe and a line of receivers at 500 mm from the transmitters. Thirty-two simulations were run to extract data of the wave propagation for the 256 pairs of transmitter-receiver in defect-free and with defect added cases.

The HARBUT algorithm was first developed for the reconstruction of velocity maps of the human breast to detect breast cancer [2], then used for thickness mapping in plates with corrosion [3], and later extended to measure corrosion in pipelines [1]. The algorithm compares Time of Flight (ToF) of the waves in both cases, defect free and with defect added. It compares the Times of Flight of a baseline mode with new data, in this case, the model with defect to detect anomalies in the information. The arrival time was considered to be when the signal exceeds 20 percent of the maximum value of the absolute values of the Hilbert transform [2]. An algorithm based on the FMM was developed to obtain the ToF on every point of the area of interest for further conversion to velocity. The velocity is then transformed into thickness using the dispersion curves of the A0 Lamb wave mode.

III. Results

The algorithm based on the FMM gives a ToF map of the area of interest with an average error of 7 percent regarding the signal from the defect free model obtained in the simulation. The error has been taken as acceptable in order to continue until it is fully developed and obtain the thickness estimation. The ToF signals of 16 pairs of T-R from the defect free model (red) model with defect added (yellow) and algorithm (blue) can be seen in Fig. 1. The signals from defect free and defect model are further compared to obtain the thickness map and identify the defect.

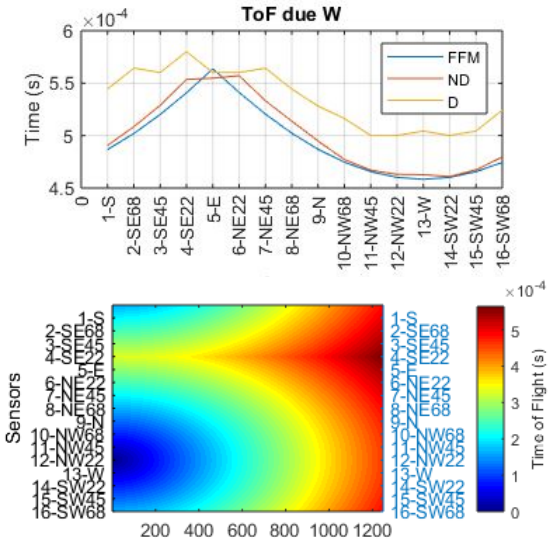

Fig. 1. Top: Time of Flight in every receiver when the transmitter "W" produce the signal. FFM ToF (blue), pipeline with defect (yellow) and pipeline defect free (red). Bottom: area of interest ToF map.

References

[1] Seher, Mathias "From EMAT to image: a practical guided wave tomography" *Imperial College London* 2015
[2] Huthwaite, P and Simonetti, F "High-resolution guided wave tomography" *Wave Motion* vol. 50 no. 5 pp. 979-993 2013
[3] Huthwaite, P and Simonetti, F "High-resolution imaging without iteration: A fast and robust method for breast ultrasound tomography" *The Journal of the Acoustical Society of America* vol. 3 no. 3 pp. 1721-1734 2011